

# Quarks and Antiquarks in Nuclei

Jason Smith

A dissertation submitted in partial fulfillment  
of the requirements for the degree of

Doctor of Philosophy

University of Washington

2005

Program Authorized to Offer Degree: Physics



University of Washington  
Graduate School

This is to certify that I have examined this copy of a doctoral dissertation by

Jason Smith

and have found that it is complete and satisfactory in all respects,  
and that any and all revisions required by the final  
examining committee have been made.

Chair of Supervisory Committee:

---

Gerald Miller

Reading Committee:

---

Gerald Miller

---

Aurel Bulgac

---

Stephen Ellis

Date: \_\_\_\_\_



In presenting this dissertation in partial fulfillment of the requirements for the doctoral degree at the University of Washington, I agree that the Library shall make its copies freely available for inspection. I further agree that extensive copying of this dissertation is allowable only for scholarly purposes, consistent with "fair use" as prescribed in the U.S. Copyright Law. Requests for copying or reproduction of this dissertation may be referred to Proquest Information and Learning, 300 North Zeeb Road, Ann Arbor, MI 48106-1346, to whom the author has granted "the right to reproduce and sell (a) copies of the manuscript in microform and/or (b) printed copies of the manuscript made from microform."

Signature\_\_\_\_\_

Date\_\_\_\_\_



University of Washington

Abstract

Quarks and Antiquarks in Nuclei

Jason Smith

Chair of Supervisory Committee:

Professor Gerald Miller  
Department of Physics

The Chiral Quark-Soliton model provides the quark and antiquark substructure of the nucleon, which is embedded in nuclear matter. This provides a new way to asses the effects of the nuclear medium on the nucleon. We calculate nuclear binding and saturation, describe the European Muon Collaboration effect consistently with Drell-Yan experiments, and predict modifications to the polarized parton distributions. We also calculate the electromagnetic form factors of a bound proton, and find significant modifications of the electromagnetic form factors in the nuclear environment. In every case, the properties of the sea of quark-antiquark pairs in the nucleon are very important, and serve to mitigate the valence quark effect. The changes in the sea quarks when the nucleon is immersed in the nuclear medium are the primary mode by which consistency is maintained with experimental constraints (Drell-Yan data, magnetic moment), while still maintaining a significant effect needed to explain the deep inelastic scattering and polarization transfer data.



## TABLE OF CONTENTS

<b>List of Figures</b>	<b>iii</b>
<b>List of Tables</b>	<b>vii</b>
<b>Glossary</b>	<b>viii</b>
<b>Chapter 1: Introduction</b>	<b>1</b>
1.1 Deep Inelastic Scattering and the EMC Effect . . . . .	3
1.2 The Drell-Yan Process and Dimuon Production . . . . .	8
<b>Chapter 2: The Chiral Quark-Soliton Model</b>	<b>10</b>
2.1 Results From The Instanton Vacuum . . . . .	10
2.2 The Model Lagrangian . . . . .	12
2.3 The Nucleon and the Large $N_C$ Limit . . . . .	17
<b>Chapter 3: Quarks and Antiquarks in Nuclei</b>	<b>20</b>
3.1 The Effect of the Medium . . . . .	20
3.2 The Numerical Procedure . . . . .	24
3.3 The Numerical Results . . . . .	25
<b>Chapter 4: Quark Distributions</b>	<b>33</b>
4.1 Light-cone Correlation Function and Sum Rules . . . . .	34
4.2 Unpolarized Distributions . . . . .	35
4.3 Polarized Quark Distribution Function . . . . .	42
<b>Chapter 5: Electromagnetic Form Factors</b>	<b>50</b>

<b>Chapter 6:</b>	<b>Summary</b>	<b>59</b>
<b>Bibliography</b>		<b>61</b>
<b>Appendix A:</b>	<b>The Connection to Chiral Perturbation Theory and Nonperturbative QCD</b>	<b>69</b>
A.1	The Chiral Lagrangian . . . . .	69
A.2	The Quark Propagator . . . . .	71
<b>Appendix B:</b>	<b>The Kahana-Ripka Basis</b>	<b>75</b>
<b>Appendix C:</b>	<b>DGLAP Evolution</b>	<b>78</b>
<b>Appendix D:</b>	<b>The Failure of Relativistic Nuclear Mean Field Theory</b>	<b>80</b>
D.1	Nucleon Green's Function for Finite Nuclei . . . . .	81
D.2	Wave function Subtleties . . . . .	84
D.3	Derivation of the Plus Momentum Distribution . . . . .	85
D.4	Nuclear Structure Functions . . . . .	91
D.5	Scalar Mesons and More General Considerations . . . . .	97

## LIST OF FIGURES

Figure Number	Page
1.1 Basic diagram of the deep inelastic scattering process $\mu^- + N \rightarrow \mu^- + X$ with momentum transfer $q$ .	4
1.2 The handbag diagram in the parton model. The virtual photon $\gamma^*$ transfers momentum $q$ to the nucleon. The nucleon has momentum $k$ , and the struck quark has momentum $p$ .	5
1.3 Drell-Yan process $p + A \rightarrow \mu^+ \mu^- + X$ . A quark $q$ from the proton, and an antiquark $\bar{q}$ from the nucleus annihilate to form a muon pair.	9
2.1 A 't Hooft vertex [104] for $N_f = 2$ . The instanton is labelled by $I$ , and the quark zero mode wave functions are represented by form factors $\sqrt{M}$ . The arrows indicate the helicity of the quarks.	12
2.2 Quark-meson vertex formed from a 't Hooft vertex (Fig. 2.1), where $\Gamma = 1, \gamma_5, \gamma^\mu, \gamma_5 \gamma^\mu, \sigma^{\mu\nu}$ represent the channels onto which the quark zero modes are projected.	13
2.3 The mass function $M(p)$ using one Pauli-Villars regulator fit to the pion decay constant (heavy line), the instanton model (light line) [37] and the extrapolation of fits to quenched lattice data [86] to the chiral limit using three Pauli-Villars propagators (heavy dashed line), see Appendix A.	14

3.1	Cartoon of the scalar and pseudoscalar densities as a function of radius from the center of the nucleon. The inverse constituent quark mass sets the typical size scale. Pictured are (a) the vacuum condensate, (b) the effective condensate Eq. (3.6), (c) the free nucleon scalar density, (d) the bound nucleon scalar density, and (e) the pseudoscalar density. . . . .	23
3.2	Diagram of the two-tier self-consistent loop. One inputs a value for $k_F$ and a guess for the profile function. $\Theta$ represents the field equation for the profile. $\Psi$ represents the Dirac equation solved in the finite basis, which takes the profile function as an input, and outputs a set of energy eigenvalues $E_n$ and wave functions. The $E_n$ are then used to calculate a the nucleon mass $M_N$ which is then used to calculate a new nucleon scalar density. . . . .	26
3.3	Binding energy per nucleon $B = E/A - M_N$ as a function of Fermi momentum fit to $B = -15.75$ MeV at the minimum for $g_s = 0.89$ (long dashed), 1.10 (short dashed) and 1.27 (solid). The box and shaded region are the experimental uncertainty [20] in the binding energy, density and compressibility of nuclear matter. . . . .	28
3.4	Profile functions in nuclear matter. The solid line is the profile function for $1.5\rho_0$ ; the curves with progressively longer dashes correspond to $1.0\rho_0$ , $0.5\rho_0$ and zero density respectively. . . . .	29
3.5	Profile functions for the free nucleon using the valence approximation of Eq. (3.5) (solid) and a fully self-consistent treatment (dashes). . . . .	30
3.6	The nucleon mean square radius as a function of Fermi momentum. The 3.1% increase at $k_F = 1.38 \text{ fm}^{-1}$ is indicated by the horizontal and vertical lines. Experiments [75, 102] limit nucleon root mean square radius swelling to less than 6%, or 1.12 on the vertical axis. . . . .	32
4.1	The smoothing effect of evolution on the quark singlet distribution. The curves are shown at scales $\log M_{PV}^2$ (highest curve at $x = 0.3$ ), and the DIS scale $\log Q^2$ , with $Q^2 = 10 \text{ GeV}^2$ (lowest curve at $x = 0.3$ ). . . . .	37

4.2	The EMC ratio at a scale $Q^2 = 10 \text{ GeV}^2$ for nuclear matter. The data are for Iron (empty boxes) and Gold (filled boxes) from SLAC-E139 [52]. . . . .	39
4.3	The Drell-Yan ratio at a scale $Q^2 = 10 \text{ GeV}^2$ for nuclear matter. The data are for Iron (empty boxes) and Tungsten (filled boxes) from FNAL-E772 [2]. . . . .	40
4.4	The distribution $xq^S(x)$ in a free (dashed) and bound (solid) nucleon at a scale $Q^2 = 10 \text{ GeV}^2$ . . . . .	41
4.5	The ratio Eq. (4.8) at scale $Q^2 = 10 \text{ GeV}^2$ for nuclear matter. The heavy line is the full calculation for nuclear matter. The light line is the effect calculated using only medium modifications to the ‘valence’ energy level as described in the text. . . . .	45
4.6	The distribution $\Delta q^{NS}(x)$ in a free (dashed) and bound (solid) nucleon at a scale $Q = 10 \text{ GeV}^2$ . . . . .	46
4.7	The asymmetry $A_1^{(p)}$ Eq. (4.17) at scale $Q^2 = 10 \text{ GeV}^2$ . The heavy line is for nuclear matter. The dashed line is for the free proton. The data are from SLAC [5] (filled) for $Q^2 \sim 1 - 40 \text{ GeV}^2$ and HERMES [1] (empty) for $Q^2 \sim 1 - 20 \text{ GeV}^2$ . The free curve falls slightly below the data due to the lower value of $g_A$ calculated in the large $N_C$ limit. . . . .	49
5.1	The isoscalar electric form factor at nuclear density (solid) and at zero density (dashes). . . . .	53
5.2	The isovector magnetic form factor at nuclear density (solid) and at zero density (dashes). . . . .	54
5.3	The electric (lower three curves) and magnetic (upper three curves) form factor ratios in Eq. (5.13) for $0.5\rho_0$ (long dashes), $1.0\rho_0$ (solid) and $1.5\rho_0$ (short dashes). . . . .	55
5.4	The double ratio Eq. (5.14) of the electric to magnetic form factors in nuclear matter and in the vacuum from the $\chi$ QS model (heavy) and the QMC model [73] (light). Three densities are shown: $0.5\rho_0$ (long dashes), $1.0\rho_0$ (solid) and $1.5\rho_0$ (short dashes). . . . .	56

A.1	Fits of Eq. (A.12) for $n = 3$ to the quenched lattice data [86] for the dynamical quark mass $M(p)$ at current quark masses $m_q a = 0.012, 0.018, 0.024, 0.036, 0.048, 0.072, 0.108$ , and $0.144$ , where $a$ is the lattice spacing. . . . .	73
A.2	Fits of Eq. (A.12) for $n = 3$ to the quenched lattice data for the wavefunction renormalization function $Z(p)$ at various quark masses. The data falls slightly below the fits. This can be attributed to an effect of the finite volume of the lattice [86]. . . . .	74
D.1	Feynman diagram for deep inelastic lepton-nucleus scattering. A nucleus of momentum $P$ is struck by a virtual photon of momentum $q$ . We label nucleon momentum $k$ , and quark momentum $p$ . . . . .	81
D.2	The function $\chi$ in a mean field theory with scalar ( $\sigma$ ) and vector ( $\omega$ ) mesons. . . . .	82
D.3	Plus momentum distributions, $f(y)$ , for $^{40}\text{Ca}$ (solid), $^{16}\text{O}$ (short dashes), $^{208}\text{Pb}$ (dot-dashes) and nuclear matter (long dashes). . . . .	92
D.4	$f(y)$ distribution for $^{16}\text{O}$ (solid) after application of the Soper-Yan transformation along with the $^{16}\text{O}$ distribution from Ref. [21] (short dashes). Note that the peaks occur at $y < 1$ . . . . .	93
D.5	Ratio functions for $^{16}\text{O}$ , $^{40}\text{Ca}$ and $^{208}\text{Pb}$ showing data for Carbon, Calcium and Gold, respectively, from SLAC-E139 [52]. The nuclear matter calculation shows extrapolated data [97]. . . . .	94
D.6	$R(x = 0.72)$ as a function of $A$ including scalar meson and binding effects (solid line), and leaving binding energy per nucleon constant at $-8.5$ MeV (dashed line). The data are from SLAC-E139 [52]. . . . .	96

## LIST OF TABLES

Table Number	Page
3.1 Model parameters to fit binding energy $B = -15.75$ MeV, the location of the minima, compressibility, and the resulting density of nuclear matter in units of $\rho_0 = 0.178 \text{ fm}^{-3}$ consistent with the experimental value of $0.167 \pm 0.018 \text{ fm}^{-3}$ [20]. . . . .	27
A.1 Constants appearing in the integrals for $L_i$ . . . . .	71
B.1 The momenta for each grand spin $G$ for the 1576 Kahana-Ripka basis functions, with cut-off and box size $\Lambda = 600$ MeV and $L = 5$ fm, respectively. The number of basis functions for each $G$ for $\Lambda = 600$ MeV (I), and $\Lambda = 5000$ MeV (II) are shown in the far right two columns. . . . .	77

## **GLOSSARY**

DGLAP: Dokshitzer-Gribov-Lipatov-Altarelli-Parisi

DIS: Deep Inelastic Scattering

EMC: European Muon Collaboration (effect)

FNAL: Fermi National Accelerator Laboratory

GPD: Generalized Parton Distribution

HERMES: HERA fixed target experiment to explore spin

IA: Impulse Approximation

KR: Kahana-Ripka (basis)

MFT: Mean Field Theory:

MIT: Massachusetts Institute of Technology (bag model)

NJL: Nambu-Jona-Lasinio (model)

NM: (Infinite) Nuclear Matter

OPE: Operator Product Expansion

PV: Pauli-Villars (subtraction)

QCD: Quantum Chromodynamics

QMC: Quark-Meson Coupling (model)

RDWIA: Relativistic Distorted-Wave Impulse Approximation

RMFT: Relativistic Mean Field Theory

RMSGA: Relativistic Multiple-Scattering Glauber Approximation

RPWIA: Relativistic Plane-Wave Impulse Approximation

SLAC: Stanford Linear Accelerator Center

TJNAF: Thomas Jefferson National Accelerator Facility

$\chi$ PT: Chiral Perturbation Theory

$\chi$ QS: Chiral Quark-Soliton (model)



## Chapter 1

### INTRODUCTION

The past century has seen the birth and incredible progress of the physics of hadrons and their strong interactions from the discovery of the nucleus [88] to the recognition of Quantum Chromodynamics (QCD) as the fundamental theory of the strong interactions with the 2004 Nobel prize in physics [54, 84]. Despite being the fundamental theory, describing a proton, much less an entire nucleus, in the context of the quark and gluon degrees of freedom of QCD is still out of reach. The fundamental theory is non-perturbative at the low energy, long wavelength scales of nuclear physics, but it does tell us some very useful information about the physics of hadrons. It gives us a scale  $\Lambda_{QCD}$  that separates perturbative and non-perturbative physics, tells us how to translate our knowledge at one scale to another through the evolution equations, gives us an approximate chiral symmetry implying its spontaneous breaking at low scales, and hints at the non-perturbative degrees of freedom with the instanton solutions to the QCD field equations providing a possible mechanism for that symmetry breaking [104]. The enormous effect of chiral symmetry has been encapsulated in the very successful low energy effective theory, Chiral Perturbation Theory ( $\chi$ PT) [49].

These high and low energy theories have yet to meet, and a frontier of hadronic physics lies in the intermediate range of length scales available to present experiments where neither QCD nor  $\chi$ PT have useful perturbative expansions. Neither fundamental quarks and gluons nor point-like hadrons provide a complete description, so including the non-perturbative information that hadrons are bound states of valence quarks in a polarized vacuum is necessary. One way to probe these intermediate length scales and this non-perturbative physics is to examine the short distance structure of a large object. The prime example is the

European Muon Collaboration (EMC) effect [7] measured in lepton-nucleus Deep Inelastic Scattering (DIS) where the short distance ( $\sim 5$  GeV, or  $\sim 10^{-2}$  fm) structure of nuclei differs from that of a collection of free nucleons. This measurement showed that the quarks and antiquarks in bound nucleons carry less momentum than in free ones, and implied that the medium modification of nucleon structure could be significant for many nuclear observables [50]. Explanations of the EMC effect have remained a diverse and controversial theoretical subject. Until a measurement of dimuon production in proton-nucleus scattering through the Drell-Yan process [2] demonstrated separately that the antiquarks in nucleons are virtually unchanged in a nuclear system, there was virtually no other handle on medium modifications in DIS. Many explanations either fail to describe the Drell-Yan data, fail to address antiquarks at the non-perturbative scale of nuclei, or fail to address antiquarks altogether.

There is a hint to the solution from evolution in QCD; dynamical rescaling [29] suggests that the EMC effect is due to a lowering of the starting scale for the renormalization group equations. While successful at describing the phenomenology of both the EMC effect and Drell-Yan experiments, like the situation for QCD and chiral symmetry breaking, it is silent on the actual mechanism and scale.

The first evidence that the protons and neutrons had structure came from the measurement of their electromagnetic form factors in elastic lepton-nucleon scattering [74]. Recent polarization transfer experiments at TJNAF (Thomas Jefferson National Accelerator Facility, also referred to as JLab) [102] observed a difference in the electromagnetic form factors of a proton bound in a Helium nucleus compared to a free one. This seems to add to the evidence in favor of the modification of hadrons in the nuclear medium.

We would like to address the subject of medium modifications with a theory that is consistent with QCD and  $\chi$ PT. Any description of the EMC effect must be consistent with the constraints set by both DIS and Drell-Yan data. Thus a successful model must include antiquarks as well as quarks, and show how the medium modifies both the valence and sea quark distributions. Our purpose is to provide a mechanism for that modification within the Chiral Quark-Soliton ( $\chi$ QS) model [68, 16, 39, 26]. It is essentially a relativistic mean field approximation approach to baryons motivated by the Instanton Liquid Model (ILM) of the

QCD vacuum and the large  $N_C$  expansion (discussed in Chapter 2). This phenomenological model has many desirable qualities: the ability to describe a wide class of hadron observables with surprising accuracy given its simplicity, the inclusion of antiquarks, the positivity of quark distributions [36], polynomiality of Generalized Parton Distributions (GPD) [94], and a basis in QCD [39]. The model also predicted the mass and narrow width [41] of the  $\theta^+$  pentaquark for which there was encouraging early evidence [8, 81], but remains a controversial subject with many experiments showing null results [43]. One of the drawbacks of the model is that, in the form presented here, it lacks explicit confinement. This is the property of QCD that quarks and gluons are never seen as free particles. The lack of confinement in the  $\chi$ QS model has not prevented it from describing a wide variety of free nucleon observables [26]. Here we show how the model describes nuclear saturation properties, reproduces the EMC effect, satisfies the bounds on nuclear antiquark enhancement provided by Drell-Yan experiments, and predicts large effects in spin polarized structure functions and electromagnetic form factors.

We will continue this introduction to the subject with a more detailed description of deep inelastic scattering and the EMC effect in Section 1.1 and dimuon production in Section 1.2. We will then present the  $\chi$ QS model in Chapter 2, and use it to build a nuclei out of quarks and antiquarks in Chapter 3. The medium modifications of the quark distributions and electromagnetic form factors are calculated in Chapters 4 and 5, respectively. In the Appendices, we elaborate on the connection of the  $\chi$ QS model to  $\chi$ PT and QCD via lattice calculations of the non-perturbative quark propagator, provide background on the small binding effect predicted by relativistic mean field theory for finite nuclei and nuclear matter, and present some details for the numerical work. This work is built on results that have been published previously elsewhere [79, 98, 99, 100].

### **1.1 Deep Inelastic Scattering and the EMC Effect**

Deep inelastic lepton-nucleon scattering occurs when a virtual photon, mediating the interaction, of high energy and momentum  $q$  ( $-q^2 \gg \Lambda_{QCD}^2$ ) fragments the target nucleon  $N$  of mass  $M_N$  into a host of particles labelled  $X$ . The electromagnetic interaction couples

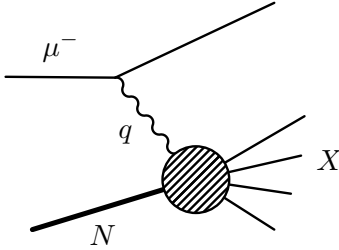


Figure 1.1: Basic diagram of the deep inelastic scattering process  $\mu^- + N \rightarrow \mu^- + X$  with momentum transfer  $q$ .

to all of the electrically charged constituents in the target nucleon. Deep inelastic scattering experiments see the valence quarks as well as the virtual quarks and antiquarks in the polarized QCD vacuum simultaneously.

The case where the lepton is a muon is illustrated in the Feynman diagram in Fig. 1.1. The use of the optical theorem allows us to package our ignorance of the photon-nucleon vertex and fragmentation function in Fig. 1.1. In inclusive inelastic scattering (where one measures the cross section with any final state  $X$ ), we can write the sum on the final states  $X$  of the diagram in Fig. 1.1 as

$$\sum_X \left| \text{Diagram} \right|^2 = 2 \operatorname{Im} \left( \text{Diagram} \right) \equiv 2 \operatorname{Im} W^{\mu\nu}(k, q)$$

We can use Lorentz covariance and current conservation to write down the form of  $W^{\mu\nu}$

$$W^{\mu\nu}(k, q) = \left( g^{\mu\nu} - \frac{q^\mu q^\nu}{q^2} \right) W_1(k, q) + \frac{1}{M_N^2} \left( k^\mu - q^\mu \frac{k \cdot q}{q^2} \right) \left( k^\nu - q^\nu \frac{k \cdot q}{q^2} \right) W_2(k, q), \quad (1.1)$$

but we need a model to calculate  $W^{\mu\nu}$ , specifically the functions  $W_1$  and  $W_2$ , explicitly. For example, we can use the parton model of Bjorken and Feynman as in Fig. 1.2, where the nucleon is composed of massless (or nearly massless) point-like, non-interacting, mostly spin-1/2 constituents. This model is justified by the asymptotic freedom [84, 54] of QCD, where at high energy the strong interaction coupling  $\alpha_s$  between the quarks and gluons goes to zero.

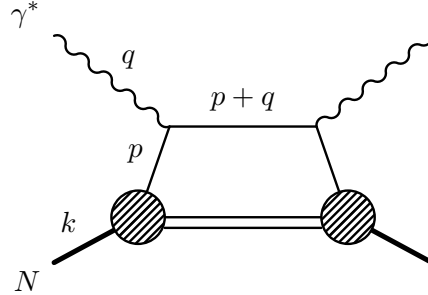


Figure 1.2: The handbag diagram in the parton model. The virtual photon  $\gamma^*$  transfers momentum  $q$  to the nucleon. The nucleon has momentum  $k$ , and the struck quark has momentum  $p$ .

It is conventional to use the momenta in Fig. 1.2 to define the variables

$$Q^2 \equiv -q^2 \quad (1.2)$$

$$\nu \equiv \frac{k \cdot q}{M_N} \quad (1.3)$$

$$x \equiv \frac{-q^2}{2k \cdot q} = \frac{Q^2}{2M_N \nu} \simeq \frac{p^+}{k^+} \quad (1.4)$$

where  $x$  is called the Bjorken variable. It has the interpretation in the parton model of the fraction of the nucleon momentum carried by the struck parton. The parton model is defined by the constituents with momentum  $p$  in Fig. 1.2 satisfying

$$(p + q)^2 = p^2 \quad (1.5)$$

$$\Rightarrow 2p \cdot q - Q^2 = 0 \quad (1.6)$$

so that if  $p = xk$ , then  $x$  is given by Eq. (1.4). We have also given  $x$  in terms of light cone variables,  $A^\pm = A^0 \pm A^3$ ,  $\mathbf{A}_\perp = (A^1, A^2)$  that are closely connected to the infinite momentum frame where the parton model is defined. The approximation in Eq. (1.4) is that at large  $Q^2$  and  $\nu$ , the struck quark has effectively zero transverse momentum after the interaction with the photon.

The Bjorken limit [17] is defined as  $Q^2, \nu \rightarrow \infty$  with  $Q^2/\nu$  finite, whereupon the functions  $W_i$  exhibit Bjorken-Feynman scaling, and we define the structure function of the nucleon  $F_2^{(N)}$

$$\frac{\nu}{M_N} W_2(\nu, Q^2) \rightarrow \sum_i e_i^2 \frac{Q^2}{2M_N \nu} q_i(Q^2/2M_N \nu) \equiv F_2^{(N)}(x) \quad (1.7)$$

where  $i$  runs over the quark flavors. This scaling breaks down experimentally as the function  $F_2^{(N)}$  acquires additional  $Q^2$  dependence. The Dokshitzer-Gribov-Lipatov-Altarelli-Parisi (DGLAP) evolution equations [42, 53, 4] (see Appendix C) derived from QCD describe the scaling violation by allowing one to calculate how the distribution of momentum  $q_i(x)$  among the quarks (and gluons) changes with the momentum scale  $Q^2$ . It is beyond the parton model, and is one of the most successful results of QCD. The structure function Eq. (1.7) is defined in terms of the quark distribution functions  $q_i(x)$ , which, in the parton model in Fig. 1.2, is given by

$$q_i(x) = k^+ \int \frac{dz^-}{2\pi} e^{ixk^+z^-} \langle k | \bar{\psi}(0)\gamma^+\psi(z^-) | k \rangle \quad (1.8)$$

The  $\psi$  are quark field operators, and  $\bar{\psi} \equiv \psi^\dagger \gamma^0$  (we will use  $\Psi$  for nucleon field operators). There are two interpretations of quark distributions:

- Probability distributions of partons carrying fraction  $x$  of the nucleon momentum in the infinite momentum frame, and
- QCD matrix elements of quark bilinears with light-like separation and the Operator Product Expansion (OPE) for the moments of the distributions.

We have so far used the first one, but these two definitions are equivalent in the  $\chi$ QS model because Feynman's hypothesis that the transverse momenta of partons do not grow with  $Q^2$  is satisfied [36].

The second approach is advantageous for the discussion of dynamical rescaling [29]. We can define the moments of the structure function of a nucleus  $F_2^{(A)}$  with momentum  $P$  in Wilson's operator product expansion

$$\begin{aligned} M_n^{(A)}(Q^2) &= \frac{1}{A} \int_0^A dx x^{n-2} F_2^{(A)}(x, Q^2) \\ &= \frac{A^{n-2}}{Q^2} \sum_{n,i} c_{n,i}(Q^2, \mu_A^2) \bar{\mathcal{O}}_{n,i}^{(A)}(\mu_A^2) \end{aligned} \quad (1.9)$$

where the sum runs on all twist-2 operators contributing to  $F_2$  (twist of an operator is given by  $t = d_i - n$ , where  $d_i$  is the mass dimension of the operator), and  $\bar{\mathcal{O}}$  is the matrix element

$$\langle P | \mathcal{O}_{i,\mu_1 \dots \mu_n}^{(A)}(\mu_A^2) | P \rangle = \bar{\mathcal{O}}_{n,i}^{(A)}(\mu_A^2) P_{\mu_1} \dots P_{\mu_n} \quad (1.10)$$

The essence of the dynamical rescaling description of the EMC effect is that the renormalization scale for nuclei is less than that for a free nucleon

$$\mu_A^2 < \mu_1^2 \ll Q^2$$

so that the nuclear operators  $\mathcal{O}^{(A)}$  undergo ‘extra evolution’ going up to the DIS scale  $Q^2$ , which accounts for the EMC effect. QCD does not tell us what  $\mu_A^2$  is, nor its relationship to  $\mu_1^A$ , but numerical studies [29] show that this process can describe both the EMC effect and Drell-Yan experiments [2].

The Wilson coefficients  $c$  in Eq. (1.9) in the OPE are dependent on the starting renormalization scale, and the essence of the dynamical rescaling picture of the EMC effect is that the scale is different in nuclei than for a free nucleon. Nuclear interactions are effective QCD interactions which renormalize a free nucleon into a bound one, but as we cannot yet in QCD calculate the parton distributions of a free nucleon, much less one in a nuclear medium. We need a model to probe the mechanism of that ‘renormalization’.

In the handbag diagram Fig. 1.2, the struck quark in the intermediate state is renormalized by QCD from the same starting scale as the other quarks in the nucleon, and hence all feel the effects of nuclear interactions at the low scale. In Chapter 4 we will calculate the effect of the presence of other nucleons on the quark distributions. One can imagine that we are calculating the effect of different starting scales for free and bound nucleons by showing what a bound nucleon parton distribution looks like at the scale of a free nucleon.

The use of a manifestly covariant formulation to derive the expression for the nuclear structure function appearing in Eq. (1.9) leads to a convolution formula [66]

$$\frac{F_2^{(A)}(x)}{A} = \int_x^A dy f(y) F_2^{(N)}(x/y) \quad (1.11)$$

The function  $f(y)$  is the nucleon momentum distribution in the nucleus, and is given by

$$f(y) = \int \frac{d^4 k}{(2\pi)^4} \delta \left( y - \frac{k^+}{M_N} \right) \text{Tr} \left[ \gamma^+ \chi^{(A)}(k, P) \right] \quad (1.12)$$

where the function  $\chi^{(A)}(k, P)$  is the Fourier transform of the connected part of the nucleon Green's function. The calculation of Eq. (1.12) is detailed in Appendix D.

The properly normalized nuclear structure function  $F_2^{(A)}(x)/A$  is smaller than the free nucleon structure function  $F_2^{(N)}(x)$  for values of  $0.3 \lesssim x \lesssim 0.7$ . This is the EMC effect [7], and it has been known for more than twenty years. The underlying mechanism responsible for the change of the distribution of momenta among the constituents of the nucleus remains beyond our ability to calculate in QCD. We must resort to models, and there is a clear interpretation within the parton model: a valence quark in a bound nucleon carries less momentum than a valence quark in a free one. One popular mechanism for this reduction in momentum involves ordinary nuclear binding which, in its simplest form, is represented by using the nucleon momentum distribution Eq. (1.12) to evaluate the free nucleon structure function at a value of  $x$  increased by a factor of the average separation energy divided by the nucleon mass  $\bar{e}/M_N \simeq 0.04$ . This picture encapsulates any nuclear effects in the nuclear structure  $F_2^{(A)}/A$  in the function  $f(y)$ .

The validity of the binding effect has been questioned in the reviews [6, 50, 83, 48], and we have shown [79, 98] that conventional relativistic nuclear mean field theory fails to describe the phenomenology of the EMC effect in terms of  $f(y)$  in Eq. (1.11). These results are summarized in Appendix D. We believe that this failure to describe the EMC effect provides additional motivation to study quarks and antiquarks in nuclei beyond trying to connect QCD to nuclear physics, and to look for medium modifications of the bound nucleon in the only other part of Eq. (1.11) available: the structure function  $F_2^{(N)}$ . We must also remain consistent with the Drell-Yan experiments, which we describe next.

## 1.2 The Drell-Yan Process and Dimuon Production

The proton-nucleus Drell-Yan cross-section can tell us about the antiquark content of the nucleus, and hence serves as another handle on nuclear parton distributions. The experimental data are consistent with no modification of the antiquark distribution [2]. Many models fail to describe, or even address, dimuon production in the Drell-Yan process depicted in Fig. 1.3. Dynamical rescaling matches the trend of the data [2], but, as in its

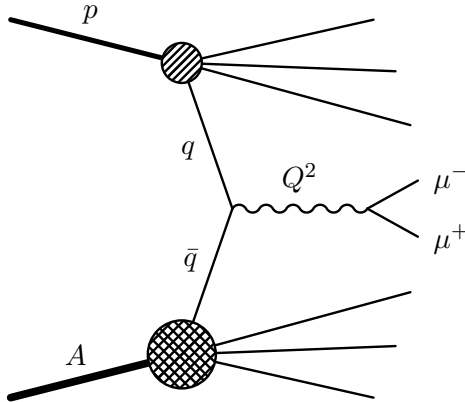


Figure 1.3: Drell-Yan process  $p + A \rightarrow \mu^+ \mu^- + X$ . A quark  $q$  from the proton, and an antiquark  $\bar{q}$  from the nucleus annihilate to form a muon pair.

description of DIS data, it does not give any insight as to the mechanism. If  $x_p$  is the momentum fraction carried by the (anti)quark in the proton, and  $x_A$  is the same for the nucleus, then one finds the cross section from Fig. 1.3 [12]

$$\frac{d^2\sigma}{dx_p dx_A} = \frac{4\pi\alpha^2 K}{9s} \frac{1}{x_p x_A} \sum_i e_i^2 \left[ q_i^{(p)}(x_p, Q^2) \bar{q}_i^{(A)}(x_A, Q^2) + \bar{q}_i^{(p)}(x_p, Q^2) q_i^{(A)}(x_A, Q^2) \right] \quad (1.13)$$

where  $\alpha \simeq 1/137$  is the electromagnetic coupling, and  $\sqrt{s}$  is the energy in the center-of-mass frame of the proton and nucleus. The factor  $K$  is an enhancement factor accounting for other dilepton production modes independent of  $x_p$  and  $x_A$  and the target and projectile, see [12], and references therein. If we look experimentally at  $x_p \gtrsim x_A + 0.2$ , then at high  $Q^2$  the first term dominates (the antiquark distribution for the proton is effectively zero for  $x_p \gtrsim 0.2$  and  $Q^2$  large). This can be achieved by controlling the kinematics of the experiment, so we can use the Drell-Yan process to examine the antiquark content of the nucleus. In order to describe the experimental data, we must have a model that includes both quarks and antiquarks at the model scale<sup>1</sup>. We introduce such a model in Chapter 2.

<sup>1</sup>The evolution equations in Appendix C generate antiquark, as well as gluon, distributions as the scale changes. While different starting distributions will generate different antiquark distributions, a lack of antiquarks in the model ignores possible nuclear effects at the starting scale. A common reason for failing to describe the Drell-Yan data is that models produce too large an enhancement in the antiquark content, so addressing antiquarks with a model at the model scale is essential.

## Chapter 2

### THE CHIRAL QUARK-SOLITON MODEL

We will begin our study in earnest by providing motivation for the  $\chi$ QS model, following the reviews [39, 34]. First, we will discuss instantons, and how they break chiral symmetry. Constructing the model itself, and deriving some of its basic properties in the meson and baryon sectors is next. The meson sector connects us to  $\chi$ PT, and the baryon sector connects us to our description of nuclear elastic, and deep inelastic scattering experiments.

#### **2.1 Results From The Instanton Vacuum**

Quantum Chromodynamics is a Yang-Mills gauge theory with gauge symmetry  $SU(N_C)$ , where the number of colors is  $N_C = 3$ . In Euclidean space<sup>1</sup>, the QCD field equation for the gluons contains solutions called instantons. These solutions never appear at any order in the perturbation theory expansion in the strong coupling  $\alpha_s$ , and hence may provide insight into non-perturbative QCD. Instantons can exist concentrated at a single point in spacetime and are sometimes called pseudoparticles as they do not follow spacetime worldlines like ordinary particles. Lattice simulations provide evidence that the QCD vacuum is populated by instantons with a size  $\bar{\rho} \sim 0.3$  fm, which is approximately the scale of chiral symmetry breaking, and a separation  $\bar{R} = (N/V)^{1/4} \sim 1$  fm where  $N/V$  is the instanton number density. The instanton packing fraction, equal to the four dimensional instanton volume  $\pi^2 \bar{\rho}^4$  times the instanton number density, is then

$$\frac{\pi^2 \bar{\rho}^4}{\bar{R}^4} \simeq \frac{1}{8},$$

which gives a small parameter aside from  $\alpha_s$  in perturbative QCD to use in expansions. This is the basis for the Instanton Liquid Model (ILM) picture of the QCD vacuum. Though

---

<sup>1</sup>Euclidean spacetime related to ordinary Minkowski spacetime with time  $t$  by taking  $t = i\tau$  with  $\tau$  being the Euclidean time.

dilute based on the packing fraction, the instantons are still strongly interacting, therefore a liquid, not a gas, picture is more accurate.

Because of their topological properties, the instantons are accompanied by  $2N_f$  zero modes of chiral fermions ( $N_f$  each of left and right handed fermions), where  $N_f$  is the number of flavors of quarks. Instantons are localized near a single point in spacetime and have  $2N_f$  fermions meeting at that point, so they look like interaction vertices appearing in Feynman rules. In the case of  $N_f = 2$ , we have effective four-quark interactions. These are the so-called 't Hooft vertices [104]; a Feynman diagram for one with  $N_f = 2$  (which we will use throughout) is in Fig. 2.1. A random ensemble of instantons [37] provides a mechanism to break chiral symmetry via these zero modes. Effectively one creates a helicity-flipping term in the Lagrangian that behaves like a mass term via scattering of chiral quarks by the 't Hooft vertices. They create a dynamical quark mass

$$M(p) = \lambda \sqrt{\frac{N\pi^2\bar{\rho}^2}{VN_C}} \phi(p\bar{\rho}/2)^2 \quad (2.1)$$

$$\phi(z) \equiv 2z \left[ I_0(z)K_1(z) - I_1(z)K_0(z) - \frac{1}{z}I_1(z)K_1(z) \right] \quad (2.2)$$

where  $\phi(z)$  is the Fourier transform of the quark zero mode wave function bound to each instanton,  $N/V$  is the instanton density, and  $N_C$  is the number of colors in the gauge theory. The constant  $\lambda$  is obtained from a detailed numerical calculation [34], which results in a dynamical constituent quark mass with  $M(0) \simeq 350$  MeV. The dynamical quark mass falls to zero for  $p \gg 1/\bar{\rho} \simeq 650$  MeV which acts as an effective momentum cutoff for the theory.

If one combines a quark and an antiquark line from a 't Hooft vertex Fig. 2.1, one obtains a quark-meson vertex pictured in Fig. 2.2 where the type of meson depends on the quantum numbers. If one considers the correlation function of two quarks

$$\Pi^\Gamma(p) = - \int d^4x e^{-ip\cdot x} \text{tr } \overline{S(x,0)\Gamma S(0,x)\Gamma} \quad (2.3)$$

$$\Gamma = 1, \gamma_5, \gamma^\mu, \gamma_5\gamma^\mu, \sigma_{\mu\nu} \quad (2.4)$$

where  $S(x,y)$  is the quark Green's function and the bar indicates an average over the instanton ensemble in the ILM, one finds a pole in the pseudoscalar channel at  $p^2 = 0$  corresponding to our massless pions resulting from the dynamical breaking of chiral symmetry,

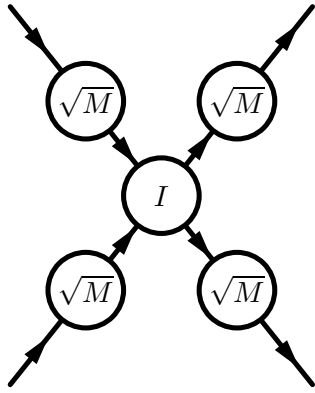


Figure 2.1: A 't Hooft vertex [104] for  $N_f = 2$ . The instanton is labelled by  $I$ , and the quark zero mode wave functions are represented by form factors  $\sqrt{M}$ . The arrows indicate the helicity of the quarks.

and in the scalar channel at  $p^2 \simeq 4M^2(0)$  which is taken as the mass a scalar meson. There are no poles in the vector or tensor channels [37]. We will denote scalar, pseudoscalar, and vector with subscripts  $s$ ,  $ps$ , and  $v$  in the following.

## 2.2 The Model Lagrangian

Using the quark meson vertex in Fig. 2.2, we can write down a Lagrangian [39] with constituent (anti)quarks  $\bar{\psi}, \psi$  and pions  $\pi(x)$

$$\begin{aligned} \mathcal{L}[\bar{\psi}, \psi, \pi] &= \bar{\psi} i\partial^\mu \psi - \int d^4 p_1 d^4 p_2 e^{i(p_1 - p_2) \cdot x} \bar{\psi}(p_1) \sqrt{M(p_1)} U^{\gamma_5}(x) \sqrt{M(p_2)} \psi(p_2) \\ U^{\gamma_5}(x) &\equiv \exp \left( i \gamma_5 \frac{\tau \cdot \pi(x)}{f_\pi} \right) \end{aligned} \quad (2.5)$$

where  $f_\pi \simeq 93$  MeV is the pion decay constant and  $\tau_i = \sigma_i/2$  are the isospin operators ( $\sigma_i$  are the Pauli spin matrices). This theory exhibits asymptotic freedom like QCD; the interaction disappears at large momenta with the function  $M(p)$  falling to zero leaving a theory of free massless quarks. We would like to replace this complicated nonlocal theory with a local one; this is done by replacing the momentum dependent mass  $M(p)$  with a constant  $M$ . The ultraviolet cutoff  $M(p \rightarrow \infty) \rightarrow 0$  is replaced by a Pauli-Villars regularization fixed by

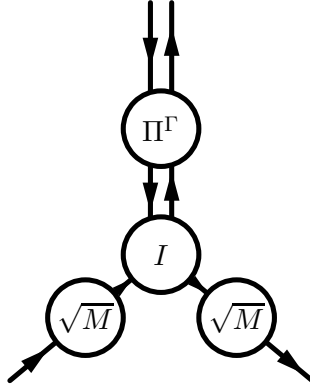


Figure 2.2: Quark-meson vertex formed from a 't Hooft vertex (Fig. 2.1), where  $\Gamma = 1, \gamma_5, \gamma^\mu, \gamma_5\gamma^\mu, \sigma^{\mu\nu}$  represent the channels onto which the quark zero modes are projected.

the physical value of

$$\begin{aligned}
 & i\tau^a \gamma^5 \\
 \text{---} \circlearrowleft &= f_\pi^2 = 4N_C \int \frac{d^4 k}{(2\pi)^4} \frac{M^2}{(k^2 - M^2)^2} - \frac{M^2}{M_{PV}^2} \frac{M_{PV}^2}{(k^2 - M_{PV}^2)^2} \\
 & i\tau^b \gamma^5 = \frac{N_C M^2}{4\pi^2} \log \frac{M_{PV}^2}{M^2}
 \end{aligned} \tag{2.6}$$

Using  $M = 420$  MeV, the resulting value for  $M_{PV} \simeq 580$  MeV is comparable to the instanton size cutoff, and the resulting mass function is close not only to the instanton model Eq. (2.2), but to an extrapolation of quenched lattice data to the chiral limit (see Appendix A). The three functions are plotted in Fig. 2.3. This value for the constituent quark mass has also been shown to reproduce many of the properties of free nucleons [26], which will be discussed in Chapters 4 and 5. We introduce the notation

$$A - PV \equiv A(M) - \frac{M^2}{M_{PV}^2} A(M_{PV})$$

as a shorthand to represent the Pauli-Villars subtraction, where  $A$  is any logarithmically divergent quantity in the  $\chi$ QS model. We use this method to regulate the divergences as it preserves the completeness of the quark states, which is important in the calculation of the quark distributions [36].

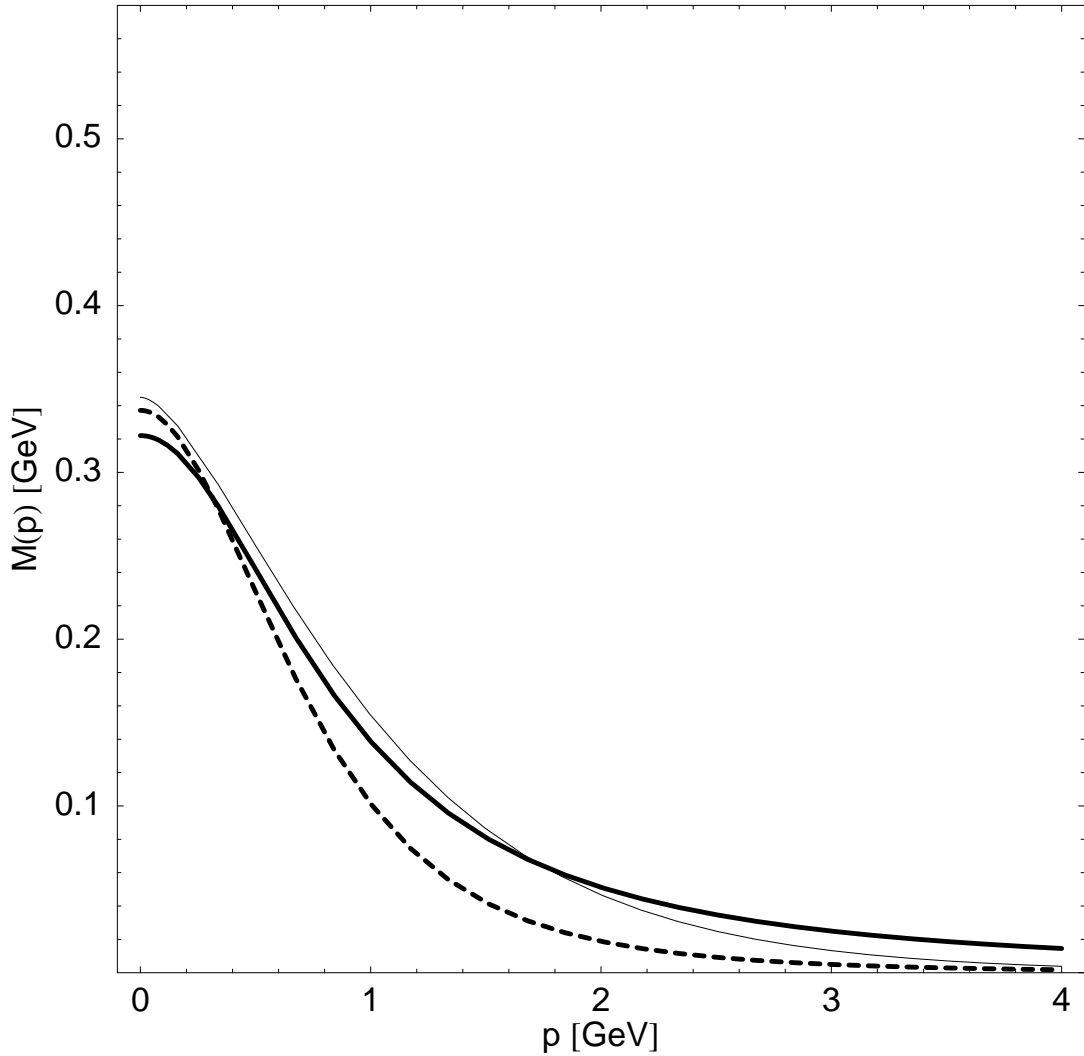


Figure 2.3: The mass function  $M(p)$  using one Pauli-Villars regulator fit to the pion decay constant (heavy line), the instanton model (light line) [37] and the extrapolation of fits to quenched lattice data [86] to the chiral limit using three Pauli-Villars propagators (heavy dashed line), see Appendix A.

In the case of the nucleon state the pion field is taken to be the ‘hedgehog’ *ansatz* with profile function  $\Theta(r)$  and unit winding number.

$$U(x) = \exp(i\mathbf{n} \cdot \boldsymbol{\tau}\Theta(r)) \quad (2.7)$$

$$\Theta(0) = -\pi \quad (2.8)$$

$$\Theta(r \rightarrow \infty) = 0 \quad (2.9)$$

Unit winding number is guaranteed by the condition Eq. (2.8). The local version of the theory (2.5) with constant mass, Pauli-Villars regulator and hedgehog profile function results in the Lagrangian for the Chiral Quark-Soliton ( $\chi$ QS) model

$$\mathcal{L} = \bar{\psi}(i\partial - M e^{i\gamma_5 \mathbf{n} \cdot \boldsymbol{\tau}\Theta(r)})\psi \quad (2.10)$$

The pion field configuration corresponds to the soliton (Skyrmion) in the Skyrme model, hence its appearance in the name of the model (quarks, however, do not appear as degrees of freedom in the Skyrme model). This is a non-renormalizable effective field theory, so that the ultraviolet cutoff, the Pauli-Villars mass, has a physical meaning (observables can depend on it), namely the instanton size. The constituent quark mass  $M$  could be taken to be a free parameter when we tackle medium modifications in Chapters 4 and 5, but we have chosen to fix it at 420 MeV. This value best reproduces a wide variety of nucleon observables [27, 26], and produces a mass function similar to Eq. (2.2) in Fig. 2.3. It is worth noting that we could have just written down the Lagrangian (2.10) without motivation from the instanton picture of the QCD vacuum as the simplest field theory of constituent quarks consistent with chiral symmetry (a chiral transformation  $\psi \rightarrow e^{i\gamma_5 \alpha(x)}\psi$  can be absorbed into a redefinition of the pion field  $\boldsymbol{\tau}$ ).

Quarks are described by single particle wave functions  $\psi_n$  that are solutions to the Dirac equation

$$(i\partial - M e^{i\gamma_5 \mathbf{n} \cdot \boldsymbol{\tau}\Theta(r)})\psi_n(\mathbf{r})e^{-iE_n t} = 0 \quad (2.11)$$

$$e^{iE_n t}\bar{\psi}_n(\mathbf{r})(i\partial - M e^{i\gamma_5 \mathbf{n} \cdot \boldsymbol{\tau}\Theta(r)}) = 0 \quad (2.12)$$

with energy eigenvalues  $E_n$ . They are represented as a discrete set labelled by  $n$  for simplicity, but the spectrum of the Dirac operator contains a single bound state (which we will

refer to as the valence level, and label with a superscript  $v$ ), as well as a positive and negative energy continua for energies  $|E| > M$ . At most one bound state is guaranteed the the unit winding number Eq. (2.8) of the hedgehog field (there may be no bound state solution for certain values of  $M$ ). Unit winding number is a necessary, not sufficient, condition to obtain unit baryon number given by the number of quarks in the valence level; the winding number is not the baryon number as it is in the Skyrme model.

The states in the negative continuum are filled in both the vacuum sector with  $U = 1$  and the nucleon sector with profile function  $\Theta(r)$ . For any observable, one must subtract the contribution from the vacuum ( $U = 1$ ) to obtain a physical result. These observables can still be logarithmically divergent after the vacuum subtraction, requiring Pauli-Villars regularization. It is the filled negative energy continuum that allows one to describe the nucleon quark sea: the virtual quarks and antiquarks that appear out of the polarized QCD vacuum in the presence of a nucleon. Positive energy antiquarks appear as a hole: a lower density of states in the negative energy continuum. Conversely, negative energy quarks appear as a higher density of states. The pions in the theory are lighter than  $2M$  because they are density fluctuations in the negative continuum consisting of a positive energy antiquark and a negative energy quark so that their mass is given by  $m_\pi \simeq M - M = 0$  [35].

There is an equivalence in calculating observables where one can use sums over the occupied states (the valence level and negative energy continuum) or the unoccupied states (the positive continuum) [36]. This equivalence is deeply rooted in the fact that the model is a relativistic quantum field theory, and is needed to preserve general conditions such as the positivity of the antiquark distribution and the baryon and momentum sum rules discussed in Chapter 4. It can be spoiled by the regulator, such as Schwinger's proper-time regulator or sharp cutoffs, but Pauli-Villars regularization preserves the completeness of the quark states and maintains the equivalence [36].

The field equation for the profile function follows directly from the Lagrangian (2.10) and is given by

$$\rho_s(r) \sin \Theta(r) - \rho_{ps}(r) \cos \Theta(r) = 0 \quad (2.13)$$

where the quark scalar and pseudoscalar densities are

$$\begin{aligned}\rho_{s,ps}(r) &= \sum_n \bar{\psi}_n(r)\Gamma\psi_n(r) \\ \Gamma &= 1, i\gamma_5 \mathbf{n} \cdot \boldsymbol{\tau}\end{aligned}\tag{2.14}$$

For a single nucleon this sum is over all occupied states which includes the negative energy continuum and the single valence level. In the nuclear medium, this becomes more complicated, and the general case would be exceedingly difficult. In symmetric infinite nuclear matter, with equal constant densities of protons and neutrons filling all space, we will be able to make some simplifications. This is an often used approximation to describe heavy nuclei [108].

### 2.3 The Nucleon and the Large $N_C$ Limit

Aside from the gauge coupling used in perturbative QCD, there is another ‘small’ dimensionless parameter that we can expand in: the inverse number of colors  $N_C^{-1}$ . It is believed that many of the important properties of QCD follow into the limit where  $N_C$  is large; we will leave the basics of this expansion regarding baryons to Ref. [109]. We will use the limit here to justify the  $\chi$ QS model as a relativistic mean field theory of baryons [35], simplifying the calculation of the nucleon mass, form factors and quark distributions. We will follow Ref. [38] to obtain an expression for the nucleon mass.

In Euclidean space (in which we will work in this section), the partition function for the  $\chi$ QS model is

$$Z = \int D\pi D\bar{\psi} D\psi \exp - \int d^4x \bar{\psi}(i\cancel{\partial} + iMU^{\gamma_5})\psi\tag{2.15}$$

The integration over the quark fields can be done, giving the effective action for the pion fields (including the vacuum subtraction)

$$S_{\text{eff}}[\pi] = -N_C \log \det \left( \frac{i\cancel{\partial} + iMU^{\gamma_5}}{i\cancel{\partial} + iM} \right)\tag{2.16}$$

One can expand this in derivatives

$$\begin{aligned}\text{Re } S_{\text{eff}}^{(2)}[\pi] &= \frac{N_C}{4} \int d^4x \int \frac{d^4k}{(2\pi)^4} \text{tr} \left( \frac{M\cancel{\partial}U^{\gamma_5}}{k^2 + M^2} \right)^2 \\ &= \frac{1}{4}f_\pi^2 \int d^4x \text{tr } \partial_\mu U \partial^\mu U^\dagger\end{aligned}\tag{2.17}$$

and see that one obtains the  $\mathcal{O}(p^2)$  term in the momentum expansion in  $\chi$ PT (note this also defines Eq. (2.6) for  $f_\pi$ ). If one includes a current quark mass, one obtains a Lagrangian consistent with the  $\mathcal{O}(p^4)$  Gasser-Leutwyler Lagrangian and large  $N_C$ . This is elaborated on in Appendix A, but we have already made the connection between  $\chi$ PT and QCD through the  $\chi$ QS model.

From the effective action, we can also determine the energy in the background pion field in the limit of long Euclidean times  $T$ . We write Eq. (2.16) in terms the Hamiltonian  $H$ , and  $H^{(0)}$  with  $U = 1$

$$S_{\text{eff}}[\pi] = -N_C \text{Tr} \left[ \log(i\partial_4 + iH) - \log(i\partial_4 + iH^{(0)}) \right] \quad (2.18)$$

$$= -N_C T \int \frac{dE}{2\pi} \text{Tr} \left[ \log(E + iH) - \log(E + iH^{(0)}) \right] \quad (2.19)$$

$$= -N_C T \int \frac{dE}{2\pi} \text{Tr} \left( \frac{E}{E + iH} - \frac{E}{E + iH^{(0)}} \right) \quad (2.20)$$

$$= -N_C T \left( \sum_{E_n < 0} E_n - \sum_{E_n^{(0)} < 0} E_n^{(0)} \right) \quad (2.21)$$

$$\equiv -N_C T E_{\text{field}}[\pi] \quad (2.22)$$

One expects the limit of the correlation function of two nucleon currents to give the nucleon mass at long times  $T$

$$\lim_{T \rightarrow \infty} \langle J(0, T) J^\dagger(0, 0) \rangle \sim e^{-M_N T} \quad (2.23)$$

where the nucleon current is given by

$$J(x) = \frac{1}{N_C!} \varepsilon^{\alpha_1 \cdots \alpha_{N_C}} \Gamma_{JJ_3TT_3}^{f_1 \cdots f_{N_C}} \psi_{\alpha_1 f_1}(x) \cdots \psi_{\alpha_{N_C} f_{N_C}}(x) \quad (2.24)$$

where  $\alpha_i$  are color indices,  $f_i$  are flavor indices,  $J$  and  $J_3$  are angular momentum quantum numbers, and  $T$  and  $T_3$  are the isospin. We subsume the description of the nucleon quantum numbers in terms of its constituent quarks into the matrix  $\Gamma$ . The correlation function is defined in terms of the partition function, and the integration over the quark fields can be done. This results in the effective action and the quark Green's function in the background

pion field

$$\begin{aligned}\langle J(0, T)J^\dagger(0, 0) \rangle &= \frac{1}{Z} \int D\pi D\psi D\psi^\dagger J(0, T)J^\dagger(0, 0) e^{-S[\pi, \psi, \psi^\dagger]} \\ &= \Gamma_{\{JT\}}^{\{f\}} \Gamma_{\{JT\}}^{\{g\}} \int D\pi \prod_i^{N_C} G_{f_i g_i}(T, 0 | \pi) e^{-S_{\text{eff}}[\pi]}\end{aligned}$$

The long time limit of the quark Green's function in the background pion field gives us the valence energy level

$$\lim_{T \rightarrow \infty} G_{f_i g_i}(T, 0 | \pi) \sim e^{-TE^v[\pi]} \quad (2.25)$$

Putting this together we obtain

$$\begin{aligned}\lim_{T \rightarrow \infty} \langle J(0, T)J^\dagger(0, 0) \rangle &\sim \int D\pi e^{-TN_C(E^v[\pi] + E_{\text{field}}[\pi])} \\ &\sim e^{-M_N T}\end{aligned}$$

which gives us, in the saddle point approximation (leading order in  $N_C$ ), the nucleon mass

$$M_N[\pi(x)] = \min_{\{\pi(x)\}} N_C (E^v[\pi] + E_{\text{field}}[\pi]) \quad (2.26)$$

We have neglected quark loop corrections at large  $N_C$  in the saddle point approximation (and therefore quantum fluctuations of the pion field, which propagate through quark loops). In this sense, the large  $N_C$  limit effectively represents a relativistic mean field approximation. The abstract functional Eq. (2.26) is minimized by solving the system self-consistently with the pion field replaced by the profile function  $\Theta(r)$ . This is the subject of Chapter 3.

## Chapter 3

### QUARKS AND ANTIQUARKS IN NUCLEI

In order to describe nuclei in terms of the quarks and antiquarks in the  $\chi$ QS model, there needs to be a way to connect the nuclear physics and the quark physics. This has been done in the context of the MIT bag model [91] to create a so-called Quark-Meson Coupling (QMC) model. We will use some of the ideas of that model, but also include some phenomenology of medium modifications and physics of the QCD vacuum. We begin with the role of the vacuum quark scalar condensate, and then construct a two-tier self-consistent calculation. We are able to obtain nuclear binding and saturation, and reproduce standard properties of nuclear matter. We therefore create a model of nuclei that includes the physics of valence and sea quarks.

#### **3.1 The Effect of the Medium**

We will begin with some motivation for our procedure to couple the quark substructure of the nucleon to the nuclear medium. Through the use of QCD sum rules, Ioffe [63] derived a relationship between the vacuum scalar condensate,  $\langle\bar{\psi}\psi\rangle_0$ , and the nucleon mass. One can re-derive this estimate in a constituent quark field theory such as we are using here. We begin with the scalar condensate

$$\begin{array}{c} \text{Diagram: A loop with a dot at the bottom-left corner labeled '1'.} \\ = \langle\bar{\psi}\psi\rangle_0 = -\text{tr} \int^{\Lambda} \frac{d^4 p}{(2\pi)^4} \frac{1}{p' - M} \\ \sim -\frac{N_C M \Lambda^2}{4\pi^2}, \end{array} \quad (3.1)$$

where the divergent loop integral is regulated by a momentum cutoff (playing the role of the Borel mass in the QCD sum rule approach). Using the fact that constituent quarks are essentially defined as having a mass  $\sim M_N/N_C$ , we can rewrite Eq. (3.1) as

$$M_N \sim -\frac{4\pi^2}{\Lambda^2} \langle\bar{\psi}\psi\rangle_0. \quad (3.2)$$

Although Eq. (3.2) is not a very accurate estimate, it does highlight the role of the condensate. It will be modified in the presence of other nucleons.

The condensate at finite density, proportional to  $k_F^3$  where  $k_F$  is the Fermi momentum, can be written in terms of the nuclear scalar density  $\rho_s^N$  and the nucleon sigma term  $\sigma_N$  [31] as

$$\langle\bar{\psi}\psi\rangle_{k_F} = \langle\bar{\psi}\psi\rangle_0 - \langle\bar{\psi}\psi\rangle_0 \frac{\sigma_N}{m_\pi^2 f_\pi^2} \rho_s^N. \quad (3.3)$$

We can then substitute Eq. (3.3) into Eq. (3.2) to obtain a schematic picture of the effect of the nuclear medium on the nucleon mass

$$M_N(k_F) \sim -\frac{4\pi^2}{\Lambda^2} \langle\bar{\psi}\psi\rangle_0 \left[ 1 - \frac{\sigma_N}{m_\pi^2 f_\pi^2} \rho_s^N \right], \quad (3.4)$$

We will effectively replace the combination of the vacuum condensate, pion mass, decay constant and the the sigma term in Eq. (3.4) with a dimensionless scalar coupling constant  $g_s$ , which we take as a free parameter. The value of  $g_s$  is determined from a fit to nuclear density and binding energy.

Using this dependence of the nucleon mass on the nuclear medium as a guide, we incorporate the medium dependence in the model by simply letting the quark scalar density in the field equation (2.13) contain a (constant) contribution arising from other nucleons present in symmetric nuclear matter. This models a scalar interaction via the exchange of multiple pairs of pions between nucleons. We take the scalar density to consist of three terms: 1) the constant condensate value  $\langle\bar{\psi}\psi\rangle_0$  (in the vacuum or at large distances from a free nucleon), 2) the valence contribution  $\rho_s^v$  and 3) the contribution from the medium which takes the form of the convolution of the nucleon  $\rho_s^N$  and valence quark scalar densities as in the QMC model [73]

$$\rho_s^q(\mathbf{r}) \simeq \langle\bar{\psi}\psi\rangle_0 + \rho_s^v(\mathbf{r}) + g_s \int d\mathbf{r}' \rho_s^N(\mathbf{r} - \mathbf{r}') \rho_s^v(\mathbf{r}') \quad (3.5a)$$

$$= \langle\bar{\psi}\psi\rangle_0 + \rho_s^v(r) + g_s P_s^N(k_F) \quad (3.5b)$$

We define an effective condensate in the presence of nuclear matter by

$$\langle\bar{\psi}\psi\rangle_0 + g_s P_s^N(k_F). \quad (3.6)$$

We take the pseudoscalar density to have only the valence term  $\rho_{ps}^q \simeq \rho_{ps}^v$ ; the two other contributions analogous to the first and third terms of Eq. (3.5) vanish due to symmetries of the QCD vacuum and nuclear matter. These approximations to the densities neglect the precise form of the negative continuum wave functions. We will see that the resulting free nucleon profile function has little discernible difference from a fully self-consistent treatment (see Fig. 3.5 in Section 3.3), demonstrating the excellence of this approximation. We provide a schematic picture of the scalar density in a free and bound nucleon in Fig. 3.1. Incorporating this dependence on nuclear matter in the field equation Eq. (2.13), the in-medium field equation for the profile function becomes

$$\Theta(r, k_F) = \arctan \frac{\rho_{ps}^q(r)}{\rho_s^q(r) + g_s P_s^N(k_F)}, \quad (3.7)$$

which is similar to the way the pion mass would enter, except with the opposite sign (*i.e.* medium effects serve to bring us closer to chiral symmetry restoration).

The (constant) nucleon scalar density in Eq. (3.5) is determined by solving the nuclear self-consistency equation [108]

$$\rho_s^N = 4 \int^{k_F} \frac{d^3 k}{(2\pi)^3} \frac{M_N(\rho_s^N)}{\sqrt{k^2 + M_N(\rho_s^N)^2}}. \quad (3.8)$$

The dependence of the nucleon mass, and any other properties calculable in the model, on the Fermi momentum  $k_F$  enters through Eq. (3.8). Thus there are two coupled self-consistency equations: one for the profile, Eq. (3.7), and one for the density, Eq. (3.8). These are iterated until the change in the nucleon mass Eq. (3.15) is as small as desired (in our case,  $\Delta M_N \leq 0.1$  MeV) for each value of the Fermi momentum.

We introduce a phenomenological vector meson field  $V^\mu$  (with mass fixed at  $m_v = 0.77$  GeV and coupling  $g_v$ ) [108] exchanged between nucleons, but not quarks in the same nucleon (*i.e.* we ignore the spatial dependence of the vector field in the vicinity of a nucleon, treating only the nuclear mean field). In the mean field approximation (MFA)  $V^{i=1,2,3} = 0$ , and the vector potential has a simple field equation [108]

$$V^0 = \frac{g_v}{m_v^2} P_v^N(k_F) \quad (3.9)$$

where the vector meson couples to the vector density

$$P_v^N(k_F) = \int d^3 r' \rho_v^N(r') \rho_v^q(r - r') = \frac{2k_F^3}{3\pi^2}. \quad (3.10)$$

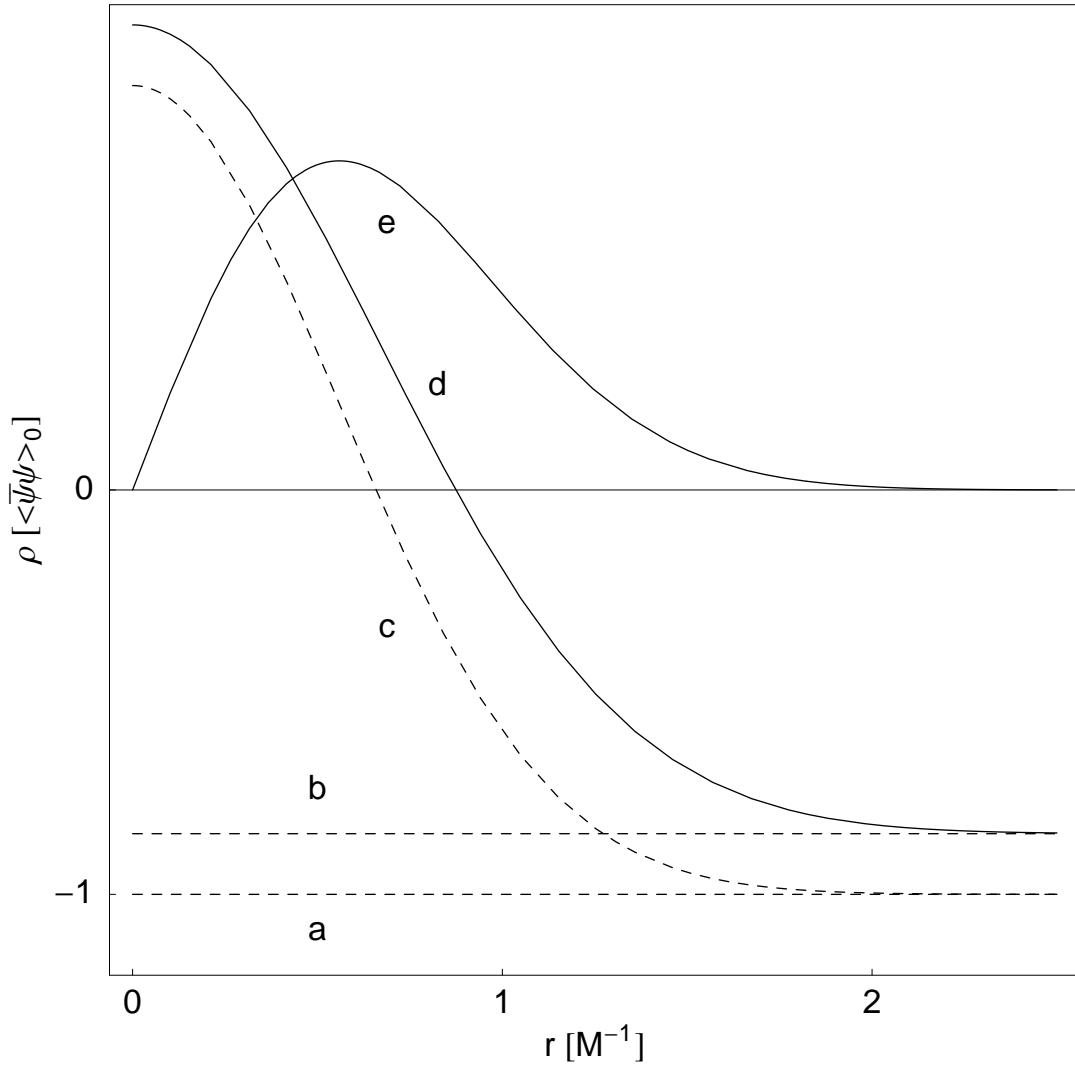


Figure 3.1: Cartoon of the scalar and pseudoscalar densities as a function of radius from the center of the nucleon. The inverse constituent quark mass sets the typical size scale. Pictured are (a) the vacuum condensate, (b) the effective condensate Eq. (3.6), (c) the free nucleon scalar density, (d) the bound nucleon scalar density, and (e) the pseudoscalar density.

It is a proxy for uncalculated soliton-soliton interactions used to obtain the necessary short distance repulsion which stabilizes the nucleus. The resulting energy per nucleon is

$$\frac{E}{A} = \frac{4}{\rho_B(k_F)} \int^{k_F} \frac{d^3 k}{(2\pi)^3} \sqrt{k^2 + M_N(k_F)^2} + \frac{1}{2} \frac{g_v^2}{m_v^2} P_v^N(k_F). \quad (3.11)$$

The single-particle Dirac Hamiltonian for the quarks in the hedgehog pion field, after including the vector interaction, is

$$\begin{aligned} H[\Theta]\psi_n(\mathbf{r}) &\equiv [-i\gamma^0\gamma^k(\partial_k + ig_v V_k) + g_v V_0 + M\gamma^0(\cos\Theta + i\gamma_5\boldsymbol{\tau}\cdot\mathbf{n}\sin\Theta)]\psi_n(\mathbf{r}) \\ &= E_n\psi_n(\mathbf{r}) \end{aligned} \quad (3.12)$$

where the effect of the nuclear medium, the dependence on  $k_F$ , enters through the vector potential, as well as the profile function  $\Theta = \Theta(r, k_F)$ .

### 3.2 The Numerical Procedure

The Dirac Hamiltonian is diagonalized in the discrete Kahana-Ripka basis [67] (see Appendix B). The basis functions  $\phi_i$  are defined by the solutions to the free single-particle Dirac Hamiltonian

$$H^{(0)}\phi_i(\mathbf{r}) = [-i\gamma^0\gamma^k\partial_k + M\gamma^0]\phi_i(\mathbf{r}) = E_i^{(0)}\phi_i(\mathbf{r}) \quad (3.13)$$

The full Hamiltonian is then solved by diagonalizing the matrix equation

$$\sum_j H_{ij}[\Theta]c_{nj} = E_n c_{ni} \quad (3.14)$$

where

$$H_{ij}[\Theta] = \int d\mathbf{r} \phi_i^\dagger(\mathbf{r}) H[\Theta] \phi_j(\mathbf{r})$$

and

$$\psi_n(\mathbf{r}) = \sum_i c_{ni} \phi_i(\mathbf{r})$$

The use of a finite basis turns the positive and negative energy continua into a discrete set of states. Our interpretation of these continua as quarks and antiquarks in the nucleon sea remains the same. Antiquarks (holes) appear as lower densities of discrete energy levels

in the negative energy states. In the finite basis, we can write the nucleon mass Eq. (2.26) as

$$M_N[\Theta(r, k_F)] = N_C \left[ E^v + \sum_{E_n < 0} E_n - \sum_{E_n^{(0)} < 0} E_n^{(0)} \right] - PV. \quad (3.15)$$

Starting at zero Fermi momentum and an initial guess for the profile function as the first step in the self consistent calculation, the valence level wave function is used to calculate the quark scalar and pseudoscalar densities (there is no medium contribution at  $k_F = 0$ ). These are used in Eq. (3.7) to calculate a new profile function.

This new profile function then gives us new quark densities after diagonalizing the Hamiltonian Eq. (3.12). This procedure is iterated until self consistency is reached when the change in the valence energy level  $\Delta E^v \leq 0.01$  MeV (the first self-consistent loop). Next, the eigenvalues are used to calculate  $M_N$ . At  $k_F = 0$ , the procedure is done here and  $k_F$  is incremented a step  $\Delta k_F = 0.01$  fm.

With  $k_F \neq 0$ , there is now a contribution to the scalar density from the medium in the profile field equation (3.7), as well as a non-zero vector potential. We calculate the nucleon scalar density via Eq. (3.8), using the nucleon mass from the previous step,  $M_N(k_F - \Delta k_F)$ , as the initial guess. The Hamiltonian is again diagonalized and the profile is calculated self consistently using the valence level and the medium contribution. The nucleon mass is then calculated, and the nucleon scalar density is recalculated using the new nucleon mass. This is repeated at each  $k_F$  until self consistency is reached when the change in the nucleon mass is  $\Delta M_n \leq 0.1$  MeV (the second self-consistent loop). Then,  $k_F$  is incremented another step, and the process continues until one reaches any value of  $k_F$  desired. A diagram of this process is in Fig. 3.2, which clarifies the double self-consistent loop structure.

### 3.3 The Numerical Results

The mass of a free nucleon is computed to be  $M_N(k_F = 0) = 1209$  MeV. The  $\sim 30\%$  difference is as expected in the model at leading order in  $N_C$ . We evaluate the nucleon mass Eq. (3.15) and energy per nucleon Eq. (3.11) as a function of  $k_F$ . We choose our free parameters to fit  $E/A - M_N(0) \equiv B = -15.75$  MeV at the minimum. The parameters are summarized in Table 3.1. We use the value  $g_s = 1.27$  (corresponding to  $\sigma_N = 41.4$  MeV),

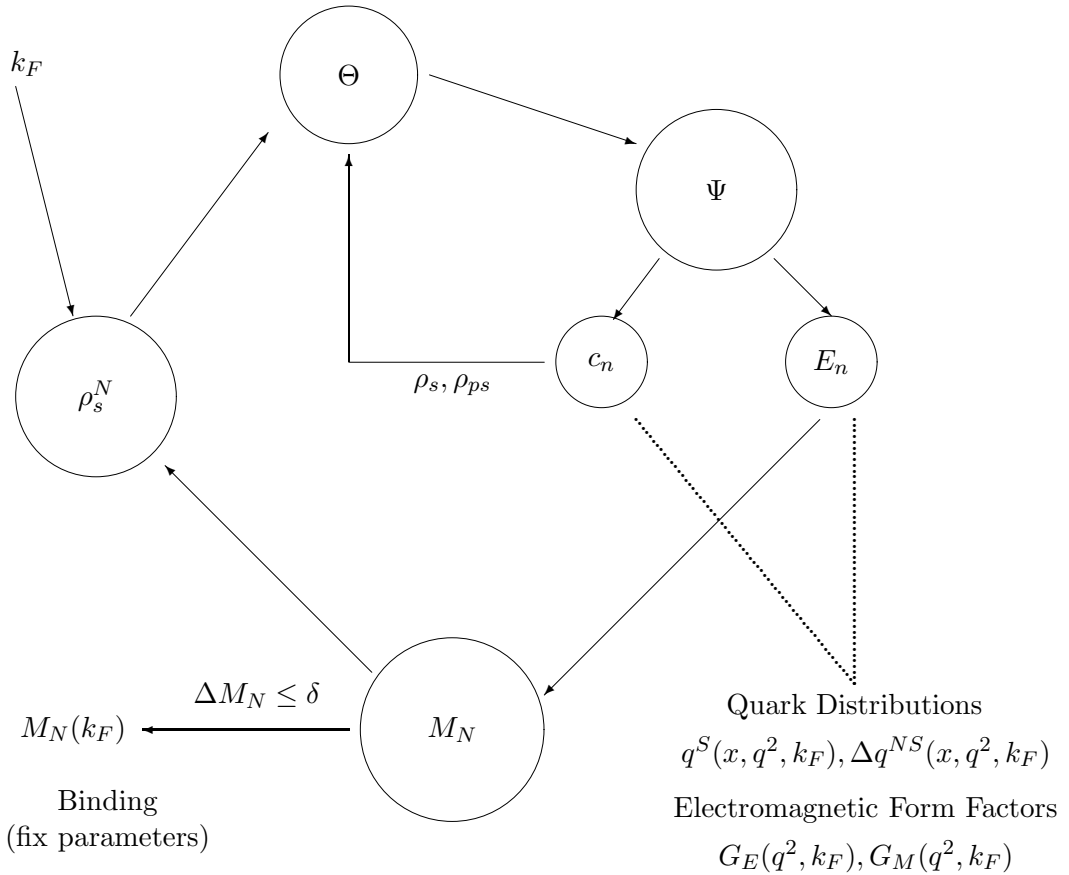


Figure 3.2: Diagram of the two-tier self-consistent loop. One inputs a value for  $k_F$  and a guess for the profile function.  $\Theta$  represents the field equation for the profile.  $\Psi$  represents the Dirac equation solved in the finite basis, which takes the profile function as an input, and outputs a set of energy eigenvalues  $E_n$  and wave functions. The  $E_n$  are then used to calculate a the nucleon mass  $M_N$  which is then used to calculate a new nucleon scalar density.

Table 3.1: Model parameters to fit binding energy  $B = -15.75$  MeV, the location of the minima, compressibility, and the resulting density of nuclear matter in units of  $\rho_0 = 0.178 \text{ fm}^{-3}$  consistent with the experimental value of  $0.167 \pm 0.018 \text{ fm}^{-3}$  [20].

$g_s$ [MeV]	$g_v^2/4\pi$ [fm $^{-1}$ ]	$k_F$ [fm $^{-1}$ ]	$K$ [MeV]	$\rho/\rho_0$
0.89	7.22	1.81	291.7	2.26
1.10	8.96	1.51	312.5	1.31
1.27	10.55	1.38	348.5	1.00

and vector coupling  $g_v^2/4\pi = 10.55$ , which gives a Fermi momentum of  $k_F = 1.38 \text{ fm}^{-1}$  in nuclear matter consistent with the known value  $k_F = 1.35 \pm 0.05 \text{ fm}^{-1}$  [20]. This value of  $g_s$  is used for the calculation of all of the parton distributions and electromagnetic form factors. We plot the binding energy per nucleon using Eq. (3.11) in Fig. 3.3. The compressibility is  $K = 348.5 \text{ MeV}$  which is above the experimental value  $K = 210 \pm 30 \text{ MeV}$ , but well below the Walecka model [108] value of 560 MeV. We have performed the self-consistent calculation to obtain the profile functions for zero density,  $0.5\rho_0$ ,  $1.0\rho_0$  and  $1.5\rho_0$  in Fig. 3.4 (where  $\rho_0 = 0.178 \text{ fm}^{-3}$  is nuclear density, consistent with the experimental value of  $0.167 \pm 0.018 \text{ fm}^{-3}$  [20]).

We need to address the valence-only approximation in Eq. (3.5) to the self-consistent profile solution. Specifically, we are making the approximation that when the change in the valence energy level  $\Delta E^v$  is small, so is  $\Delta M_N$ . We are also hypothesizing that the negative energy level contributions to the scalar density are approximately constant in space, and that the spatially varying part of the scalar density is well approximated by the valence level. It is very important to note that these approximations are only used in determining the self-consistent profile, not in the wave functions used as input into the quark distributions or electromagnetic form factors. We can see the difference from a fully self-consistent calculation of the profile function for a free nucleon in Fig. 3.5. The resulting profiles are virtually identical.

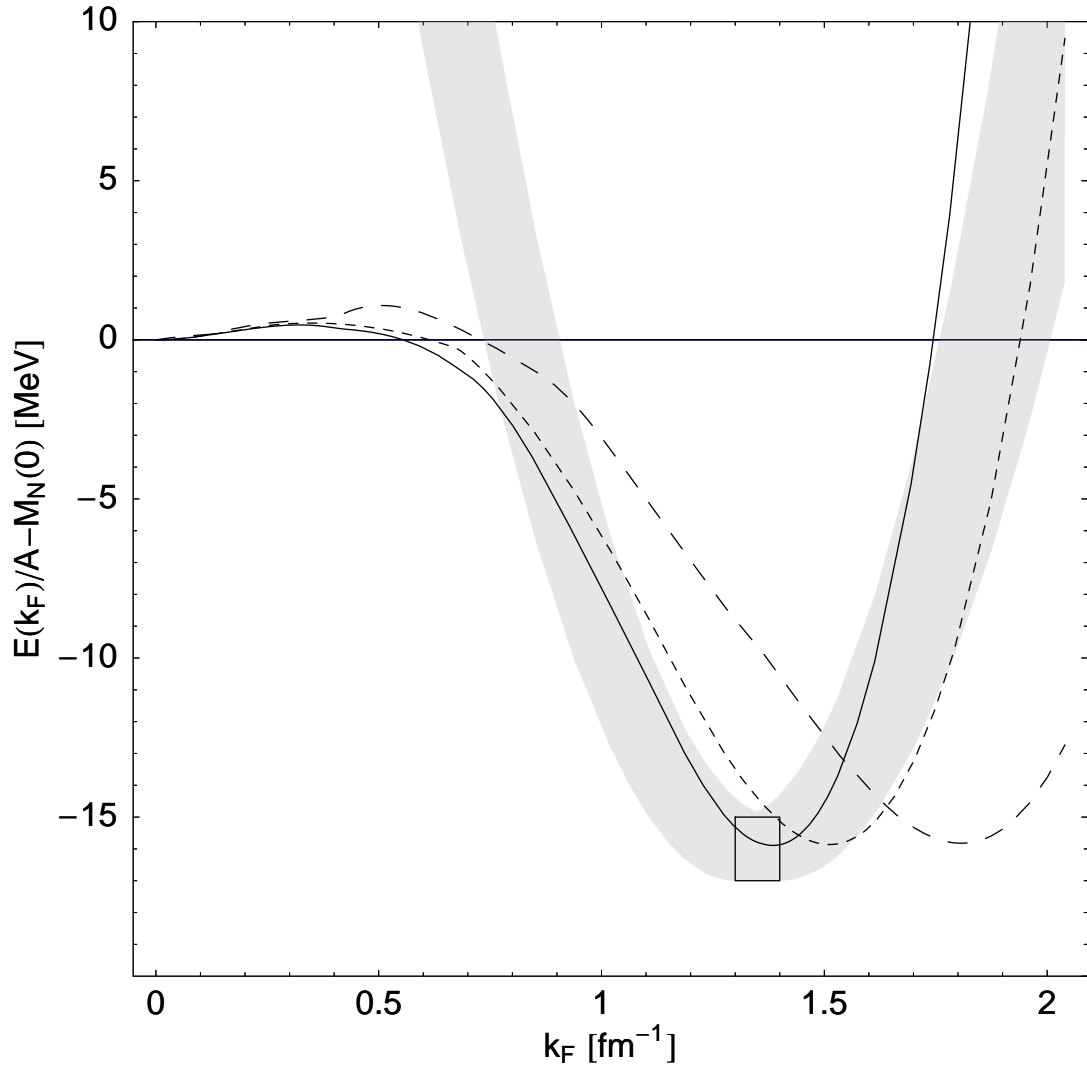


Figure 3.3: Binding energy per nucleon  $B = E/A - M_N$  as a function of Fermi momentum fit to  $B = -15.75$  MeV at the minimum for  $g_s = 0.89$  (long dashed),  $1.10$  (short dashed) and  $1.27$  (solid). The box and shaded region are the experimental uncertainty [20] in the binding energy, density and compressibility of nuclear matter.

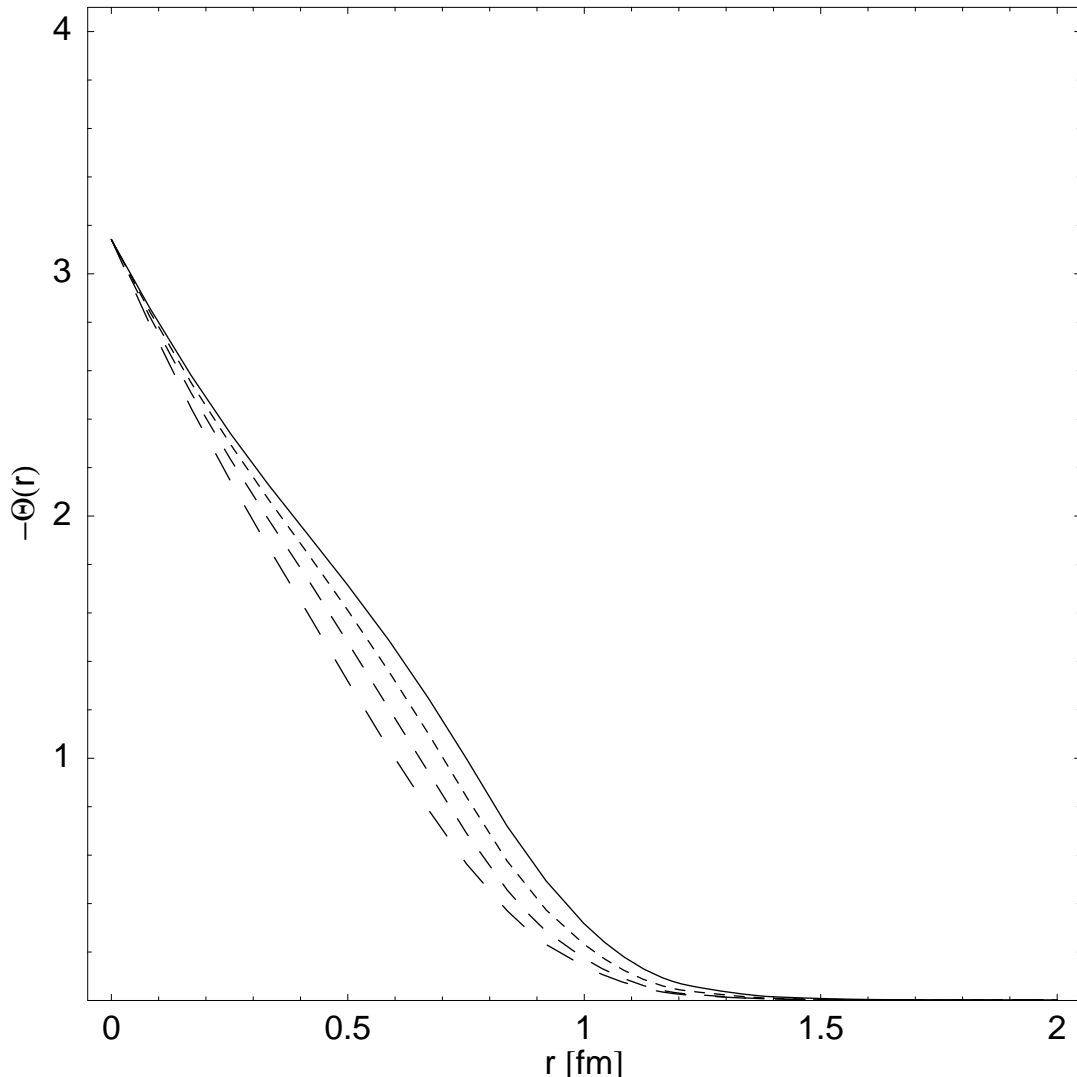


Figure 3.4: Profile functions in nuclear matter. The solid line is the profile function for  $1.5\rho_0$ ; the curves with progressively longer dashes correspond to  $1.0\rho_0$ ,  $0.5\rho_0$  and zero density respectively.

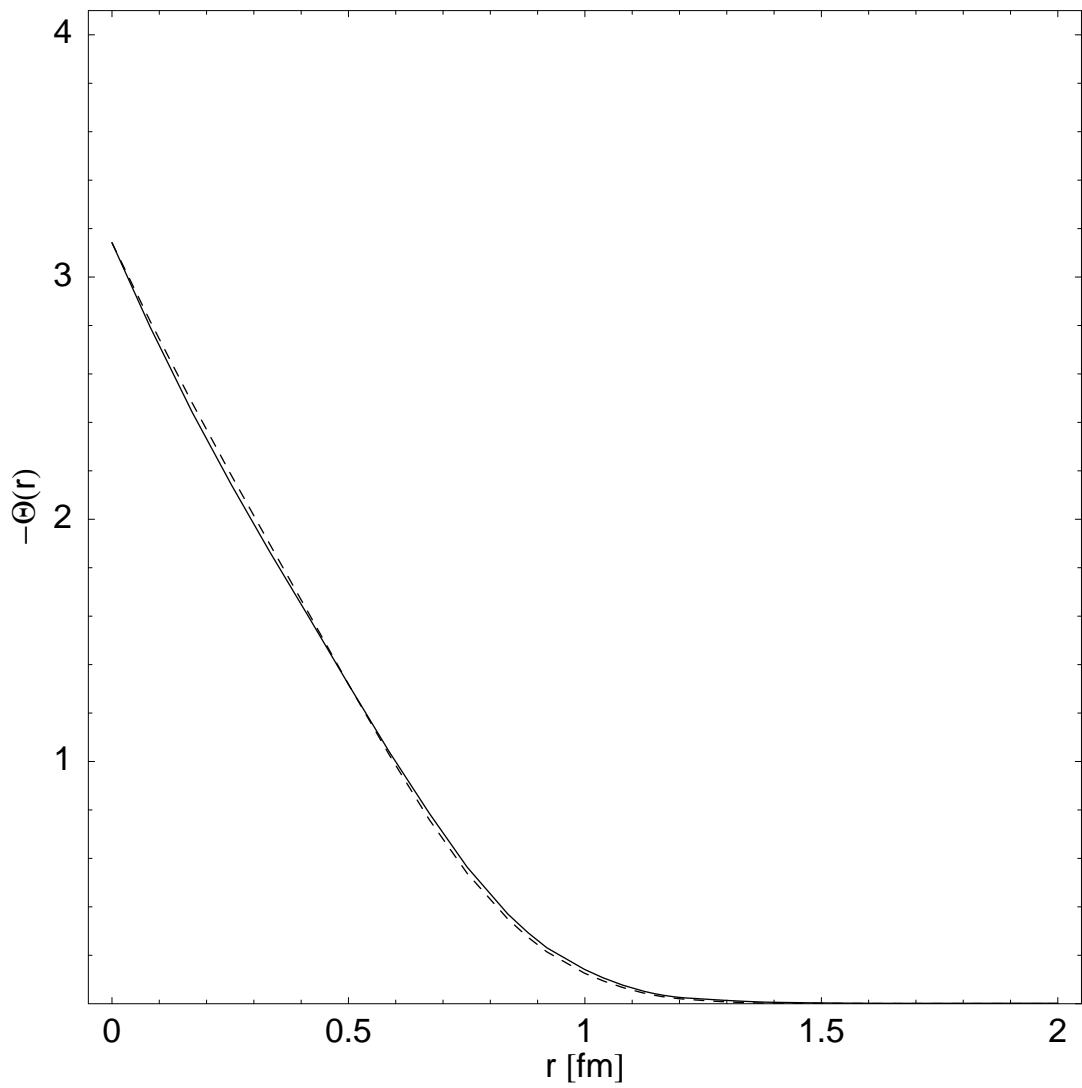


Figure 3.5: Profile functions for the free nucleon using the valence approximation of Eq. (3.5) (solid) and a fully self-consistent treatment (dashes).

While the vacuum value of the condensate does not vary with the Fermi momentum by definition, the effective condensate Eq. (3.6) falls  $\sim 30\%$  at nuclear density,  $q.v.$  Eq. (3.3). This is consistent with the model independent result [31] that predicts a value 25-50% below the vacuum value. The nucleon mean square radius is plotted as a function of the Fermi momentum in Fig. 3.6. The influence of the nuclear medium on the nucleon causes the root mean square radius of the baryon density to increase by 3.1% at  $k_F = 1.38 \text{ fm}^{-1}$ . This swelling is consistent with a  $< 6\%$  increase ( $\langle r^2 \rangle_A / \langle r^2 \rangle_0 < 1.12$  in Fig. 3.6) as constrained by quasi-elastic inclusive electron-nucleus scattering data [75].

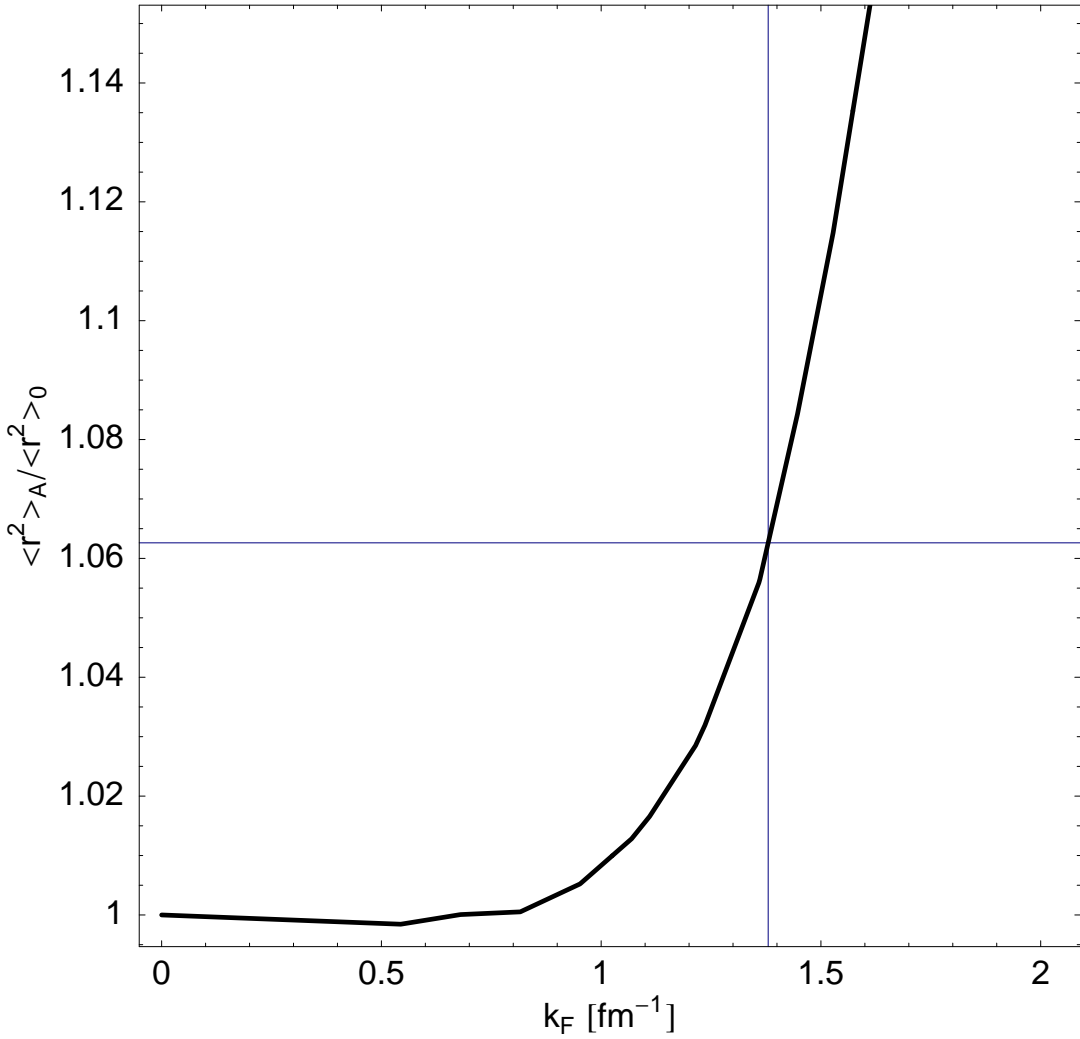


Figure 3.6: The nucleon mean square radius as a function of Fermi momentum. The 3.1% increase at  $k_F = 1.38 \text{ fm}^{-1}$  is indicated by the horizontal and vertical lines. Experiments [75, 102] limit nucleon root mean square radius swelling to less than 6%, or 1.12 on the vertical axis.

## Chapter 4

### QUARK DISTRIBUTIONS

One way to probe intermediate length scales and non-perturbative physics is to examine the short distance structure of a large object. The prime example is the European Muon Collaboration (EMC) effect [7] where the short distance ( $\sim 5$  GeV, or  $\sim 10^{-2}$  fm) structure of nuclei seen in deep inelastic lepton-nucleus scattering differs from that of a collection of free nucleons. This measurement showed that bound nucleons are different than free ones, and implied that the medium modifications could be significant for any nuclear observable [50].

Our primary concern is the depletion of the nuclear structure function  $F_2^A(x)$  in the valence quark regime  $0.3 \lesssim x \lesssim 0.7$ . While the general interpretation is that a valence quark in a bound nucleon has less momentum than in a free one, corresponding to some increased length scale, the specific mechanism for this has eluded a universally accepted explanation for 20 years [50, 83, 6, 93]. A popular explanation is the so-called ‘binding’ effect which originates from a possible mechanism in which mesons binding the nucleus carry momentum. An important consequence is that the mesonic presence would enhance the anti-quark content of the nucleus [12, 44]. Such an effect has not been seen in Drell-Yan experiments [2] in which a quark in a proton beam annihilates with an antiquark in a nuclear target producing a muon pair. Furthermore, relativistic treatments, including the light-cone approach needed to obtain the nucleon structure function, of the binding effect with structureless hadrons fail [79, 98, 15, 47], suggesting that modifications of the internal quark structure of the nucleon are required to explain the deep inelastic scattering data.

Any description of the EMC effect must be consistent with the constraints set by both deep inelastic scattering and Drell-Yan data. Thus a successful model must include antiquarks as well as quarks, and show how the medium modifies both the valence and sea quark distributions. Our purpose is to provide a mechanism for that modification within the

Chiral Quark-Soliton ( $\chi$ QS) model [68, 16, 39, 26]. This phenomenological model has many desirable qualities: the ability to describe a wide class of hadron observables with surprising accuracy, the inclusion of antiquarks, positivity of Generalized Parton Distributions, and a basis in QCD [39]. Here we show how the model describes the EMC effect, and satisfies the bounds on nuclear antiquark enhancement provided by Drell-Yan experiments.

Polarized lepton-nucleus scattering experiments are another important tool in hadronic physics. For example, in order to study the spin structure function of the neutron, one must use nuclear targets. It is already well known that there are significant differences between free and bound nucleons in the unpolarized case (the EMC effect [7]). It is reasonable to assume that nuclear effects could appear in polarized quark distributions. Our purpose here is to calculate the analogous modification to the nucleon spin structure function  $g_1^{(p,n)}(x, Q^2)$ : a ‘polarized EMC effect’.

#### 4.1 Light-cone Correlation Function and Sum Rules

If we insert a complete set of states into the light-cone correlation function, we obtain

$$q(x) = k^+ \int \frac{dz^-}{2\pi} e^{ixk^+z^-} \langle k | \bar{\psi}(0) \gamma^+ \psi(z^-) | k \rangle \quad (4.1)$$

$$= N_C k^+ \sum_n \int \frac{dz^-}{2\pi} e^{ixk^+z^-} \langle k | p, n \rangle \gamma^0 \gamma^+ e^{-ip_n^+ z^-} \langle p, n | k \rangle. \quad (4.2)$$

Evaluating Eq. (4.2) in the rest frame, with  $k^+ = k^- = M_N[\Theta(r, k_F)]$  from Eq. (3.15), and writing the wave functions and plus and minus components explicitly, we obtain

$$q(x) = N_C M_N \sum_n \int \frac{dz^0}{2\pi} e^{ixM_N z^0} \psi_n^\dagger(p) (1 + \gamma^0 \gamma^3) e^{-i(E_n + p^3)z^0} \psi_n(p) \quad (4.3)$$

We can put this in a form that is ideal for evaluation in the finite KR basis

$$q(x) = N_C M_N \sum_n \langle n | (1 + \gamma^0 \gamma^3) \delta(E_n + p^3 - xM_N) | n \rangle \quad (4.4)$$

In order to address the baryon and momentum sum rules, we will follow Ref. [40]. It is convenient to put the light-cone correlator in the form of a functional trace using (in the rest frame)

$$\sum_n |n\rangle \langle n| e^{-iE_n z^0} = \int dE \delta(E - H) e^{-iEz^0}$$

where  $H$  is the Dirac Hamiltonian Eq. (3.12). With this substitution, we can write the moments of Eq. (4.3) as

$$\int dx x^{n-1} q(x) = N_C M_N^{1-n} \int dE \operatorname{Tr} [\delta(E - H)(E + p^3)^{n-1}(1 + \gamma^0 \gamma^3)] \quad (4.5)$$

For  $n = 1$ , we obtain the baryon sum rule

$$N_C \operatorname{Tr} [\theta(E^v - H) - \theta(-H^{(0)})] = N_C B$$

since the  $\theta$ -function operator simply counts the occupied levels in the nucleon, with the number of occupied levels in the vacuum subtracted, leaving only the quarks in the valence level. It should be noted here that the topological condition for the profile function guarantees that only one energy level comes out of the positive continuum, and hence that the winding number of the soliton field is not the baryon number; it is only a necessary, not sufficient, condition to obtain unit baryon number.

For  $n = 2$ , along with other terms that vanish by the hedgehog symmetry of the profile function, we obtain the momentum sum rule

$$\begin{aligned} N_C M_N^{-1} \operatorname{Tr} [\theta(E^v - H)H - \theta(-H^{(0)})H^{(0)}] &= N_C M_N^{-1} \left[ E^v + \sum_{E_n < 0} E_n - \sum_{E_n^{(0)} < 0} E_n^{(0)} \right] \\ &= M_N^{-1} M_N [\Theta(r, k_F)] \\ &= 1 \end{aligned} \quad (4.6)$$

The only details we have used are that we have a complete set of basis states, a single valence energy level, and that the sum of the energy eigenvalues of the Dirac Hamiltonian Eq. (3.12) yield the nucleon mass Eq. (3.15). Therefore, the calculation presented here is independent of the addition of a non-zero vector potential. It is important to note that both of these sum rules are automatically satisfied as long as one remains in the same basis consistently throughout the calculation, provided Eq. (4.1) holds.

## 4.2 Unpolarized Distributions

The isoscalar unpolarized distribution  $q(x) = u(x) + d(x)$  is the leading order term in  $N_C$ , with the isovector unpolarized quark distribution  $u(x) - d(x)$  smaller by a factor  $\sim 1/N_c$

and set to zero. The distributions are calculated using the KR basis at  $k_F = 0$  and  $k_F = 1.38 \text{ fm}^{-1}$  almost exactly as in Ref. [36] where the quark distribution is given by the matrix element Eq. (4.4) evaluated in the finite basis

$$q(x) = N_C M_N \sum_n \sum_{i,j} c_{ni}^* c_{nj} \frac{1}{2p_i} \theta(p_i - |E_n - xM_N|) \left[ \delta_{ij} - \frac{E_n - xM_N}{p_i^2} (\gamma^0 \mathbf{p} \cdot \boldsymbol{\gamma})_{ij} \right], \quad (4.7)$$

with the Pauli-Villars regulated sum taken over occupied states. The eigenvalues  $E_n$  are determined from diagonalizing the Hamiltonian, derived from the Lagrangian (2.10), in the KR basis. The vector meson exchange is not explicit in Eq. (4.7); it is implicit in the energy eigenvalues  $E_n$ . The antiquark distribution is given by  $\bar{q}(x) = -q(-x)$  where the sum is over unoccupied states [36]. We use the exact sea wave functions, and not the approximation used in Eq. (3.5). The use of a finite basis causes the distributions to be discontinuous. These distributions are smooth functions of  $x$  in the limit of infinite momentum cutoff and box size, but numerical calculations are made at finite values and leave some residual roughness. This is overcome in Ref. [36] by introducing a smoothing function. We deviate from their procedure, and do not smooth the results; instead we find the subsequent one-loop perturbative QCD evolution [57] to be sufficient. This can be seen in Fig. 4.1.

These distributions are used as input at the model scale of  $Q^2 = M_{PV}^2 \simeq 0.34 \text{ GeV}^2$  for evolution to  $Q^2 = 10 \text{ GeV}^2$  in the case of the quark singlet distribution  $q^S(x) = q(x) + \bar{q}(x) \propto F_2^N(x)/x$  at leading order in  $N_C$ . We define the generic ratio function to be

$$R_g(x, Q^2) = \frac{f \otimes g(x, Q^2, k_F)}{Ag(x, Q^2, k_F = 0)}, \quad (4.8)$$

$$f \otimes g(x/y, Q^2, k_F) = \int_x^A dy f(y) g(x/y, Q^2, k_F). \quad (4.9)$$

In the following, we take the general function  $g$  to be the structure function  $F_2^{(N)}$ , the antiquark distribution  $\bar{q}$ , or the spin structure function  $g_1^{(p,n)}$ . The nucleon momentum distribution  $f(y)$  following from a light-cone approach, for any mean field theory of nuclear matter (see Ref. [79] and Eq. (D.40) in Appendix D) is

$$f(y) = \frac{3}{4\Delta_F^3} \theta(1 + \Delta_F - y) \theta(y - 1 + \Delta_F) [\Delta_F^2 - (1 - y)^2], \quad (4.10)$$

where  $\Delta_F = k_F/\bar{M}_N$  and  $\bar{M}_N = M_N(0) - 15.75 \text{ MeV}$ . The distributions are evolved to  $Q^2 = 10 \text{ GeV}^2$  for use in the EMC ratio  $R_{F_2}(x)$  and the Drell-Yan ratio  $R_{\bar{q}}(x)$  Eq. (4.8).

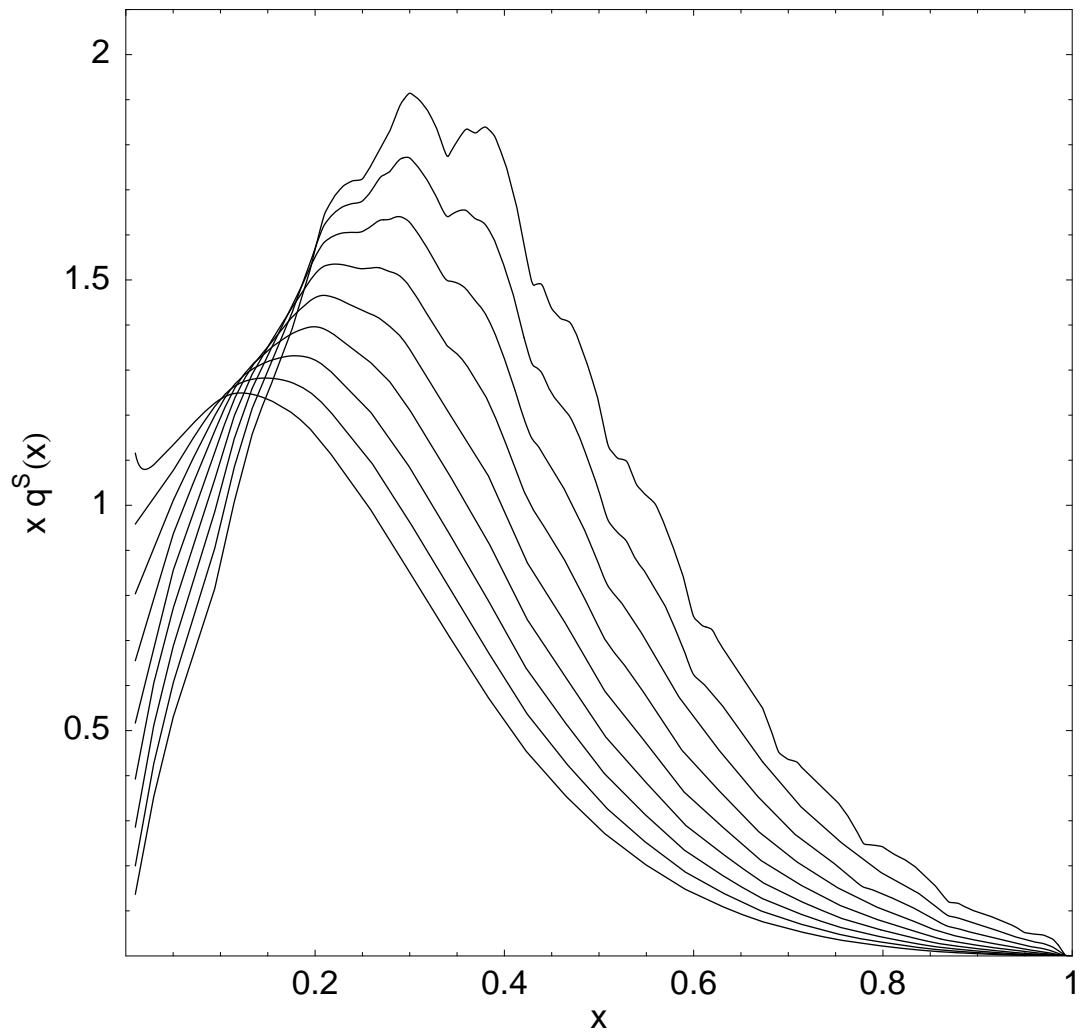


Figure 4.1: The smoothing effect of evolution on the quark singlet distribution. The curves are shown at scales  $\log M_{PV}^2$  (highest curve at  $x = 0.3$ ), and the DIS scale  $\log Q^2$ , with  $Q^2 = 10 \text{ GeV}^2$  (lowest curve at  $x = 0.3$ ).

The ratios are plotted in Figs. 4.2 and 4.3, respectively. While the data shown in Figs. 4.2 and 4.3 are for large, but finite, nuclei, our calculation reproduces the trend of both sets of data. It falls slightly below the SLAC-E139 data [52] due to the higher density of nuclear matter.

In Fig. 4.4 we show the quark singlet distribution for a free and bound nucleon at a scale  $Q^2 = 10 \text{ GeV}^2$ . There is a large depletion in the bound nucleon valence distribution, accounting for nearly all of the depletion in Fig. 4.4, since the antiquark contribution is virtually unchanged. If one uses only the valence contribution to calculate the EMC ratio (4.8), produces too large an effect. This large effect is comparable to that of the QMC model impulse approximation calculation or the Guichon model [90], both of which only include valence quarks. This valence effect is mitigated by a small enhancement in  $\bar{q}(x)$ , consistent with the Drell-Yan data, so that the singlet distribution has only a moderate depletion consistent with the EMC effect.

A simple picture in terms of the uncertainty principle is available. The influence of the nuclear medium on the nucleon causes the root mean square radius of the baryon density to increase by 3.1%. This corresponds to a decreased momentum, and a depletion of the bound structure function relative to the free one. This swelling is consistent with a  $< 6\%$  increase as constrained by quasi-elastic inclusive electron-nucleus scattering data [75], and the recent polarization transfer measurement [102].

We ignore the effects of shadowing, which occur when the virtual photon striking the nucleus fluctuates into a quark-antiquark pair over a distance  $\sim 1/2M_N x$  exceeding the inter-nucleon separation. This causes a depletion in the structure function for  $x \leq 0.1$  and is relatively well understood [50, 83, 6, 93] and so we do not reiterate those results. Additionally, we ignore contributions from quantum pion structure functions, which in this model propagate through constituent quark loops, and would modify the behavior at small  $x$ . These loops are suppressed by  $\mathcal{O}(1/N_C)$ , and are not treated at leading order.

The present model provides a intuitive, qualitative treatment that maintains consistency with all of the free nucleon properties calculated by others [39, 26]. It gives a reasonable description of nuclear saturation properties, reproduces the EMC effect, and satisfies the constraints on the nuclear sea obtained from Drell-Yan experiments with only two free

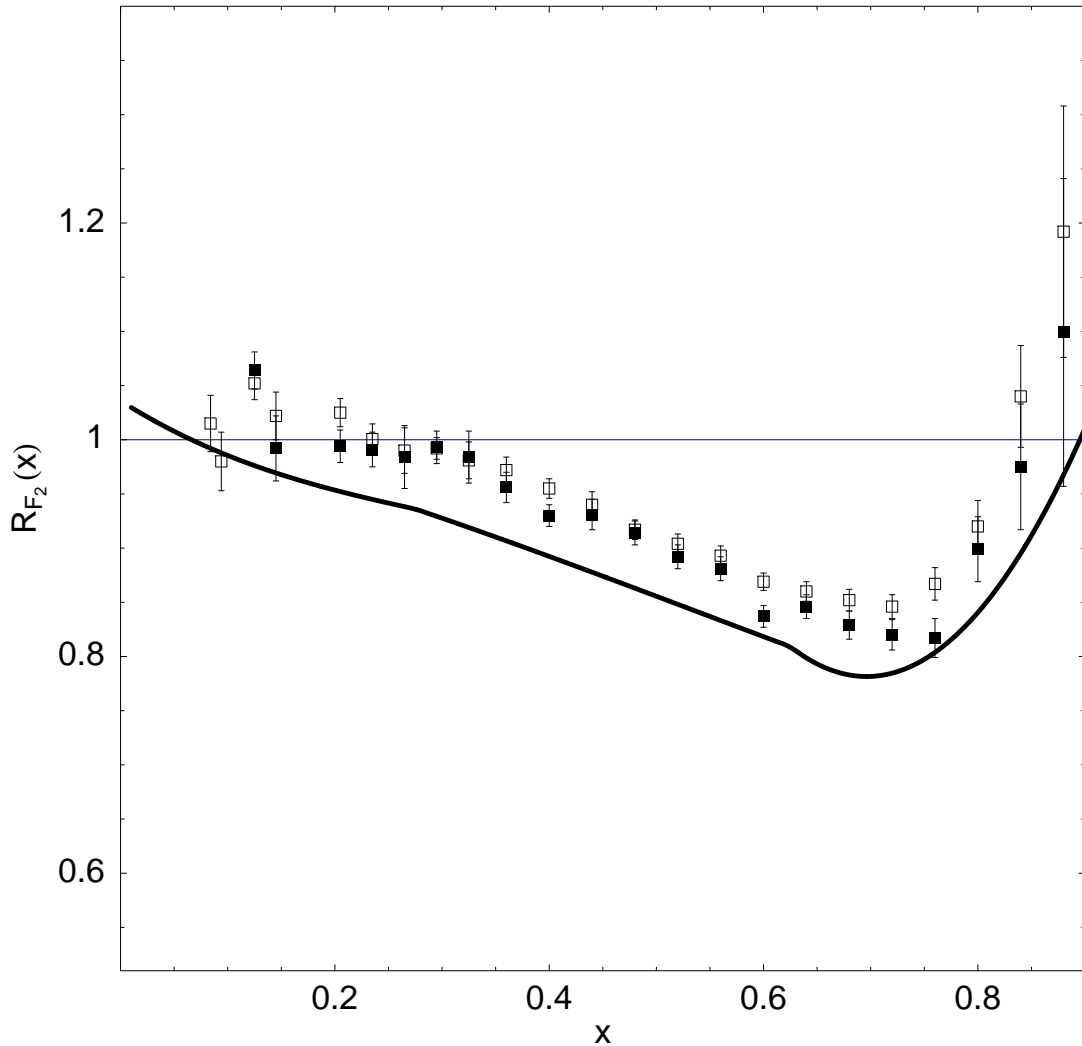


Figure 4.2: The EMC ratio at a scale  $Q^2 = 10$  GeV $^2$  for nuclear matter. The data are for Iron (empty boxes) and Gold (filled boxes) from SLAC-E139 [52].

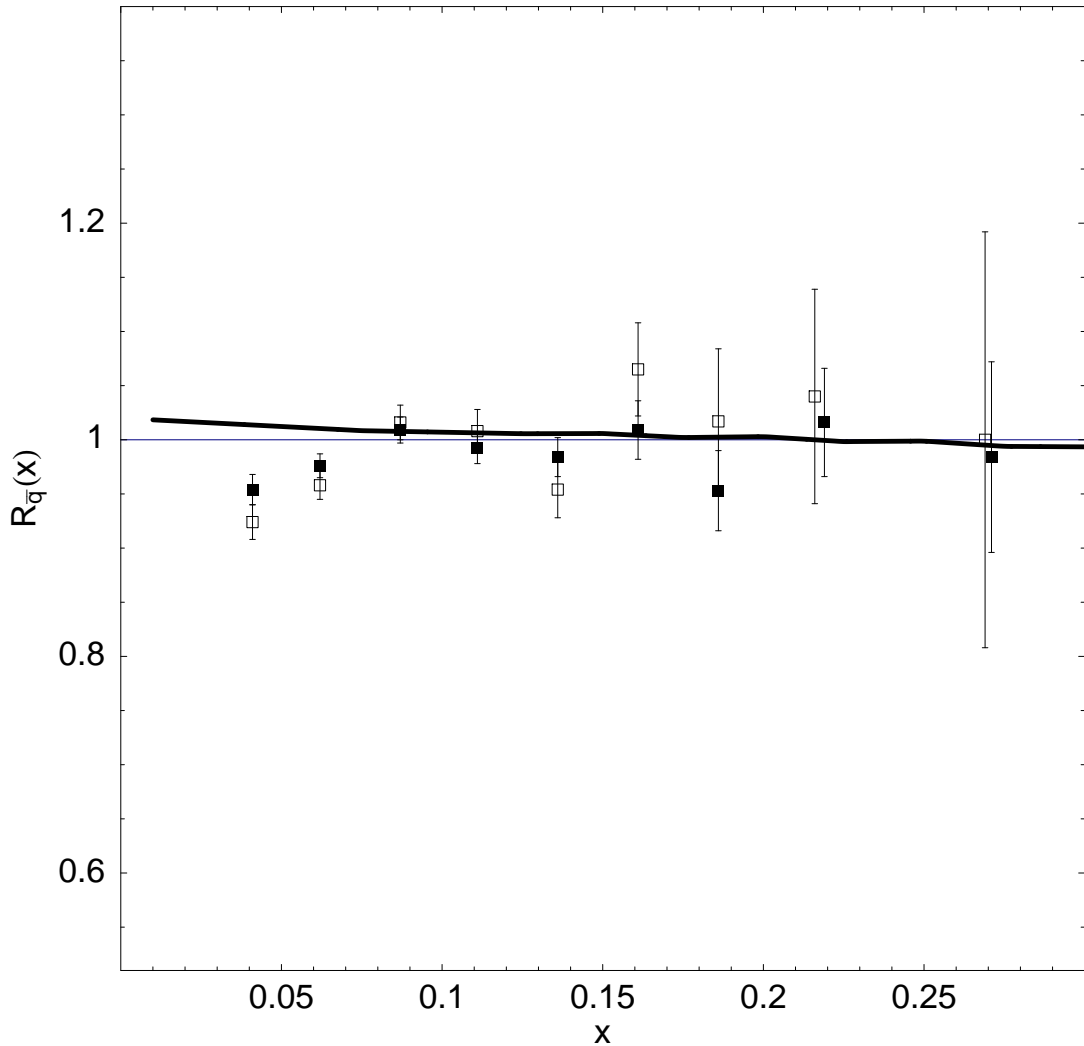


Figure 4.3: The Drell-Yan ratio at a scale  $Q^2 = 10 \text{ GeV}^2$  for nuclear matter. The data are for Iron (empty boxes) and Tungsten (filled boxes) from FNAL-E772 [2].

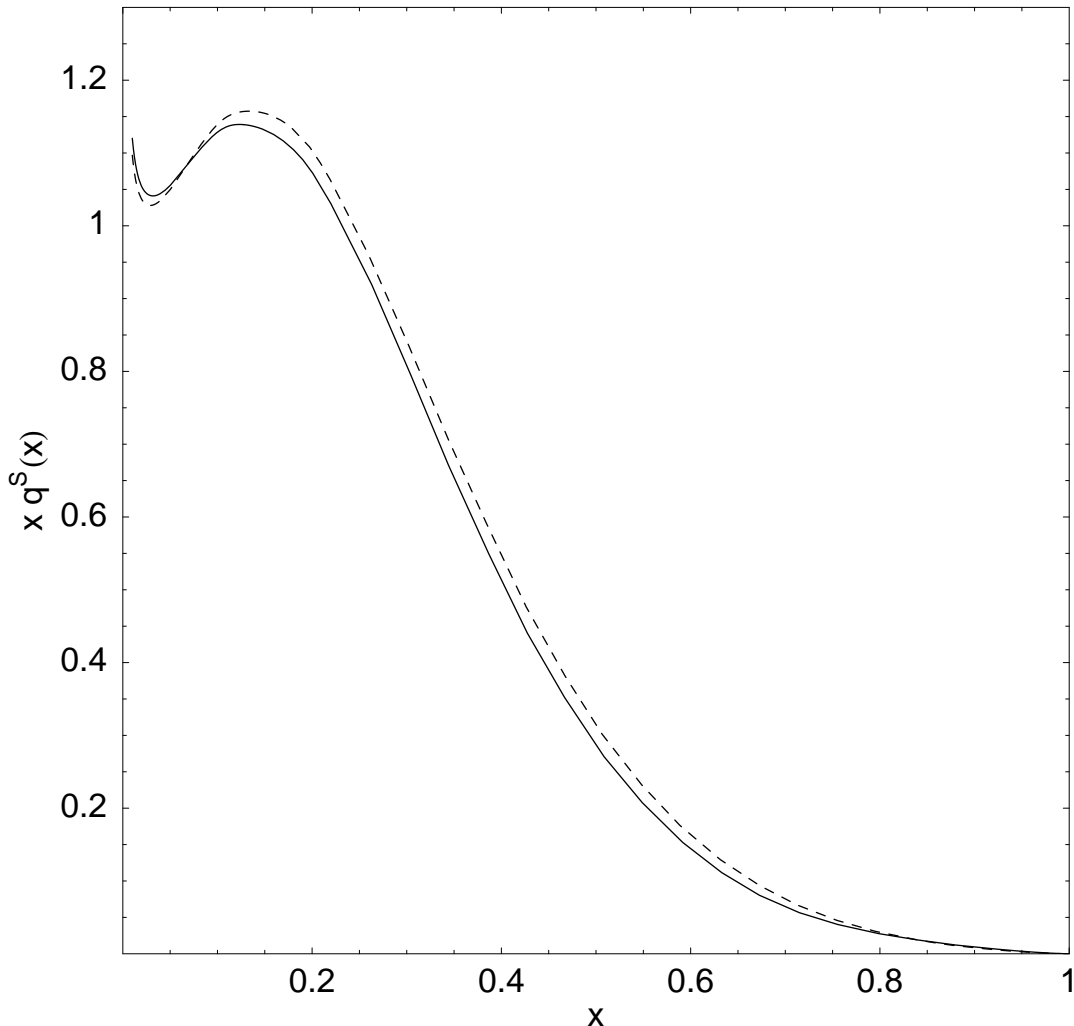


Figure 4.4: The distribution  $xq^S(x)$  in a free (dashed) and bound (solid) nucleon at a scale  $Q^2 = 10 \text{ GeV}^2$ .

parameters:  $g_s$  and  $g_v$ .

The central mechanism to explain the EMC effect is that the nuclear medium provides an attractive scalar interaction that modifies the nucleon wave function. This is also the dominant mechanism in the QMC model approach to the EMC effect [90] and also similar to the quark delocalization approach [9]. The improvements given here are the explicit computation of the effects of the medium on the antiquark distributions so that consistency with the Drell-Yan data could be verified, and the reduction of the number of input parameters and model assumptions. Our extension of the Chiral Quark-Soliton model to nuclear matter provides a new, consistent way to calculate possible medium modifications of a variety of observables that could be measured in experiments.

### 4.3 Polarized Quark Distribution Function

The first discussion of nuclear effects in the polarized quark distributions is in Ref. [30] in the context of dynamical rescaling. A more recent calculation is in Ref. [28]; it predicts dramatic effects for the bound nucleon spin structure function. We have previously shown how the model describes nuclear saturation properties, reproduces the EMC effect, and satisfies the bounds on unpolarized nuclear antiquark enhancement provided by Drell-Yan experiments [99]. Therefore, we expect the  $\chi$ QS model to produce a reasonable result for the polarized distributions.

The polarized quark distribution for flavor  $i$  is defined by the difference between the quark distributions with spin parallel ( $\uparrow$ ) and antiparallel ( $\downarrow$ ) to the nucleon

$$\Delta q_i(x, Q^2) = q_i^\uparrow(x, Q^2) - q_i^\downarrow(x, Q^2). \quad (4.11)$$

The polarized antiquark distribution is defined analogously using  $\bar{q}_i^\uparrow$ , and  $\bar{q}_i^\downarrow$ . The isovector polarized distribution  $\Delta q^{(T=1)}(x) = \Delta u(x) - \Delta d(x)$  is the leading order term in  $N_C$ , with the isoscalar polarized quark distribution  $\Delta q^{(T=0)}(x) = \Delta u(x) + \Delta d(x)$  smaller by a factor  $\sim 1/N_C$  and set to zero. We will therefore suppress the isospin superscript in the following. The distributions are calculated using the KR basis at  $k_F = 0$  and  $k_F = 1.38 \text{ fm}^{-1}$  (see Refs. [99, 100]) almost exactly as in Ref. [36] where the quark distribution is given by the

matrix element

$$\begin{aligned} \Delta q(x) = & -\frac{1}{3}(2T_3)N_C M_N \sum_n \sum_{i,j} c_{ni}^* c_{nj} \frac{1}{2p_i} \theta(p_i - |E_n - xM_N|) \times \\ & \left[ \frac{E_n - xM_N}{p_i^2} (\gamma_5 \mathbf{p} \cdot \boldsymbol{\tau})_{ij} + \right. \\ & \left( -\frac{1}{2p_i} + \frac{3}{2} \frac{(E_n - xM_N)^2}{p_i^4} \right) \sum_k (\gamma^0 \mathbf{p} \cdot \boldsymbol{\gamma})_{ik} (\gamma_5 \mathbf{p} \cdot \boldsymbol{\tau})_{kj} + \\ & \left. \left( \frac{1}{2} - \frac{1}{2} \frac{(E_n - xM_N)^2}{p_i^2} \right) (\gamma^0 \boldsymbol{\tau} \cdot \boldsymbol{\gamma})_{ij} \right], \end{aligned} \quad (4.12)$$

with the Pauli-Villars regulated sum taken over occupied states. The eigenvalues  $E_n$  are determined from diagonalizing the Hamiltonian, derived from the Lagrangian (2.10), in the KR basis.

The antiquark distribution is given by  $\Delta \bar{q}(x) = \Delta q(-x)$  where the sum is over unoccupied states. The use of a finite basis causes the distributions to be discontinuous. These distributions are smooth functions of  $x$  in the limit of infinite momentum cutoff and box size, but numerical calculations are made at finite values and leave some residual roughness. This is overcome in Ref. [36] by introducing a smoothing function. We deviate from their procedure, and do not smooth the results; instead we find that performing the one-loop perturbative QCD evolution [57] provides sufficient, but not complete, smoothing. Some residual fluctuations due to the finite basis remain visible in our results, and the size of these fluctuations serve as a guide to the size of the error introduced by the method.

These distributions are used as input at the model scale of  $Q^2 = M_{PV}^2 \simeq 0.34 \text{ GeV}^2$  for evolution to  $Q^2 = 10 \text{ GeV}^2$ . The polarized structure function to leading order in  $N_C$  is given by

$$g_1^{(p,n)} = \frac{1}{2} \sum_i e_i^2 (\Delta q_i + \Delta \bar{q}_i) \quad (4.13)$$

$$g_1^{(p,n)} = \pm \frac{5}{18} \Delta q^{NS} + \mathcal{O}(N_C^0) \quad (4.14)$$

$$\Delta q^{NS} = \frac{3}{5} (\Delta u - \Delta d + \Delta \bar{u} - \Delta \bar{d}) + \mathcal{O}(N_C^0) \quad (4.15)$$

The nucleon momentum distribution is assumed to be the same as the unpolarized case, Eq. (4.10).

This is justified since the Hugenholtz-van Hove theorem follows from the pressure vanishing for a stable nucleus (see Appendix D), which would remain valid for a polarized system. Therefore, we would expect to still have a distribution sharply peaked around  $y \simeq 1$ . The details of the functional form of  $f(y)$  have little effect on the ratio beyond the peak location. We are already ignoring target polarization, which has the same effect as the leading order correction (change in the normalization) to the momentum distribution, with the sum on the spin-dependent distributions yielding the unpolarized distributions. Also, the spin-orbit force tends to average out in nuclear matter, leading to the same distribution for all nucleons. The nuclear matter momentum distribution we use is fairly close to those calculated for Lithium isotopes [92].

We show the ratio Eq. (4.8) in Fig. 4.5 using a ‘valence’-like distribution, as well as for the full distribution. The latter includes all medium modifications, while the former distribution uses the medium modified energy level eigenstate, but the same free nucleon sea quark distribution for both the free and bound nucleon. This was done in order to compare our results with the model in Ref. [28], which only has valence quarks at the model scale. The single energy level actually has a contribution to the polarized antiquark distribution, so it alone cannot be considered a true valence spin structure function. However, this contribution is small, so we effectively reproduce the result of a valence quark model, especially in the region  $x \gtrsim 0.3$ .

In Fig. 4.5, one can see that there is a large depletion in the polarized ‘valence’ quark distribution . This produces a large depletion in the isovector axial coupling  $g_A^{(T=1)}$  of 17.8%. This large effect is comparable to that of the calculation in Ref. [28] which only includes valence quarks at the model scale. This valence effect is mitigated by a large enhancement in the sea quark contribution, so that the full polarized distribution has only a moderate depletion in the region  $0.3 \lesssim x \lesssim 0.7$  of the same size as the EMC effect in unpolarized nuclear structure functions. There is a large enhancement for  $x \lesssim 0.3$  due to the sea quarks. This large enhancement is very different from the small effect calculated in the unpolarized case [99], and seen in unpolarized Drell-Yan experiments [2]. This would suggest that one might see a significant enhancement in a polarized Drell-Yan experiment, even after including shadowing corrections (which we address later).

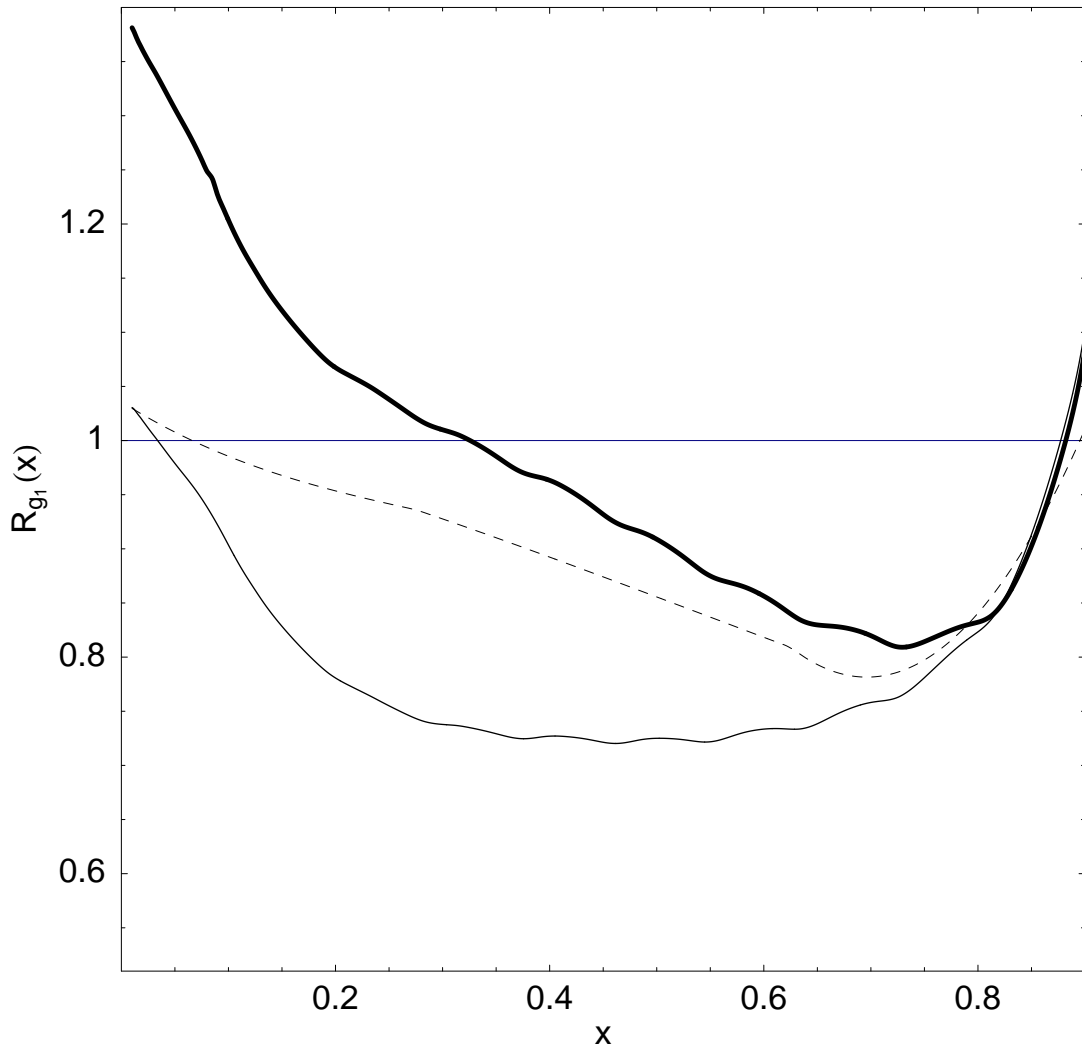


Figure 4.5: The ratio Eq. (4.8) at scale  $Q^2 = 10 \text{ GeV}^2$  for nuclear matter. The heavy line is the full calculation for nuclear matter. The light line is the effect calculated using only medium modifications to the ‘valence’ energy level as described in the text.

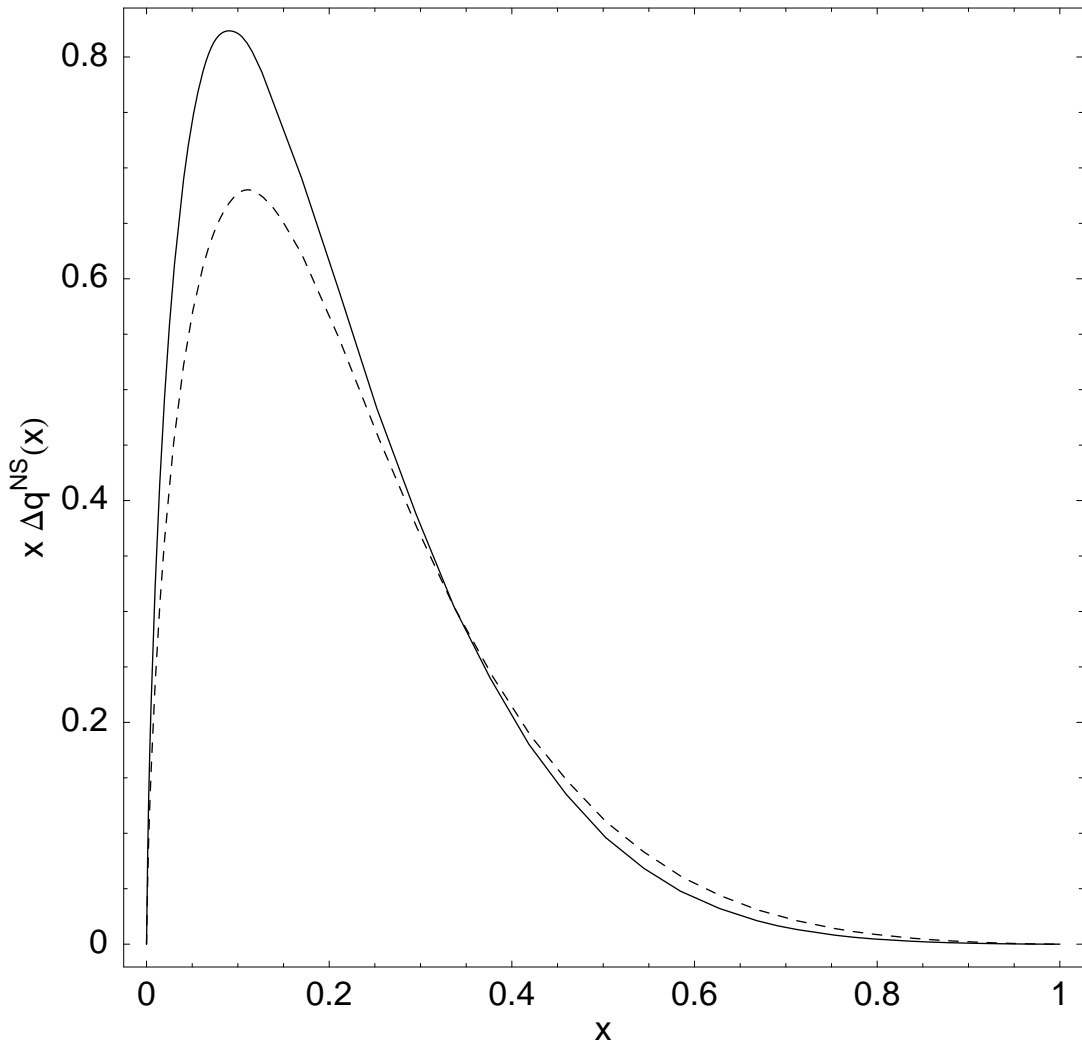


Figure 4.6: The distribution  $\Delta q^{NS}(x)$  in a free (dashed) and bound (solid) nucleon at a scale  $Q = 10 \text{ GeV}^2$ .

The larger sensitivity to the lower components of the wave functions, and the smaller size of the relevant distribution  $\Delta q(x)$  are the primary sources for the greater sea quark enhancement in the polarized case than in the unpolarized case. This model gives a smaller value for the isovector axial coupling  $g_A^{(T=1)} = 1.11$  than experiment. This is to be expected at leading order in  $N_C$  as there are important corrections due to rotational modes of the soliton. These corrections should be relatively minor when considering the ratio Eq. (4.8).

The axial coupling  $g_A^{(T=1)}$  is enhanced by 9.8% in the nuclear medium. This is in accord with an earlier finding of a  $\sim 25\%$  enhancement for  $g_A$  in a different soliton model by Birse [14]. There, the effect is also seen as a competition between enhancement and depletion.

In order to address the medium modification of the Bjorken sum rule [18, 19]

$$\lim_{Q^2 \rightarrow \infty} \int_0^1 dx g_1^{(p)}(x, Q^2) - g_1^{(n)}(x, Q^2) = \frac{g_A}{6} \quad (4.16)$$

as an integral of the experimentally observed nuclear distribution, one must account for the effects of shadowing. This occurs when the virtual photon striking the nucleus fluctuates into a quark-antiquark pair over a distance  $\sim 1/2M_N x$  exceeding the inter-nucleon separation. This causes a depletion in the structure function for  $x \lesssim 0.1$  and is relatively well understood [83, 6, 93]. Shadowing in the polarized case is expected to be larger than in the unpolarized case by roughly a factor of 2 simply from the combinatorics of multiple scattering (see *e.g.* Ref. [56]).

The enhancement at  $x \sim 0.1 - 0.2$  in Fig. 4.5 is comparable to that seen by Guzey and Strikman [56]; they assume that the combined effects of shadowing, enhancement, and target polarization lead to the empirical value of the nuclear Bjorken sum rule for  ${}^3\text{He}$  and  ${}^7\text{Li}$ . Shadowing effects become large for  $x \lesssim 0.05$ , but we ignore them as well as target polarization; such precision is not necessary for our relatively qualitative analysis. One needs  $\sim 10$  times the shadowing observed in the unpolarized case for Lead in order to counter the enhancement at  $x \sim 0.1 - 0.2$ , and give the same value for the Bjorken sum rule (4.16) in matter and free space. This assumes that shadowing is the only effect neglected at small  $x$  in our calculation of the unpolarized quark distribution [99].

We also present, in Fig. 4.7, the results for the spin asymmetry

$$A_1^{(p)}(x, Q^2) = \frac{\sum_i e_i^2 [\Delta q_i(x, Q^2) + \Delta \bar{q}_i(x, Q^2)]}{\sum_i e_i^2 [q_i(x, Q^2) + \bar{q}_i(x, Q^2)]}. \quad (4.17)$$

The nuclear asymmetry  $A_1^{(A)}$  is defined by replacing the polarized and unpolarized quark distributions, represented generically as  $q$ , with  $f \otimes q$  in Eq. (4.9). We find that for the free case, the calculation falls slightly below the data due to the smaller value of  $g_A$  in the large  $N_C$  limit, and that the size of the medium modification is of the same order as the experimental error for the free proton [5, 1].

The central mechanism to explain the EMC effect is that the nuclear medium provides an attractive scalar interaction that modifies the nucleon wave function. We see this again in the polarized case. This is also the dominant mechanism in the Nambu-Jona-Lasinio (NJL) type quark-diquark model of Cloet *et al* [28], and the soliton model of Birse [14].

It is worth noting that the model of Ref. [28] uses proper time infrared and ultraviolet cutoffs. These cutoffs are known [36] in the  $\chi$ QS model to ruin the equivalence of sums using occupied and unoccupied states, producing unphysical behavior in the antiquark distributions. This lack of equivalence can be traced to a violation of causality, therefore the NJL model of Ref. [28], like the MIT bag model used in the QMC model, probably could not be used to calculate medium effects on sea quarks.

The present model provides a intuitive, qualitative treatment that maintains consistency with all of the free nucleon properties calculated by others [39, 26]. It provides reasonable description of nuclear saturation properties, reproduces the EMC effect, and satisfies the constraints on the nuclear sea obtained from Drell-Yan experiments with only two parameters for the nuclear physics ( $g_s$  and  $g_v$ ) fixed by the binding energy and density of nuclear matter. Therefore, we expect the results presented here to manifest themselves in future experiments with polarized nuclei.

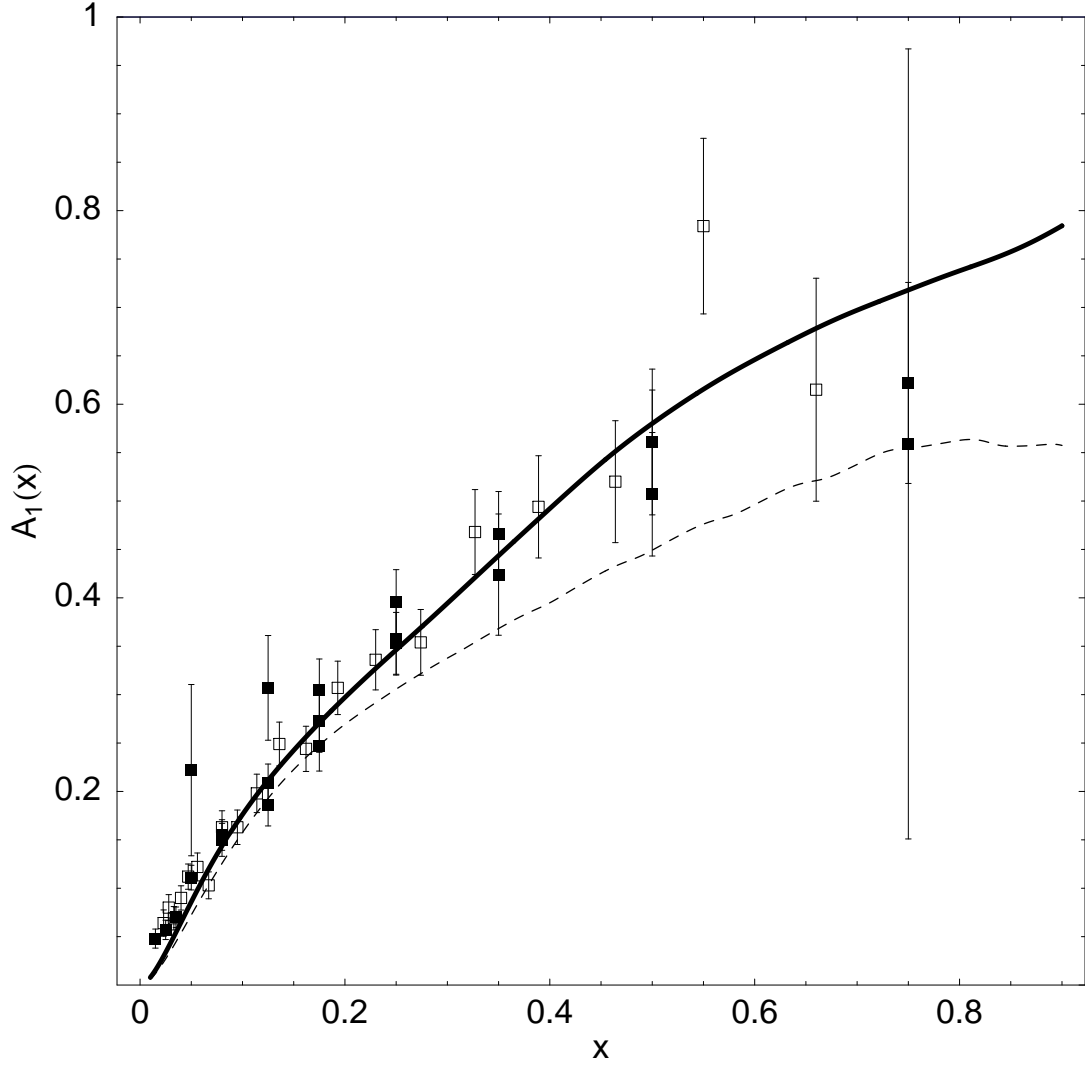


Figure 4.7: The asymmetry  $A_1^{(p)}$  Eq. (4.17) at scale  $Q^2 = 10 \text{ GeV}^2$ . The heavy line is for nuclear matter. The dashed line is for the free proton. The data are from SLAC [5] (filled) for  $Q^2 \sim 1 - 40 \text{ GeV}^2$  and HERMES [1] (empty) for  $Q^2 \sim 1 - 20 \text{ GeV}^2$ . The free curve falls slightly below the data due to the lower value of  $g_A$  calculated in the large  $N_C$  limit.

## Chapter 5

### ELECTROMAGNETIC FORM FACTORS

Recent polarization transfer experiments at TJNAF [102] observed a difference in the electromagnetic form factors of a proton bound in a Helium nucleus compared to a free one. The form factors encode the structure information of the proton observed in elastic scattering. There is extensive work on the medium modifications of electromagnetic properties of the nucleon in the literature (for example, see Refs. [87, 46, 110, 73] ). This includes effective Lagrangians as well as models that include the quark substructure of hadrons. While in principle these effects could be couched in terms of effective field theory operators, it is our thesis that such results may be more transparent, physically intuitive or straightforward to calculate when viewed as a change in the internal structure of the hadrons.

We will use the  $\chi$ QS model to calculate the electromagnetic form factors. The overall procedure is similar to the Quark-Meson Coupling model (QMC) [73], which uses the MIT bag model for the nucleon. The bag model does not include sea quarks. It is a confining model, whereas the  $\chi$ QS model is not. Additionally, the QMC model calculation, when coupled with a Relativistic Distorted Wave Impulse Approximation (RDWIA) calculation [106] or a Relativistic Multiple-Scattering Glauber Approximation (RMSGA) calculation [89, 71], improves the agreement between theory and the TJNAF data [102]. With our study, we hope to reinforce the interpretation of the medium effect in terms of quark degrees of freedom, as well as provide an alternate model when the accuracy of the data is improved.

The procedure is much the same as that in Chapter 4 for the quark distributions, except that we are looking at the spatial structure of the nucleon in elastic scattering (after a Fourier transform) instead of the momentum distributions of the constituents observed in inelastic scattering. In fact, Generalized Parton Distributions (GPD) contain both form factors and quark distributions in the same framework. We will begin our description of electromagnetic form factors unconventionally starting with GPDs.

The leading twist GPD is given by the off-forward (incoming nucleon has a different momentum  $k$  than the outgoing one  $k'$ ) matrix element analogous to Eq. (1.8)

$$F(x, \xi, Q^2) = k^+ \int \frac{dz^-}{2\pi} e^{ixk^+ z^-} \langle k' | \bar{\psi}(0) \gamma^+ \psi(z^-) | k \rangle \quad (5.1)$$

which can be written in terms of two functions  $H$  and  $E$

$$F(x, \xi, Q^2) = \bar{u}(k') \left[ \gamma^+ H(x, \xi, Q^2) + \frac{i\sigma^{+\mu} q_\mu}{2M_N} E(x, \xi, Q^2) \right] u(k) \quad (5.2)$$

The functions  $u(k)$  and  $\bar{u}(k')$  are the incoming and outgoing nucleon spinors. The other variables are defined by

$$q \equiv k - k' \quad (5.3)$$

$$Q^2 \equiv -\mathbf{q}^2 \quad (5.4)$$

$$\xi \equiv \frac{q^+}{(k + k')^+} \quad (5.5)$$

The parton distributions of Chapter 4 are given by the forward limit  $k = k'$ , so that

$$q(x) = H(x, 0, 0) \quad (5.6)$$

$$\Delta q(x) = E(x, 0, 0) \quad (5.7)$$

The electromagnetic form factors are integrals over  $x$  of functions  $H$  and  $E$

$$\int_{-1}^1 dx H(x, \xi, Q^2) = F_1(Q^2) \quad (5.8)$$

$$\int_{-1}^1 dx E(x, \xi, Q^2) = F_2(Q^2) \quad (5.9)$$

where the  $F_{1,2}$  are the usual Dirac and Pauli form factors<sup>1</sup>. The dependence on  $\xi$  drops out as a special case of polynomiality: the moments of  $H$  and  $E$  must be polynomials in  $\xi$ . This property is rooted in Lorentz invariance, and is preserved by the  $\chi$ QS model [94]. The Dirac/Pauli form factors can be rewritten as the Sachs form factors

$$G_E(Q^2) = F_1(Q^2) - \frac{Q^2}{4M_N} F_2(Q^2) \quad (5.10)$$

$$G_M(Q^2) = F_1(Q^2) + F_2(Q^2) \quad (5.11)$$

---

<sup>1</sup>There are not to be confused with the structure functions  $F_{1,2}^{(N)}(x)$  discussed Chapters 1 and 4.

These electromagnetic form factors can be evaluated in terms of the quark wave functions, and are derived in Ref. [27]. The formulae are reproduced here, with a Pauli-Villars regulator, for convenience. To leading order in  $N_C$ , we have only the isoscalar electric and isovector magnetic form factors ( $G_X^{T=0,1} = G_X^p \pm G_X^n$ )

$$G_E^{T=0}(q^2) = \frac{N_C}{3} \int d\mathbf{r} e^{i\mathbf{q}\cdot\mathbf{r}} \left\{ \sum_{E_n \leq E^v} \psi_n^\dagger(\mathbf{r}) \psi_n(\mathbf{r}) - \sum_{E_n^{(0)} \leq 0} \psi_n^{(0)\dagger}(\mathbf{r}) \psi_n^{(0)}(\mathbf{r}) \right\} \quad (5.12a)$$

$$\begin{aligned} G_M^{T=1}(q^2) &= \frac{N_C M_N}{3} \varepsilon^{jkl} \frac{i q^j}{|q^2|} \int d\mathbf{r} e^{i\mathbf{q}\cdot\mathbf{r}} \left\{ \sum_{E_n \leq E^v} \psi_n^\dagger(\mathbf{r}) \gamma^0 \gamma^k \tau^l \psi_n(\mathbf{r}) \right\} \\ &\quad - PV. \end{aligned} \quad (5.12b)$$

In the nuclear medium, Eqs. (5.12) acquire a dependence on the Fermi momentum through the wave functions as described in Chapter 3. We use Eqs. (5.12a) and (5.12b) to calculate the form factors, which we present in Figs. 5.1 and 5.2. We also present the results in terms of the ratios

$$\frac{G_{E,M}^{T=0,1}(Q^2, k_F)}{G_{E,M}^{T=0,1}(Q^2, 0)} \equiv \frac{G_X^*(Q^2)}{G_X(Q^2)}, \quad (5.13)$$

where  $X$  is  $E(T = 0)$  or  $M(T = 1)$ , and the double ratio

$$\frac{G_E^*(Q^2)/G_M^*(Q^2)}{G_E(Q^2)/G_M(Q^2)}. \quad (5.14)$$

These ratios are plotted in Figs. 5.3 and 5.4 for  $0.5\rho_0$ ,  $1.0\rho_0$  and  $1.5\rho_0$ .

The electric form factor is dominated by the valence contribution and shows a dramatic effect, while the magnetic form factor has equally important contributions from the valence and the sea. The latter shows almost no change in nuclear matter; it shows only a 1.3% enhancement of the magnetic moment at nuclear density, and a 2.3% enhancement at 1.5 times nuclear density. These are consistent with the constraints of a  $< 2\%$  increase set by Ref. [45]. In contrast, the QMC model [73] predicts an enhancement of roughly 5% for Oxygen and 10% for Lead. The influence of the nuclear medium on the nucleon also causes the root mean square radius of the baryon density to increase by 3.1% in the  $\chi$ QS model. This swelling is consistent with a  $< 6\%$  increase as constrained by quasi-elastic inclusive electron-nucleus scattering data [75]. The effect in the electric form factor calculated here is comparable to that of the QMC model; the main difference from that calculation lies in

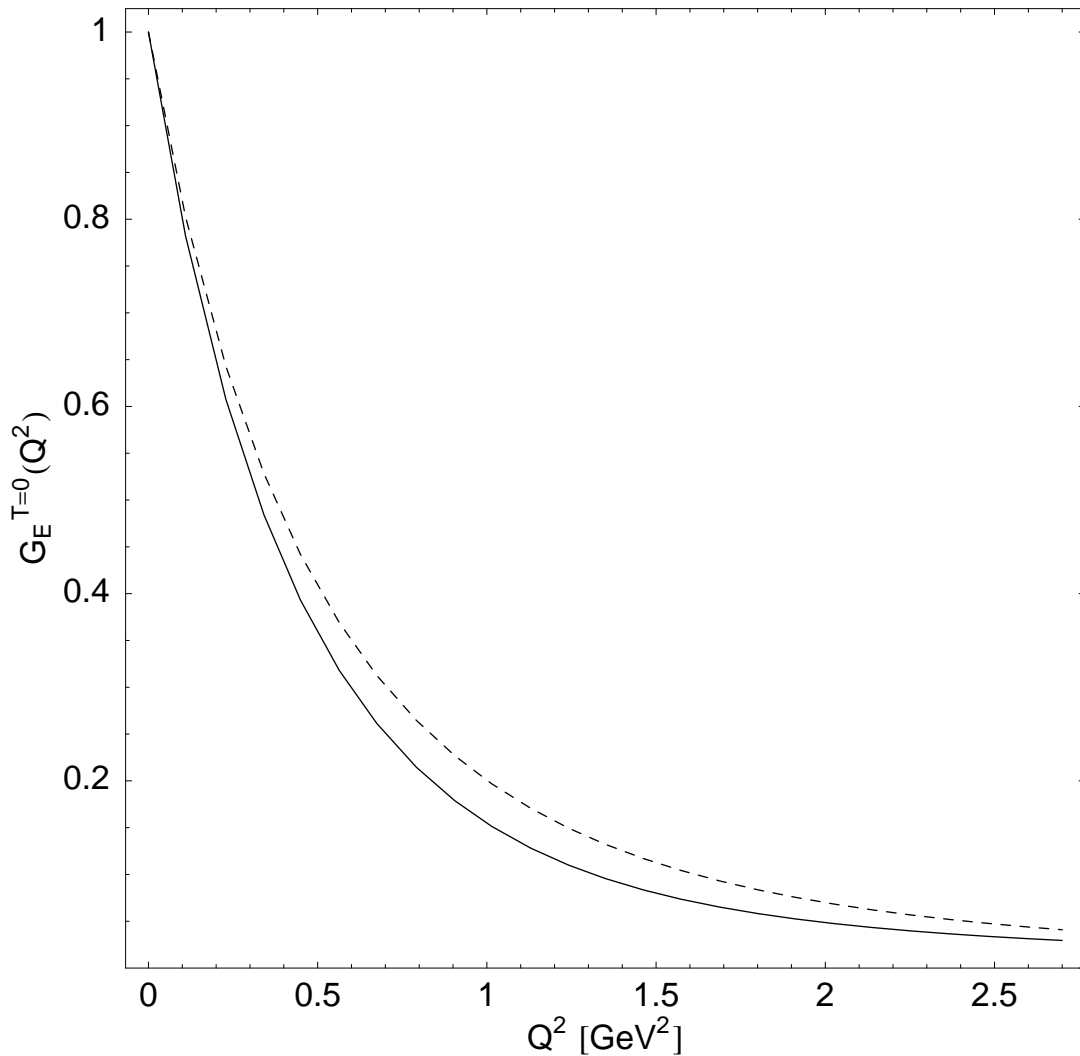


Figure 5.1: The isoscalar electric form factor at nuclear density (solid) and at zero density (dashes).

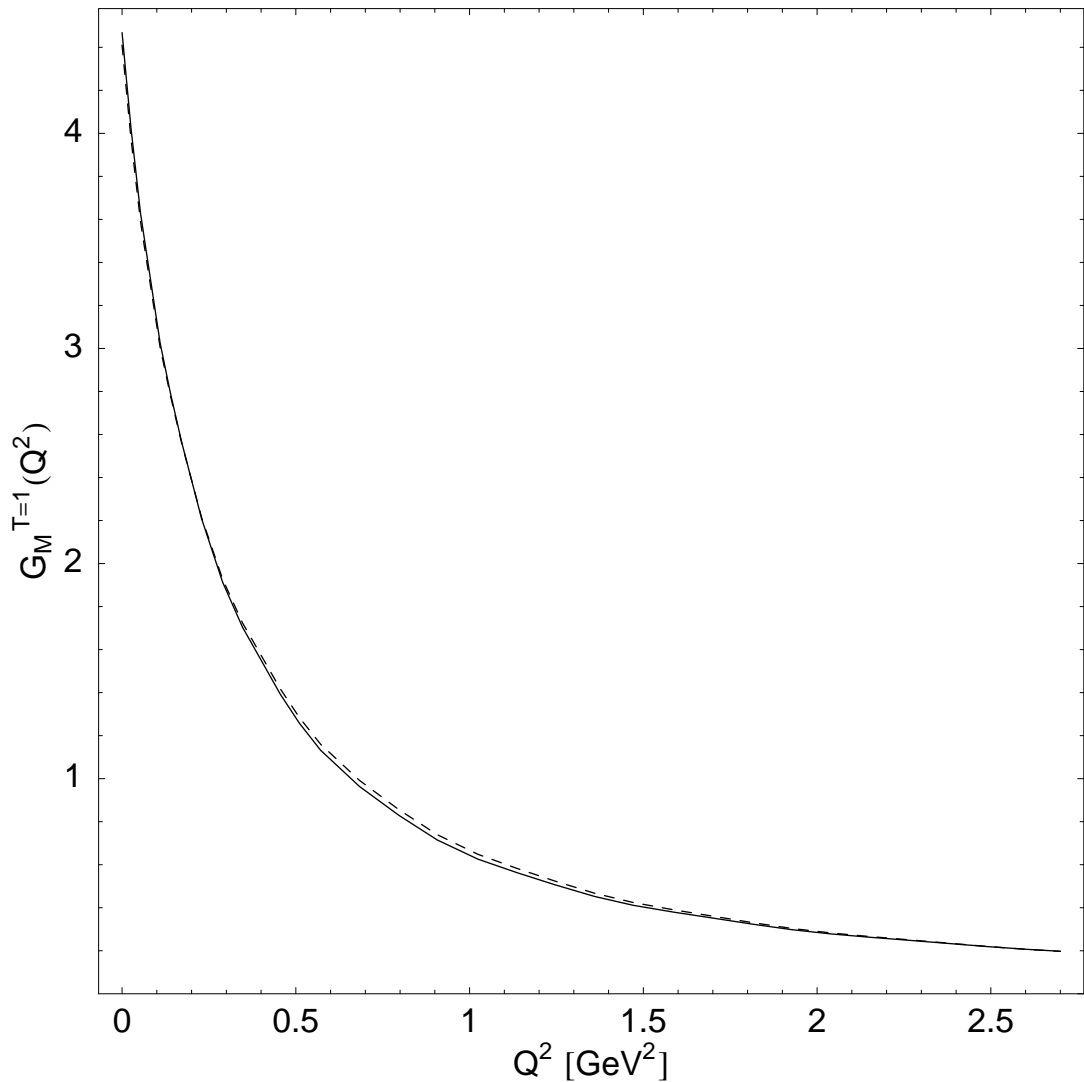


Figure 5.2: The isovector magnetic form factor at nuclear density (solid) and at zero density (dashes).

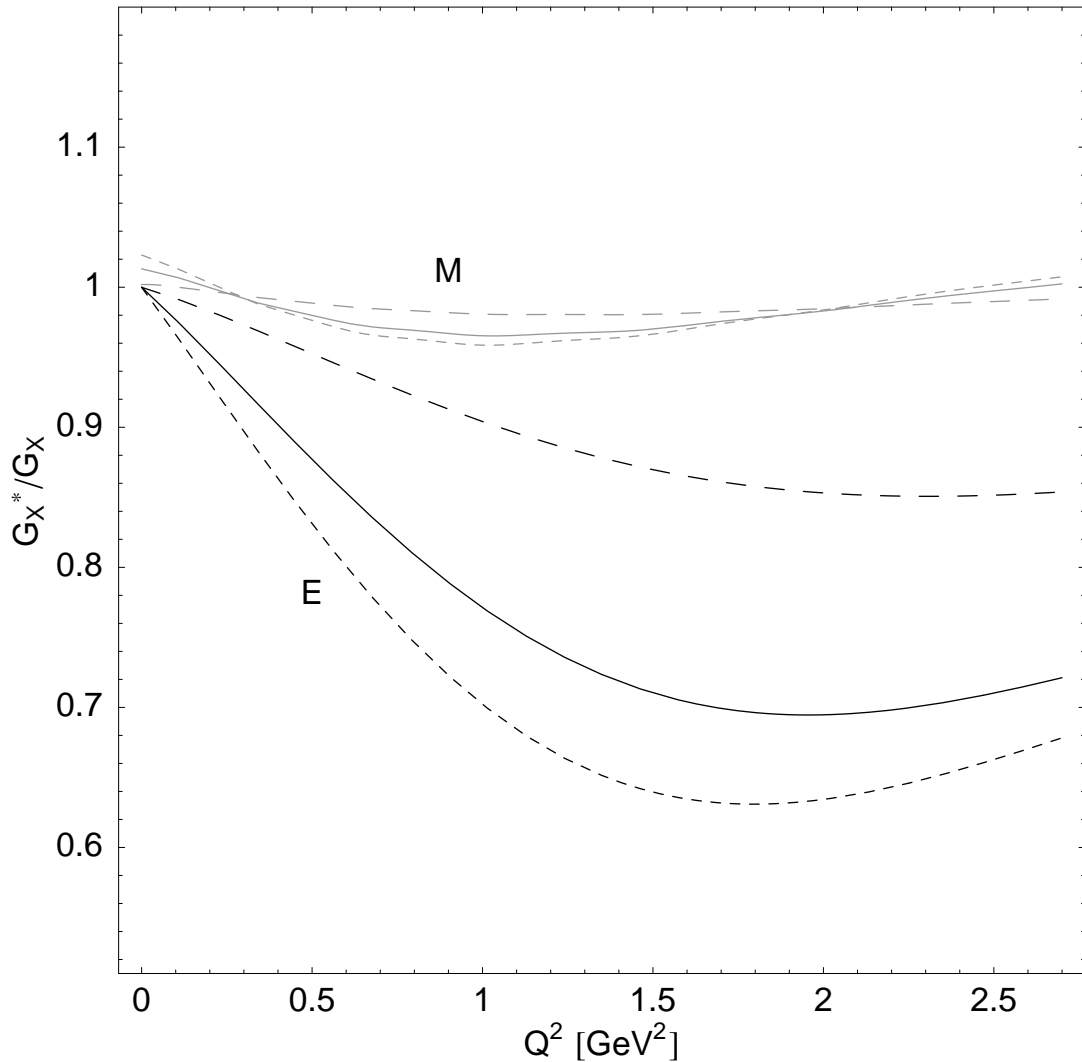


Figure 5.3: The electric (lower three curves) and magnetic (upper three curves) form factor ratios in Eq. (5.13) for  $0.5\rho_0$  (long dashes),  $1.0\rho_0$  (solid) and  $1.5\rho_0$  (short dashes).

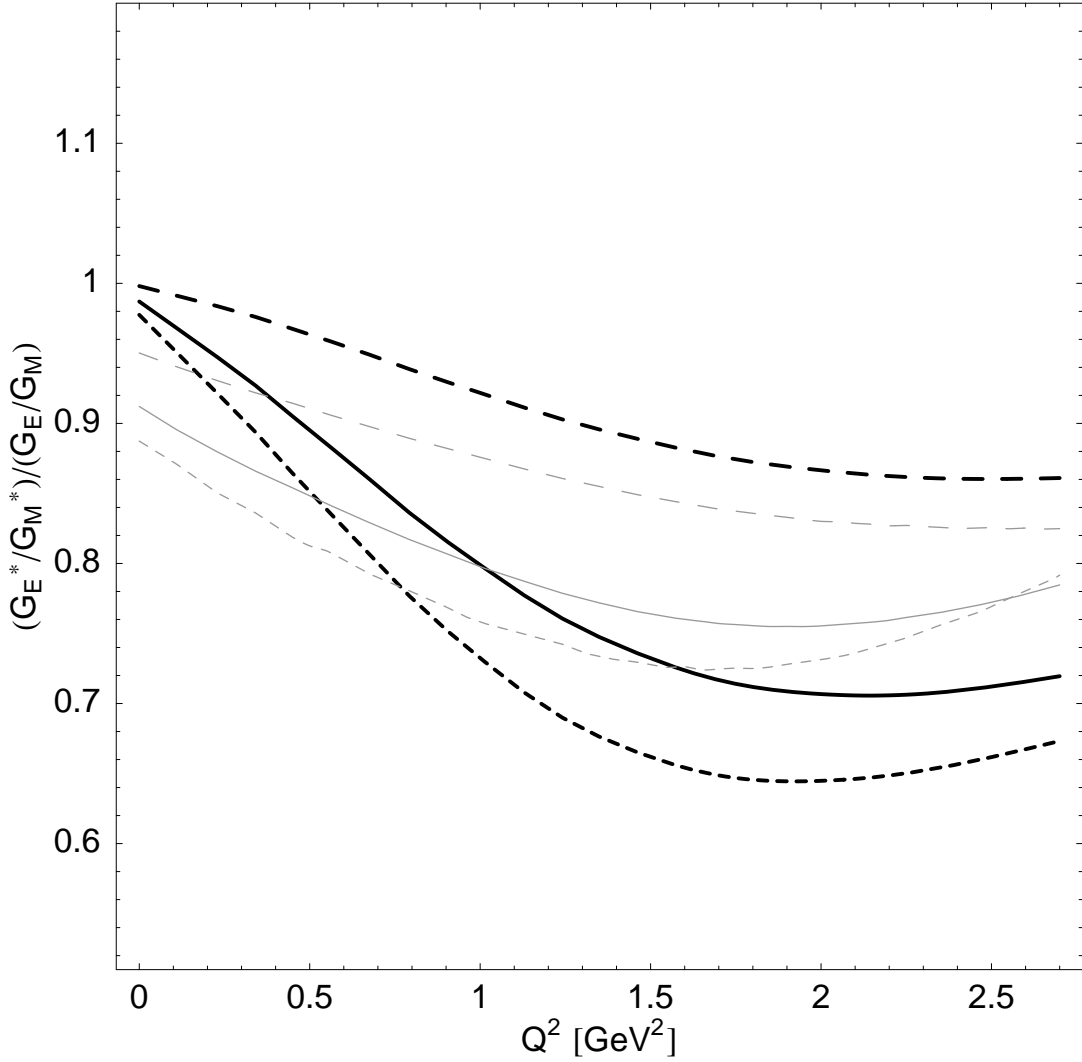


Figure 5.4: The double ratio Eq. (5.14) of the electric to magnetic form factors in nuclear matter and in the vacuum from the  $\chi$ QS model (heavy) and the QMC model [73] (light). Three densities are shown:  $0.5\rho_0$  (long dashes),  $1.0\rho_0$  (solid) and  $1.5\rho_0$  (short dashes).

the lack of enhancement in the magnetic form factor, specifically the practically unchanged value of the magnetic moment.

While both form factors use the same wave functions, the isovector magnetic form factor includes an extra weighting by a factor of the angular momentum of the state (relative to the electric form factor) due to the  $\gamma^k$  in Eq. (5.12b). This extra factor is not only responsible for making the regularization of Eq. (5.12b) necessary, but for making the sea contribution as important as the valence. In the  $\chi$ QS model, the orbital angular momentum carried by the sea is comparable to the orbital angular momentum carried by the valence quarks [107] (the sum of which make up about 60% of the total angular momentum of the nucleon state, with the remainder belonging to the intrinsic spin of the constituent quarks).

Conversely, the isoscalar electric form factor (which is finite, after the vacuum subtraction) does not have as large of a contribution from the sea. The valence level is the most important piece, even at  $Q^2 > 0$ , since the  $Q^2$  dependence in the form factors arises from the wave functions [27]. The negative Dirac continuum wave functions largely cancel in the vacuum subtraction in Eq. (5.12a).

The magnetic form factors are sensitive to the tail of the quark wave functions, and the mere existence of a tail is due to the lack of confinement. This is one reason for the discrepancy between the current results and the QMC model [73], but the primary source is due to the resistance to change of the sea. The former accounts for only a few percent of the difference; it is the latter that is our most important result. We see that the role of antiquarks is again prevalent as in our previous work [99].

The double ratio obtained in Fig. 5.4 has the same trend as the QMC model [73], but differs in the details. Since we obtain a similar double ratio, we expect to have similar results if we compare these results with the polarization transfer data [102]. This requires one to take the final state and relativistic effects into account through the use of the RDWIA [106] or the RMSGA [71], which accounts for a few percent of the discrepancy between the results for bound and free protons. A RMSGA calculation for the Helium reaction studied in Ref. [102] has been done with these  $\chi$ QS model results [70], and it delivers remarkably similar results to the same calculation done with the QMC model [71]. The  $\chi$ QS model predicts a smaller deviation than the QMC model from a Relativistic Plane Wave Impulse

Approximation (RPWIA) calculation, which is taken as a baseline in Ref. [102]. While it slightly worsens the agreement with the data at  $Q^2 \lesssim 1$ , the differences are of the same order of magnitude as the current experimental error, and both models under predict the observed deviation from a RPWIA calculation. At higher  $Q^2$ , the two models produce nearly identical results for Helium.

We ignore potentially important corrections that follow from integrating out the rotational and translational zero modes of the soliton that are suppressed by  $1/N_C$ . These corrections break the  $N - \Delta$  degeneracy, and improve the agreement of the vacuum form factors with experiment [27]. More relevant to the calculation presented here, the rotational corrections do not affect the  $Q^2$  dependence, but instead affect the normalization of the form factors [27]. However, there is no reason at that level to continue to ignore quantum fluctuations of the pion field (quark loops, also suppressed by  $1/N_C$ ) or center of mass corrections, and treat the soliton as a purely self-consistent, static mean field. We will save this difficult problem for the future.

We have calculated the electric and magnetic form factors at leading order in  $N_C$  at nuclear density using the  $\chi$ QS model. Our results help validate the apparent success of the QMC model in describing the polarization transfer experiment [102, 73], and provide a counterpoint consistent with constraints on the nucleon radius and magnetic moment in nuclei to be distinguished when finer resolution becomes available in the data. In fact, the difference between the  $\chi$ QS model double ratio and the QMC model [73] is roughly the size as the current experimental error. Specifically, data on the bound nucleon magnetic form factor at low  $Q^2$ , particularly the magnetic moment, could serve to determine the role of sea quarks in nuclei.

## Chapter 6

### SUMMARY

The Chiral Quark-Soliton model provides a intuitive, qualitative treatment that maintains consistency with all of the free nucleon properties calculated by others [39, 26]. It gives a reasonable description of nuclear saturation properties, reproduces the EMC effect, and satisfies the constraints on the nuclear sea obtained from Drell-Yan experiments with only two free parameters:  $g_s$  and  $g_v$ .

The central mechanism behind these calculated effects is that the nuclear medium provides an attractive scalar interaction that modifies the nucleon wave function. This is the same mechanism involved in other calculations [90, 9, 28, 14]. The major difference between this calculation and others is the inclusion of antiquarks at the model scale, and we see that they play an important role in the modifications, maintaining not only consistency with constraints such as those imposed by Drell-Yan experiments [2] and the theoretical and experimental understanding of magnetic moments [45], but also positivity and baryon and momentum sum rules. The latter is deeply connected with the inclusion of antiquarks and a regulator which does not interfere with the completeness of the set of quark states or the equivalence of summing over occupied and unoccupied states in the spectrum.

Dynamical rescaling, a moderately successful attempt at simultaneous phenomenological description of the EMC effect and related Drell-Yan experiments, automatically maintains the baryon and momentum sum rules due to the structure of the renormalization group equations. A change in the nucleon size in nuclei was believed to be the scale driving the effect. These are all properties of the  $\chi$ QS model, with the nucleon size swelling 3.1% in the nuclear medium. Although there is no special scale (one could point to the relative sizes of the nuclear scalar density and chiral condensate), we have a mechanism in the scalar interaction of the quarks in a nucleon with the medium. It may be possible that the spectrum of quark states in a bound nucleon is the exactly the same as in a free nucleon at

a smaller model scale  $M_{PV}$ , the Pauli-Villars mass, and hence one would have a ‘derivation’ of dynamical rescaling. It also may just be a coincidence that any model that maintains the momentum and baryon sum rules with some swelling of the nucleon describes the EMC effect and Drell-Yan data within the accuracy of current experiments.

The Wilson coefficients  $c$  in Eq. (1.9) in the OPE are dependent on the starting renormalization scale. Nuclear interactions are effective QCD interactions which renormalize a free nucleon into a bound one. In the handbag diagram Fig. 1.2, all three quarks, not just the spectator quarks, in the intermediate state are renormalized by QCD from the same starting scale, and hence all feel the effects of nuclear interactions. The picture presented in Chapter 4 is consistent with this viewpoint, while other approaches [28, 90] treat the struck quark as if it had the same normalization point as one in a free nucleon.

We have also calculated the electric and magnetic form factors at nuclear density. Our results help validate the apparent success of the QMC model in describing the polarization transfer experiment [102, 73], and provide a counterpoint to be distinguished when finer resolution becomes available in the data. In fact, the difference between the  $\chi$ QS model double ratio and the QMC model [73] is roughly the size as the current experimental error.

These successful descriptions of the medium modification of quark distributions and form factors give weight to the model and point to future experiments. For example, data on the bound nucleon magnetic form factor at low  $Q^2$ , particularly the magnetic moment, where the difference between the QMC and  $\chi$ QS models is the largest, may be able to differentiate between the two models. We also expect the results for the polarized quark distribution to manifest themselves in future experiments with polarized nuclei. These experiments could serve to help determine the role of both quarks and antiquarks in nuclei.

## BIBLIOGRAPHY

- [1] A. Airapetian et al. Measurement of the proton spin structure function  $g_1^{(p)}$  with a pure hydrogen target. *Phys. Lett. B*, 442:484, 1998.
- [2] D.M. Alde et al. Nuclear dependence of dimuon production at 800 GeV. FNAL-772 experiment. *Phys. Rev. Lett.*, 64:2479, 1990.
- [3] R. Alkofer, H. Reinhardt, and H. Weigel. Baryons as chiral solitons in the Nambu-Jona-Lasinio model. *Phys. Rept.*, 265:139, 1996.
- [4] G. Altarelli and G. Parisi. Asymptotic freedom in parton language. *Nucl. Phys. B*, 126:298, 1977.
- [5] P.L. Anthony et al. Measurements of the  $Q^2$  dependence of the proton and neutron spin structure functions  $g_1^{(p)}$  and  $g_1^{(n)}$ . *Phys. Lett. B*, 493:19, 2000.
- [6] M. Arneodo. Nuclear effects in structure functions. *Phys. Rept.*, 240:301, 1994.
- [7] J.J. Aubert et al. The ratio of the nucleon structure functions  $F_2^{(N)}$  for Iron and Deuterium. *Phys. Lett. B*, 123:275, 1983.
- [8] V.V. Barmin et al. Observation of a baryon resonance with positive strangeness in  $K^+$  collisions with Xe nuclei. *Phys. Atom. Nucl.*, 66:1715, 2003.
- [9] C.J. Benesh, T. Goldman, and G.J. Stephenson. Valence quark distribution in  $A = 3$  nuclei. *Phys. Rev. C*, 68:045208, 2003.
- [10] O. Benhar, V.R. Pandharipande, and I. Sick. Density dependence of the EMC effect. *Phys. Lett. B*, 469:19, 1999.
- [11] E.L. Berger. Nuclear effects in massive lepton pair production. *Nucl. Phys. B*, 267:231, 1986.
- [12] R.P. Bickerstaff, M.C. Birse, and G.A. Miller. Disentangling explanations of deep inelastic lepton nucleus scattering by lepton pair production. *Phys. Rev. Lett.*, 53:2532, 1984.
- [13] M. C. Birse. Relativistic mean fields and the EMC effect. *Phys. Lett.*, B299:186–188, 1993.

- [14] M.C. Birse. The axial charge of a nucleon in matter. *Phys. Lett. B*, 316:472, 1993.
- [15] M.C. Birse. Relativistic mean fields and the EMC effect. *Phys. Lett. B*, 299:186, 1993.
- [16] M.C. Birse and M.K. Banerjee. A chiral soliton model of nucleon and delta. *Phys. Lett. B*, 136:284, 1984.
- [17] J. D. Bjorken. Asymptotic sum rules at infinite momentum. *Phys. Rev.*, 179:1547–1553, 1969.
- [18] J.D. Bjorken. Applications of the chiral  $U(6) \times U(6)$  algebra of current densities. *Phys. Rev.*, 148:1467, 1966.
- [19] J.D. Bjorken. Inelastic scattering of polarized leptons from polarized nucleons. *Phys. Rev. D*, 1:1376, 1970.
- [20] J.P. Blaizot. Nuclear compressibilities. *Phys. Rept.*, 64:171, 1980.
- [21] P.G. Blunden, M. Burkardt, and G.A. Miller. Light-front nuclear physics: Mean field theory for finite nuclei. *Phys. Rev. C*, 60:055211, 1999.
- [22] P.G. Blunden and G.A. Miller. Quark-meson coupling model for finite nuclei. *Phys. Rev. C*, 54:359, 1996.
- [23] S.J. Brodsky and G.P. Lepage. Exclusive processes in quantum chromodynamics. In A. Mueller, editor, *Perturbative Quantum Chromodynamics*. World Scientific, Singapore, 1989.
- [24] S.J. Brodsky, H.C. Pauli, and S.S. Pinsky. Quantum chromodynamics and other field theories on the light cone. *Phys. Rept.*, 301:299, 1998.
- [25] M. Burkardt. Light front quantization. *Adv. Nucl. Phys.*, 23:1, 1996.
- [26] C.V. Christov et al. Baryons as non-topological chiral solitons. *Prog. Part. Nucl. Phys.*, 37:91, 1996.
- [27] C.V. Christov, A.Z. Gorski, K. Goeke, and P.V. Pobylitsa. Electromagnetic form-factors of the nucleon in the chiral quark soliton model. *Nucl. Phys. A*, 592:513, 1995.
- [28] I.C. Cloet, W. Bentz, and A.W. Thomas. Spin-dependent structure functions in nuclear matter and the polarized EMC effect. *arXiv:nucl-th/0504019*, 2005.

- [29] F. E. Close, R. L. Jaffe, R. G. Roberts, and Graham G. Ross. Change of confinement scale in nuclei: Predictions for structure functions confront electroproduction data. *Phys. Rev.*, D31:1004, 1985.
- [30] F.E. Close, R.G. Roberts, and G.G. Ross. Factorization scale independence, the connection between alternative explanations of the EMC effect and QCD predictions for nuclear properties. *Nucl. Phys. B*, 296:582, 1988.
- [31] T.D. Cohen, R.J. Furnstahl, and D.K. Griegel. Quark and gluon condensates in nuclear matter. *Phys. Rev. C*, 45:1881, 1992.
- [32] J.R. Cooke and G.A. Miller. Deuteron binding energies and form factors from light front field theory. *Phys. Rev. C*, 66:034002, 2002.
- [33] J.G. de Groot et al. QCD analysis of charged current structure functions. *Phys. Lett. B*, 82:456, 1979.
- [34] D. Diakonov. Instantons at work. *Prog. Part. Nucl. Phys.*, 51:173–222, 2003.
- [35] D. Diakonov. Relativistic mean field approximation to baryons. *Eur. Phys. J. A*, 24S1:3, 2005.
- [36] D. Diakonov et al. Unpolarized and polarized quark distributions in the large- $N_C$  limit. *Phys. Rev. D*, 56:4069, 1997.
- [37] D. Diakonov and V. Y. Petrov. Instanton based vacuum from Feynman variational principle. *Nucl. Phys.*, B245:259, 1984.
- [38] D. Diakonov, V. Y. Petrov, and P. V. Pobylitsa. A chiral theory of nucleons. *Nucl. Phys.*, B306:809, 1988.
- [39] D. Diakonov and V.Y. Petrov. Nucleons as chiral solitons. In M. Shifman, editor, *At the Frontier of Particle Physics, Vol. 1*, page 359. World Scientific, Singapore, 2001.
- [40] D. Diakonov, V.Y. Petrov, P. Pobylitsa, M. V. Polyakov, and C. Weiss. Nucleon parton distributions at low normalization point in the large  $N_C$  limit. *Nucl. Phys.*, B480:341–380, 1996.
- [41] D. Diakonov, V.Y. Petrov, and M.V. Polyakov. Exotic anti-decuplet of baryons: Prediction from chiral solitons. *Z. Phys. A*, 359:305, 1997.
- [42] Y. L. Dokshitzer. Calculation of the structure functions for deep inelastic scattering and  $e^+e^-$  annihilation by perturbation theory in quantum chromodynamics. (In Russian). *Sov. Phys. JETP*, 46:641–653, 1977.

- [43] A. R. Dzierba, C. A. Meyer, and A. P. Szczepaniak. Reviewing the evidence for pentaquarks. *hep-ex/0412077*, 2004. Talk at 1st Meeting of the APS Topical Group on Hadronic Physics (GHP2004).
- [44] M. Ericson and A.W. Thomas. Evidence for an enhanced nuclear sea from the proton - nucleus Drell-Yan process. *Phys. Lett. B*, 148:191, 1984.
- [45] T. E. O. Ericson and A. Richter. Limits on the scaling of nucleon magnetic moments in nuclei. *Phys. Lett.*, B183:249, 1987.
- [46] M.R. Frank, B.K. Jennings, and G.A. Miller. The role of color neutrality in nuclear physics—Modifications of nucleonic wave functions. *Phys. Rev. C*, 54:920, 1996.
- [47] L.L. Frankfurt and M.I. Strikman. On the normalization of nucleus spectral function and the EMC effect. *Phys. Lett. B*, 183:254, 1987.
- [48] L.L. Frankfurt and M.I. Strikman. Hard nuclear processes and microscopic nuclear structure. *Phys. Rept.*, 160:235, 1988.
- [49] J. Gasser and H. Leutwyler. Chiral perturbation theory to one loop. *Ann. Phys.*, 158:142, 1984.
- [50] D.F. Geesaman, K. Saito, and A.W. Thomas. The nuclear EMC effect. *Ann. Rev. Nucl. Part. Sci.*, 45:337, 1995.
- [51] S.D. Glazek, editor. *Theory of hadrons and light-front QCD*. World Scientific, Singapore, 1994.
- [52] J. Gomez et al. Measurement of the A-dependence of deep inelastic electron scattering. *Phys. Rev. D*, 49:4348, 1994.
- [53] V. N. Gribov and L. N. Lipatov. Deep inelastic  $e$ - $p$  scattering in perturbation theory. *Sov. J. Nucl. Phys.*, 15:438–450, 1972.
- [54] D. J. Gross and F. Wilczek. Ultraviolet behavior of non-Abelian gauge theories. *Phys. Rev. Lett.*, 30:1343–1346, 1973.
- [55] F. Gross and S. Liuti. Role of nuclear binding in the EMC effect. *Phys. Rev. C*, 45:1374, 1992.
- [56] V. Guzey and M. Strikman. Nuclear effects in  $g_1^{(A)}(x, Q^2)$  at small  $x$  in deep inelastic scattering on  ${}^7\text{Li}$  and  ${}^3\text{He}$ . *Phys. Rev. C*, 61:014002, 2000.
- [57] K. Hagiwara et al. Review of particle physics. *Phys. Rev. D*, 66:010001, 2002.

- [58] A. Harindranath. An introduction to light-front dynamics for pedestrians. In J.P. Vary and F. Wölz, editors, *Light-Front Quantization and Non-Perturbative QCD*. Int. Inst. of Theoretical and Applied Physics, Ames, IA, 1997.
- [59] M. Hirai, S. Kumano, and M. Miyama. Numerical solution of  $Q^2$  evolution equations for polarized structure functions. *Comput. Phys. Commun.*, 108:38, 1998.
- [60] C.J. Horowitz. TIMORA. In K. Langanke, J.A. Maruhn, and S.E. Koonin, editors, *Computational Nuclear Physics. Vol. 1: Nuclear Structure*. Springer-Verlag, New York, 1991.
- [61] C.J. Horowitz and B.D. Serot. Selfconsistent Hartree description of finite nuclei in a relativistic quantum field theory. *Nucl. Phys. A*, 368:503, 1981.
- [62] N.M. Hugenholtz and L. van Hove. A theorem on the single particle energy in a Fermi gas with interaction. *Physica*, 24:363, 1958.
- [63] B.L. Ioffe. Calculation of baryon masses in quantum chromodynamics. *Nucl. Phys. B*, 188:317, 1981. *Erratum-ibid.* 191:591, 1981.
- [64] X. Ji. Generalized parton distributions. *Ann. Rev. Nucl. Part. Sci.*, 54:413–450, 2004.
- [65] X.-D. Ji. Quantum field theory in light front coordinates. *Comments Nucl. Part. Phys.*, 21:123, 1992.
- [66] H. Jung and G.A. Miller. Nucleonic contribution to lepton nucleus deep inelastic scattering. *Phys. Lett. B*, 200:351, 1988.
- [67] S. Kahana and G. Ripka. Baryon density of quarks coupled to a chiral field. *Nucl. Phys. A*, 419:462, 1984.
- [68] S. Kahana, G. Ripka, and V. Soni. Soliton with valence quarks in the chiral invariant sigma model. *Nucl. Phys. A*, 415:351, 1984.
- [69] T. Kubota, M. Wakamatsu, and T. Watabe. On the chiral quark soliton model with Pauli-Villars regularization. *Phys. Rev. D*, 60:014016, 1999.
- [70] P. Lava, J. Ryckebusch, and S. Strauch. Private communication.
- [71] P. Lava, J. Ryckebusch, B. Van Overmeire, and S. Strauch. Polarization transfer in  ${}^4\text{He}(\vec{e}, e'\vec{p})$  and  ${}^{16}\text{O}(\vec{e}, e'\vec{p})$  in a relativistic Glauber model. *Phys. Rev. C*, 70:014605, 2005.

- [72] D.H. Lu, A.W. Thomas, K. Tsushima, A.G. Williams, and K. Saito. In-medium electron nucleon scattering. *Phys. Lett. B*, 417:217, 1998.
- [73] D.H. Lu, K. Tsushima, A.W. Thomas, A.G. Williams, and K. Saito. Electromagnetic form factors of the bound nucleon. *Phys. Rev. C*, 60:068201, 1999.
- [74] R. W. McAllister and R. Hofstadter. Elastic scattering of 188-MeV electrons from the proton and the alpha particle. *Phys. Rev.*, 102:851–856, 1956.
- [75] R.D. McKeown. Precise determination of the nucleon radius in  ${}^3\text{He}$ . *Phys. Rev. Lett.*, 56:1452, 1986.
- [76] G.A. Miller. Light front treatment of nuclei: Formalism and simple applications. *Phys. Rev. C*, 56:2789, 1997.
- [77] G.A. Miller. Light front quantization: A technique for relativistic and realistic nuclear physics. *Prog. Part. Nucl. Phys.*, 45:83, 2000.
- [78] G.A. Miller and R. Machleidt. Infinite nuclear matter on the light front: Nucleon-nucleon correlations. *Phys. Rev. C*, 60:035202, 1999.
- [79] G.A. Miller and J.R. Smith. Return of the EMC effect. *Phys. Rev. C*, 65:015211, 2002. *Erratum-ibid.* 66:049903, 2002.
- [80] M. Miyama and S. Kumano. Numerical solution of  $Q^2$  evolution equations in a brute force method. *Comput. Phys. Commun.*, 94:185–215, 1996.
- [81] T. Nakano et al. Evidence for a narrow  $S = +1$  baryon resonance in photo-production from neutron. *Phys. Rev. Lett.*, 91:012002, 2003.
- [82] R.J. Perry. Hamiltonian light front field theory and quantum chromodynamics. In V. E. Herscovitz *et al*, editor, *Hadron Physics 94: Topics on the structure and interactions of hadronic systems*. World Scientific, Singapore, 1994.
- [83] G. Piller and W. Weise. Nuclear deep-inelastic lepton scattering and coherence phenomena. *Phys. Rept.*, 330:1, 2000.
- [84] H. D. Politzer. Reliable perturbative results for strong interactions? *Phys. Rev. Lett.*, 30:1346–1349, 1973.
- [85] M. Praszalowicz and G. Valencia. Quark models and chiral lagrangians. *Nucl. Phys. B*, 341:27–49, 1990.

- [86] E. Ruiz Arriola, P. O. Bowman, and W. Broniowski. Landau-gauge condensates from the quark propagator on the lattice. *Phys. Rev.*, D70:097505, 2004.
- [87] E. Ruiz Arriola, C.V. Christov, and K. Goeke. Medium effects on nucleon properties. *Phys. Lett. B*, 225:22, 1989.
- [88] E. Rutherford. The scattering of alpha and beta particles by matter and the structure of the atom. *Phil. Mag.*, 21:669–688, 1911.
- [89] J. Ryckebusch, D. Debruyne, P. Lava, S. Janssen, B. Van Overmeire, and T. Van Cauteren. Relativistic formulation of Glauber theory for  $A(e, e'p)$  reactions. *Nucl. Phys. A*, 728:226, 2003.
- [90] K. Saito and A.W. Thomas. A microscopic understanding of the structure functions of finite nuclei. *Nucl. Phys. A*, 574:659, 1994.
- [91] K. Saito and A.W. Thomas. A quark-meson coupling model for nuclear and neutron matter. *Phys. Lett. B*, 327:9, 1994.
- [92] K. Saito, M. Ueda, K. Tsushima, and A. W. Thomas. Structure functions of unstable lithium isotopes. *Nucl. Phys. A*, 705:119–152, 2002.
- [93] M.M. Sargsian et al. Hadrons in the nuclear medium. *J. Phys. G*, 29:R1, 2003.
- [94] P. Schweitzer, S. Boffi, and M. Radici. Polynomality of off-forward distribution functions in the chiral quark soliton model. *Phys. Rev. D*, 66:114004, 2002.
- [95] B.D. Serot and J.D. Walecka. The relativistic nuclear many body problem. *Adv. Nucl. Phys.*, 16:1, 1986.
- [96] B.D. Serot and J.D. Walecka. Recent progress in quantum hadrodynamics. *Int. J. Mod. Phys. E*, 6:515, 1997.
- [97] I. Sick and D. Day. The EMC effect of nuclear matter. *Phys. Lett. B*, 274:16, 1992.
- [98] J.R. Smith and G.A. Miller. Return of the EMC effect: Finite nuclei. *Phys. Rev. C*, 65:055206, 2002.
- [99] J.R. Smith and G.A. Miller. Chiral solitons in nuclei: Saturation, EMC effect, and Drell-Yan experiments. *Phys. Rev. Lett.*, 91:212301, 2003.
- [100] J.R. Smith and G.A. Miller. Chiral solitons in nuclei: Electromagnetic form factors. *Phys. Rev. C*, 70:065205, 2004.

- [101] D.E. Soper. Massive quantum electrodynamics in the infinite momentum frame. *Phys. Rev. D*, 4:1620, 1971.
- [102] S. Strauch et al. Polarization transfer in the  ${}^4\text{He}(\vec{e}, e' \vec{p}) {}^3\text{H}$  reaction up to  $Q^2 = 2.6 \text{ (GeV/c)}^2$ . *Phys. Rev. Lett.*, 91:052301, 2003.
- [103] G. 't Hooft. Computation of the quantum effects due to a four-dimensional pseudoparticle. *Phys. Rev.*, D14:3432–3450, 1976.
- [104] G. 't Hooft. Symmetry breaking through Bell-Jackiw anomalies. *Phys. Rev. Lett.*, 37:8–11, 1976.
- [105] A.W. Thomas, D.H. Lu, K. Tsushima, A.G. Williams, and K. Saito. Recent results from QMC relevant to TJNAF. *arXiv:nucl-th/9807027*, 1998. Invited talk at TJNAF.
- [106] J.M. Udias, J.A. Caballero, E. Moya de Guerra, J.E. Amaro, and T.W. Donnelly. Quaiselastic scattering from relativistic bound nucleons: Transverse-longitudinal response. *Phys. Rev. Lett.*, 83:5451, 1999.
- [107] M. Wakamatsu and H. Yoshiki. A chiral quark model of the nucleon. *Nucl. Phys. A*, 524:561, 1991.
- [108] J.D. Walecka. A theory of highly condensed matter. *Annals Phys.*, 83:491, 1974.
- [109] E. Witten. Baryons in the  $1/N$  expansion. *Nucl. Phys. B*, 160:57, 1979.
- [110] U.T. Yakhshiev, U.G. Meissner, and A. Wirzba. Electromagnetic form factors of bound nucleons revisited. *Eur. Phys. J. A*, 16:569, 2003.
- [111] T.-M. Yan. Quantum field theories in the infinite momentum frame 3. Quantization of coupled spin one fields. *Phys. Rev. D*, 7:1760, 1973.
- [112] W.-M. Zhang. Light front dynamics and light front QCD. *Chinese J. Phys.*, 32:717, 1994.

## Appendix A

### THE CONNECTION TO CHIRAL PERTURBATION THEORY AND NONPERTURBATIVE QCD

In this Appendix, we perform a low-momentum expansion of the  $\chi$ QS model Lagrangian (2.10) with a non-zero current quark mass, and compare it to the Lagrangian of Gasser and Leutwyler. This has been done before in Ref. [85], for example; we present a slightly different approach here for completeness. We also fit quenched lattice data for the dynamical quark mass to a sum of propagators (as appearing in Pauli-Villars regulation of divergences).

#### A.1 *The Chiral Lagrangian*

We will first derive Eq. (2.17) with current quark mass  $m_0 \neq 0$ . Then we will proceed to higher order in the derivative expansion.

##### A.1.1 *The $\mathcal{O}(p^2)$ Lagrangian*

The constituent quark model Lagrangian in Euclidean space with (anti)quark fields  $\psi^\dagger, \psi$  that we use is

$$\mathcal{L} = \psi^\dagger(i\partial + i\hat{M}U^{\gamma_5} + im_0)\psi - \psi^\dagger(i\partial + i\hat{M})\psi \quad (\text{A.1})$$

where

$$U^{\gamma_5} \equiv U\frac{1-\gamma_5}{2} + U^\dagger\frac{1+\gamma_5}{2} \quad (\text{A.2})$$

The constituent quark mass,  $\hat{M}$ , is a function of momentum, falling to zero as the momentum goes to infinity. The second term represents the vacuum subtraction. One can integrate over the constituent quark fields in the Euclidean partition function to obtain the effective action

$$\tilde{S}[U] = -N_C \left\{ \log \det(i\partial + iMU^{\gamma_5} + im_0) - \log \det(i\partial + iM) \right\} \quad (\text{A.3})$$

We wish to look at the real part of this effective action.

$$\text{Re } \tilde{S}[U] = -\frac{N_C}{2} \log \det \left[ 1 - \frac{1}{-\partial^2 + \hat{M}^2} (\hat{M} \not{\partial} U^{\gamma_5} - m_0 \hat{M} [U + U^\dagger]) \right] \quad (\text{A.4})$$

To simplify our calculation we introduce the ‘regulated’ derivative and scalar source operators

$$\tilde{\nabla}^\mu \equiv \frac{\hat{M}}{-\partial^2 + \hat{M}^2} \partial^\mu \quad (\text{A.5a})$$

$$\tilde{\chi} \equiv 2m_0 \frac{\hat{M}}{-\partial^2 + \hat{M}^2} \quad (\text{A.5b})$$

Note that  $\tilde{\nabla}^\mu U$  is leading  $\mathcal{O}(p)$  and  $\tilde{\chi}$  is leading  $\mathcal{O}(p^2)$  from the current quark mass. After rewriting our effective action in terms of this new notation, and using  $\log \det = \text{Tr} \log$  where Tr means a functional as well as Dirac and flavor trace, we obtain

$$\text{Re } \tilde{S}[U] = -\frac{N_C}{2} \text{Tr} \log \left[ 1 - \tilde{\nabla} U^{\gamma_5} - \frac{1}{2} (\tilde{\chi}^\dagger U + U^\dagger \tilde{\chi}) \right] \quad (\text{A.6})$$

Then one can expand in derivatives of the field  $\tilde{\nabla}^\mu U$  and current quark mass, and obtain the momentum expansion of chiral perturbation theory. One essentially expands

$$\log(1 - \varepsilon) = -\varepsilon - \frac{1}{2}\varepsilon^2 - \frac{1}{3}\varepsilon^3 + \dots$$

To order  $\mathcal{O}(p^2)$ , after taking the Dirac trace, we obtain the chiral Lagrangian in leading order in  $N_C$

$$\mathcal{L}^{(N_C,2)} = N_C \text{tr} \tilde{\nabla}^\mu U \tilde{\nabla}_\mu U^\dagger + N_C \text{tr} (\tilde{\chi}^\dagger U + U^\dagger \tilde{\chi}) \quad (\text{A.7})$$

Where the lowercase trace is over flavor indices, and functional traces over the operators defined in Eq. (A.5).

### A.1.2 The $\mathcal{O}(p^4)$ Lagrangian

To order  $\mathcal{O}(p^4)$  and leading order in  $N_C$ , we obtain the operators

$$\begin{aligned} \mathcal{L}^{(N_C,4)} = & \frac{N_C}{2} \text{tr} \left( \tilde{\nabla}^\mu U \tilde{\nabla}^\nu U^\dagger \tilde{\nabla}_\nu U \tilde{\nabla}_\mu U^\dagger + \tilde{\nabla}^\mu U \tilde{\nabla}_\mu U^\dagger \tilde{\nabla}^\nu U \tilde{\nabla}_\nu U^\dagger \right) \\ & - \frac{N_C}{2} \text{tr} \left( \tilde{\nabla}^\mu U \tilde{\nabla}^\nu U^\dagger \tilde{\nabla}_\mu U \tilde{\nabla}_\nu U^\dagger \right) \\ & + N_C \text{tr} \left( \tilde{\nabla}^\mu U \tilde{\nabla}_\mu U^\dagger (\tilde{\chi}^\dagger U + U^\dagger \tilde{\chi}) \right) \\ & + \frac{N_C}{2} \text{tr} \left( (\tilde{\chi}^\dagger U + U^\dagger \tilde{\chi})^2 \right) \end{aligned} \quad (\text{A.8})$$

Table A.1: Constants appearing in the integrals for  $L_i$ .

	$i =$	1	2	3	5	8
$\lambda_i$		$\frac{1}{4}$	$\frac{1}{2}$	1	1	$\frac{1}{2}$
$\alpha_i$		4	4	4	3	2

We will use the identity, for  $N_f = 3$

$$\text{tr}(ABAB) = -2\text{tr}(A^2B^2) + \frac{1}{2}\text{tr}(A^2)\text{tr}(B^2) + \text{tr}(AB)^2 \quad (\text{A.9})$$

to put this Lagrangian in the form of Gasser and Leutwyler [49]

$$\begin{aligned} \mathcal{L}^{(N_C,4)} &= \frac{N_C}{4}(\text{tr}\tilde{\nabla}^\mu U\tilde{\nabla}_\mu U^\dagger)^2 + \frac{N_C}{2}\text{tr}(\tilde{\nabla}^\mu U\tilde{\nabla}^\nu U^\dagger)\text{tr}(\tilde{\nabla}_\mu U\tilde{\nabla}_\nu U^\dagger) \\ &\quad - N_C\text{tr}(\tilde{\nabla}^\mu U\tilde{\nabla}_\mu U^\dagger\tilde{\nabla}^\nu U\tilde{\nabla}_\nu U^\dagger) \\ &\quad + N_C\text{tr}\left(\tilde{\nabla}^\mu U\tilde{\nabla}_\mu U^\dagger(\tilde{\chi}^\dagger U + U^\dagger\tilde{\chi})\right) \\ &\quad + \frac{N_C}{2}\text{tr}(\tilde{\chi}^\dagger U\tilde{\chi}^\dagger U + U^\dagger\tilde{\chi} U^\dagger\tilde{\chi}) \end{aligned} \quad (\text{A.10})$$

This means that to leading order in  $N_C$ , the constituent quark Lagrangian Eq. (A.1) gives the Gasser and Leutwyler coefficients  $L_1, L_2, L_3, L_5$ , and  $L_8 \neq 0$  and  $L_4 = L_6 = L_7 = 0$ . When one takes the functional trace over the operator, one gets

$$L_i = \lambda_i N_C \int \frac{d^4 k}{(2\pi)^2} \left( \frac{\hat{M}(k)}{k^2 + \hat{M}(k)^2} \right)^{\alpha_i} \quad (\text{A.11})$$

where  $\lambda_i$  and  $\alpha_i$  are given in Table A.1.

## A.2 The Quark Propagator

The (quenched) lattice data [86] gives the quark propagator in terms of functions  $Z(k)$ , the wave function renormalization, and  $M(k)$ , the constituent quark mass. We fit this data with a sum of propagators as the parameterization (much like what appears in Pauli-Villars regularization)

$$\frac{Z(k)}{ik + iM(k)} \rightarrow \sum_{i=0}^n Z_i \frac{\mu_0}{\mu_i} \frac{1}{ik + i\mu_i + im_0} \quad (\text{A.12})$$

Regularizing the divergent integrals appearing in the momentum expansion (specifically the quadratically divergent chiral condensate and the logarithmically divergent pion decay constant in  $\mathcal{L}^{(2)}$ ), along with the restriction that  $Z(k \rightarrow \infty) \rightarrow 1$ , requires

$$\sum_{i=0}^n Z_i \frac{\mu_0}{\mu_i} = 1 \quad (\text{A.13a})$$

$$\sum_{i=0}^n Z_i = 0 \quad (\text{A.13b})$$

$$\sum_{i=0}^n Z_i \mu_i = 0 \quad (\text{A.13c})$$

We have taken  $n = 3$ , so we have 5 parameters to fit the lattice data. A fit of the momentum dependent quark mass  $M(p)$  with Eq. (A.12) for  $n = 3$  to the quenched lattice data for  $m_q \simeq 0.14$  GeV are shown in Fig. A.1. The same parameters do a good job of reproducing the lattice data for several other quark masses, so the extrapolation to the chiral limit shown in Fig. 2.3 is expected to allow a good qualitative comparison with the instanton model and the single Pauli-Villars subtraction used in the self-consistent calculations.

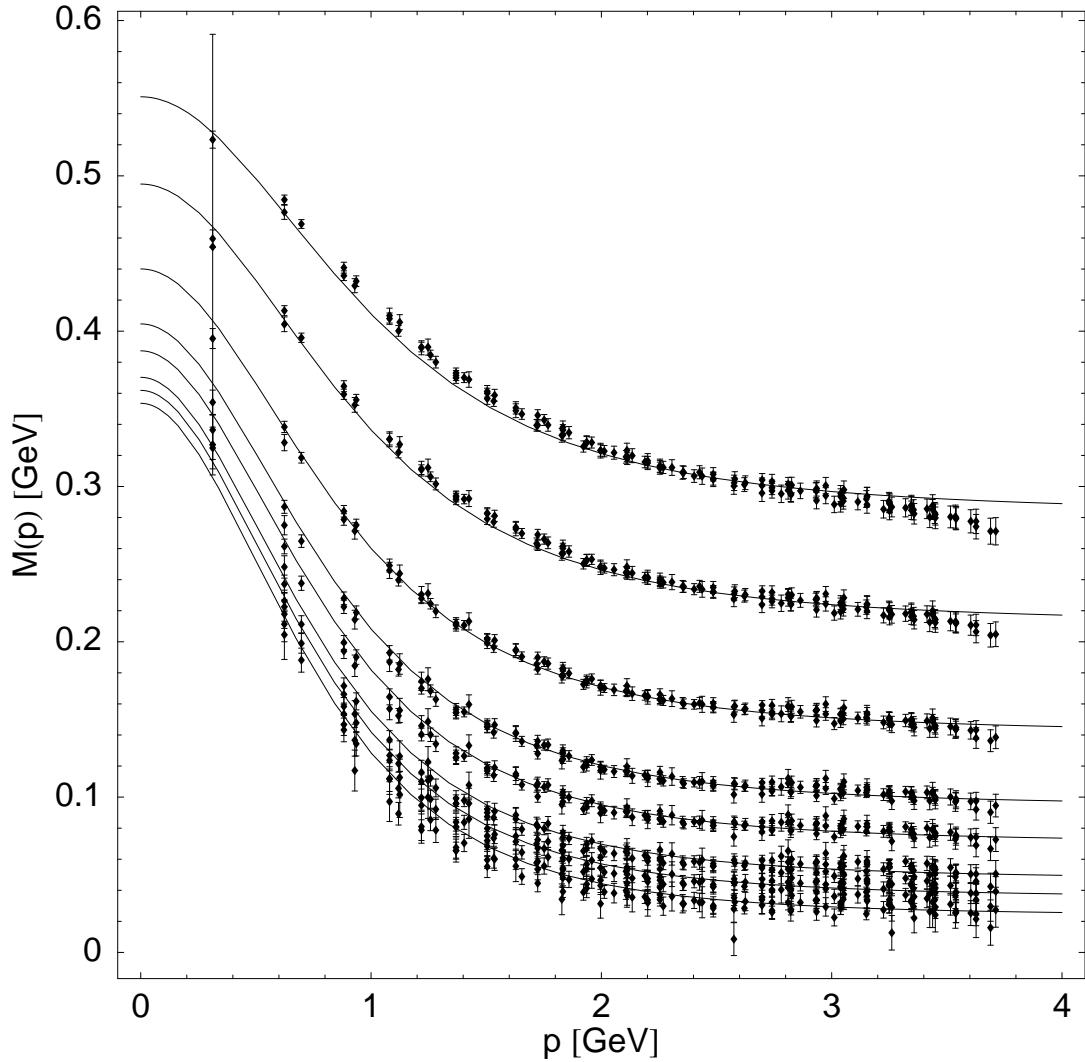


Figure A.1: Fits of Eq. (A.12) for  $n = 3$  to the quenched lattice data [86] for the dynamical quark mass  $M(p)$  at current quark masses  $m_q a = 0.012, 0.018, 0.024, 0.036, 0.048, 0.072, 0.108$ , and  $0.144$ , where  $a$  is the lattice spacing.

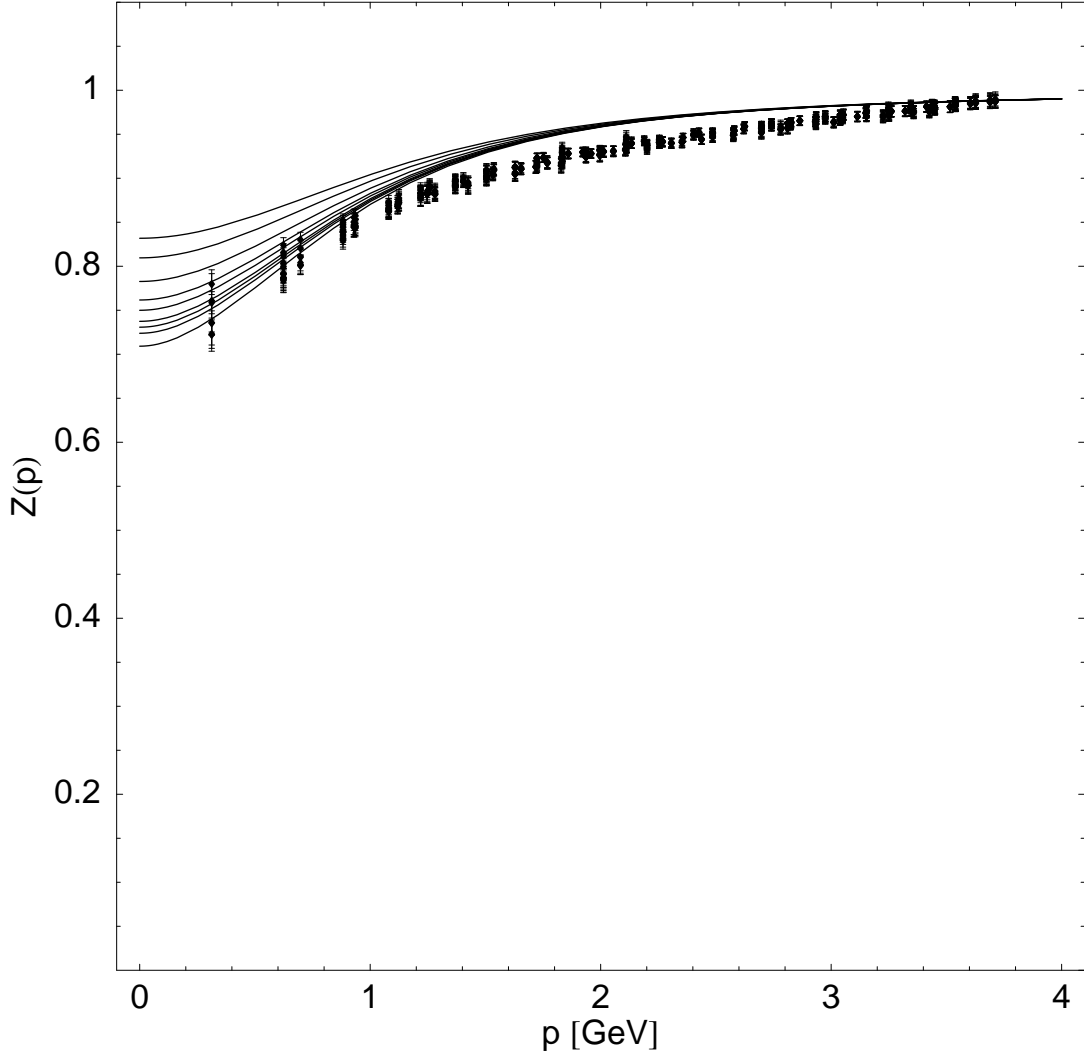


Figure A.2: Fits of Eq. (A.12) for  $n = 3$  to the quenched lattice data for the wavefunction renormalization function  $Z(p)$  at various quark masses. The data falls slightly below the fits. This can be attributed to an effect of the finite volume of the lattice [86].

## Appendix B

### THE KAHANA-RIPKA BASIS

The Kahana-Ripka basis is defined as the following set of functions inside a spherical box with radius  $L$ :

$$\phi_{nGjlMst}(\mathbf{r}) = N_{n,l} j_l(p_n r) \Xi_{Gjlst}^M(\mathbf{n}) \quad (\text{B.1})$$

where  $j_l(k_n r)$  is a spherical Bessel function. The momenta  $p_n$  are defined by

$$j_G(p_n L) = 0$$

where  $p_n < \Lambda$  and  $\Lambda$  is the basis momentum cut-off, and  $G$  is the grand spin, defined below in Eq. (B.4). The normalization  $N_{n,l}$  is defined by a property of the zeros of spherical Bessel functions. If  $a$  and  $a'$  are two zeros of  $j_l(x)$

$$j_l(a) = j_l(a') = 0$$

then

$$\int_0^1 dy y^2 j_l(ay) j_l(a'y) = \int_0^1 dy y^2 j_{l\pm 1}(ay) j_{l\pm 1}(a'y) \quad (\text{B.2})$$

$$= \delta_{a,a'} \frac{1}{2} [j_{l\pm 1}(a)]^2 \quad (\text{B.3})$$

The quantum number  $n$  is a good quantum number for the free Dirac Hamiltonian Eq. (3.13). The Dirac Hamiltonian in the  $\chi$ QS model Eq. (3.12) derived from the Lagrangian Eq. (2.10) commutes with the grand spin  $G$ , the sum of the spin, angular momentum and isospin operators

$$G = J + T = L + S + T, \quad (\text{B.4})$$

therefore we construct eigenstates  $\Xi$  of  $G$ . The functions  $\Xi$  are spinor-isospinor-spherical harmonics, defined by the sum of Clebsch-Gordan coefficients  $C_{j_1 m_1 j_2 m_2}^{jm}$ , spherical harmonics  $Y$  and (iso)spinors  $\chi$

$$\Xi_{Gjlst}^M(\mathbf{n}) = \sum_{j_3} \sum_{t_3} \sum_{l_3} \sum_{s_3} C_{jj_3 tt_s}^{GM} C_{ll_3 ss_s}^{jj_3} Y_l^{l_3}(\mathbf{n}) \chi_{s_3} \chi_{t_3}$$

The functions Eq. (B.1) are organized into eight (four in the case of  $G = 0$ ) basis functions: four with parity  $P = (-1)^l = (-1)^G$  and four with  $P = (-1)^l = (-1)^{G+1}$ . The eight can also be separated into two groups of four with  $l = G + 1, G (\times 2)$  and  $G - 1$ . There are only four functions for  $G = 0$  since  $l = G - 1$  and  $j = G - 1/2$  cannot be satisfied. The  $\Xi$  are eight element vectors, corresponding to the four of the Dirac spinor and the two of the isospinor. For an explicit example, the basis states with  $G^P = 0^+$  are

$$\phi_{n0\frac{1}{2}0}(\mathbf{r}) = \frac{1}{\sqrt{8\pi}} N_{n,0} j_0(p_n r) \begin{pmatrix} 0 \\ 0 \\ 0 \\ 0 \\ 0 \\ -1 \\ 1 \\ 0 \end{pmatrix}$$

$$\phi_{n0\frac{1}{2}1}(\mathbf{r}) = \frac{1}{\sqrt{8\pi}} N_{n,1} j_1(p_n r) \begin{pmatrix} e^{-i\phi} \sin \theta \\ -\cos \theta \\ -\cos \theta \\ -e^{-i\phi} \sin \theta \\ 0 \\ 0 \\ 0 \\ 0 \end{pmatrix}$$

with  $N_{n,l} = \sqrt{2}/j_{l+1}(p_n L)$ . They satisfy  $l = G = j - 1/2$  and  $l = G + 1 = j + 1/2$  respectively.

An explicit example of the momenta for a Kahana-Ripka basis with cutoff  $\Lambda = 600$  MeV and box size  $L = 5$  fm is in Table B.1. These represent a finite basis of 1576 functions. The largest basis used to calculate the numerical results presented here has cutoff  $\Lambda = 5000$  MeV and box size  $L = 6$  fm, for which there are  $\sim 1.7 \times 10^6$  functions. Symmetry considerations

Table B.1: The momenta for each grand spin  $G$  for the 1576 Kahana-Ripka basis functions, with cut-off and box size  $\Lambda = 600$  MeV and  $L = 5$  fm, respectively. The number of basis functions for each  $G$  for  $\Lambda = 600$  MeV (I), and  $\Lambda = 5000$  MeV (II) are shown in the far right two columns.

$G$	$p_{n=1}$	$p_2$	$p_3$	$p_4$	Total states	
	[MeV]	[MeV]	[MeV]	[MeV]	(I)	(II)
0	123.984	247.968	371.953	495.937	16	192
1	177.334	304.880	430.336	555.128	96	1128
2	227.457	358.938	486.330		120	1880
3	275.782	411.116	540.598		168	2576
4	322.928	461.939	593.546		216	3312
5	369.321	511.729			176	3960
6	414.893	560.700			208	4680
7	460.049				120	5280
8	504.793				136	5984
9	549.194				152	6536
10	593.302				168	7224
					1576	42752

immediately reduce this number to  $\sim 20,000$  depending on the specific matrix elements calculated.

## Appendix C

### DGLAP EVOLUTION

Quantum Chromodynamics tells us how to calculate parton distributions at another scale  $Q^2$  if they are given at a scale  $Q_0^2$  through the Dokshitzer-Gribov-Lipatov-Altarelli-Parisi (DGLAP) evolution equations [42, 53, 4]. In Chapter 4, we make use of QCD evolution to not only obtain the (un)polarized distributions at  $Q^2 = 10 \text{ GeV}^2$  where DIS takes place, but to smooth out the effect of the finite KR basis. First, we must write down the polarized distribution in its nonsinglet form, and the unpolarized distribution in its singlet form; these are more convenient for the application of the DGLAP equations.

The unpolarized singlet distribution is given in terms of the distributions of up and down quarks as

$$q^S(x) = \sum_i q_i(x) + \bar{q}_i(x) \quad (\text{C.1})$$

$$= u(x) + d(x) + \bar{u}(x) + \bar{d}(x). \quad (\text{C.2})$$

The polarized nonsinglet distribution is

$$\Delta q^{NS}(x) = \sum_i \frac{e_i^2 - \langle e_i^2 \rangle}{\langle e_i^2 \rangle} (\Delta q_i(x) + \Delta \bar{q}_i(x)) \quad (\text{C.3})$$

$$= \frac{3}{5} (\Delta u(x) - \Delta d(x) + \Delta \bar{u}(x) - \Delta \bar{d}(x)) + \mathcal{O}(N_C^0). \quad (\text{C.4})$$

Note that Eqs. (C.2) and (C.4) are normalized to the baryon number and axial coupling, respectively, which are both  $\mathcal{O}(N_C)$ . The combinations  $u - d$  and  $\Delta u + \Delta d$  are normalized to the isospin and spin, respectively; these are  $\mathcal{O}(N_C^0)$ . The gluon distribution is denoted  $g(x, Q^2)$ .

If we define

$$t \equiv -\frac{2}{\beta_0} \log \frac{\alpha_s(Q^2)}{\alpha_s(Q_0^2)}$$

and

$$p \otimes q(x) = \int_x^1 \frac{dy}{y} p(x/y) q(y)$$

then the DGLAP equations are given by

$$\frac{d}{dt} \Delta q^{NS}(x, t) = P_{qq} \otimes \Delta q^{NS}(x, t) \quad (\text{C.5})$$

$$\frac{d}{dt} \mathbf{q}(x, t) = \mathbf{P} \otimes \mathbf{q}(x, t) \quad (\text{C.6})$$

where

$$\mathbf{q} = \begin{pmatrix} q^S \\ g \end{pmatrix} \quad \mathbf{P} = \begin{pmatrix} P_{qq} & 2N_f P_{qg} \\ P_{gq} & P_{gg} \end{pmatrix}$$

The splitting functions  $P_{ij}$  to leading order in  $\alpha_s$  are

$$P_{qq}(x) = C_F \left[ \frac{1+x^2}{(1-x)_+} + \frac{3}{2} \delta(1-x) \right] \quad (\text{C.7})$$

$$P_{qg}(x) = T_R [x^2 + (1-x^2)] \quad (\text{C.8})$$

$$P_{gq}(x) = C_F \left[ \frac{1+(1-x)^2}{x} \right] \quad (\text{C.9})$$

$$P_{gg}(x) = 2C_G \left[ \frac{x}{(1-x)_+} + \frac{1-x}{x} + x(1-x) \left( \frac{11}{12} - \frac{1}{3} \frac{N_f T_R}{C_G} \right) \delta(1-x) \right] \quad (\text{C.10})$$

where the plus-distribution is defined by its integral with an arbitrary function  $f(x)$

$$\int_0^1 dx \frac{f(x)}{(1-x)_+} = \int_0^1 dx \frac{f(x) - f(1)}{(1-x)}$$

The DGLAP evolution equations are solved here with the brute force method following Refs. [80, 59], with  $N_t = 200$  points in the scale variable  $t$ ,  $\Delta t_j = t_{j+1} - t_j$ , and  $N_x = 1000$  points in  $x$ ,  $\Delta x_k = x_k - x_{k-1}$ . We then have, for the nonsinglet polarized distribution

$$\Delta q^{NS}(x_i, t_{j+1}) = \Delta q^{NS}(x_i, t_j) + \Delta t_j \sum_{k=i}^{N_x} \frac{\Delta x_k}{x_k} P_{qq}(x_i/x_k) q^{NS}(x_k, t_j).$$

and similarly for the singlet unpolarized distribution.

## Appendix D

### THE FAILURE OF RELATIVISTIC NUCLEAR MEAN FIELD THEORY

We have shown [79, 98] that the use of the relativistic mean field approximation, and the assumption that the structure of the nucleon is not modified by effects of the medium, to describe infinite nuclear matter leads to no appreciable binding effect. The failure was encapsulated in terms of the Hugenholtz-van Hove theorem [62] which states that the average nuclear binding energy per nucleon is equal to the binding energy of a nucleon at the top of the Fermi sea. The light front version of this theorem is obtained from the requirement that, in the nuclear rest frame, the expectation values of the total plus and minus momentum are equal. The original version of the theorem was obtained in a non-relativistic theory in which nucleons are the only degrees of freedom. Here, the mesons are important and the theory is relativistic, but the theorem still holds. This theorem can be shown to restrict [79] the plus momentum carried by nucleons to be the mass of the nucleus, which in turn implies that the probability for a nucleon to have a plus momentum  $k^+$  is narrowly peaked about  $k^+ = M_A/A = \bar{M}_N$ . Thus the only binding effect arises from the average binding energy, which is much smaller than the average separation energy. Therefore dynamics beyond the relativistic mean field approximation must be invoked to explain the EMC effect.

We briefly outline our procedure. In Sections D.1 and D.2 we present the covariant deep inelastic scattering formalism of Ref. [66] and derive its representation in terms of nucleon single particle wave functions. The plus momentum distribution follows from this representation in Section D.3 where we also derive a relativistic version of the Hugenholtz-van Hove theorem. Then we present the results of analytic and numerical calculations in Section D.4, the latter giving an  $A$  dependence of the ratio function contrary to experimental results. This demonstrates that the use of the relativistic mean field approximation, combined with the assumption that the nuclear medium does not modify the structure of the nucleon,

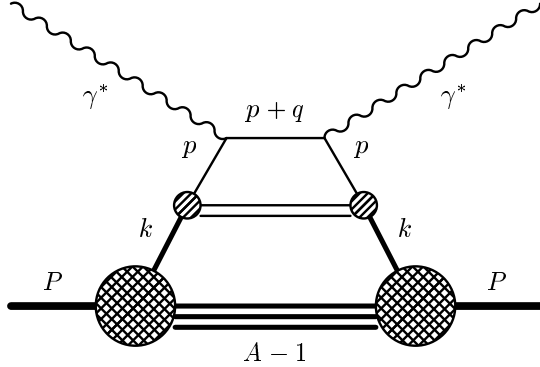


Figure D.1: Feynman diagram for deep inelastic lepton-nucleus scattering. A nucleus of momentum  $P$  is struck by a virtual photon of momentum  $q$ . We label nucleon momentum  $k$ , and quark momentum  $p$ .

cannot describe the EMC effect. The reasons for the subtle differences between the results for finite nuclei and nuclear matter are detailed in Section D.5.

### D.1 Nucleon Green's Function for Finite Nuclei

The use of a manifestly covariant formulation to derive the expression for the structure function leads to a convolution formula Eqs. (1.11) and (1.12) [66]. The function  $\chi(k, P)$  is (proportional to) the connected part of the nuclear expectation value of the nucleon Green's function, and the trace is over the Dirac and isospin indices. We begin with the covariant plus momentum distribution function. Eq. (1.12) where we identify

$$\chi^A(k, P) \equiv -i \int d^4x \int d^4y e^{-ik\cdot(x-y)} G^C(x, y), \quad (\text{D.1})$$

where  $G^C(x, y)$  is the connected part of the nucleon Green's function:

$$iG(x, y) \equiv \langle P | T^+ \{ \Psi'(x) \bar{\Psi}'(y) \} | P \rangle. \quad (\text{D.2})$$

This result is directly determined from the Feynman diagram in Fig. D.1 following Ref. [66], but with  $\chi$  having a different normalization. So far this is independent of the particular relativistic mean field model, but for concreteness we use a Quantum Hadrodynamics (QHD)

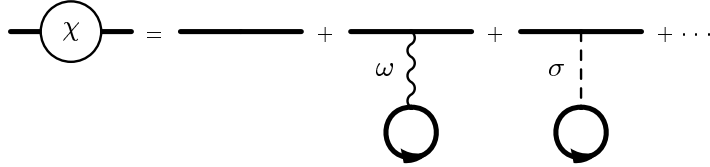


Figure D.2: The function  $\chi$  in a mean field theory with scalar ( $\sigma$ ) and vector ( $\omega$ ) mesons.

Lagrangian [96, 95], specifically QHD-I as in Ref. [21], where the nucleon fields,  $\Psi'$ , that appear in Eq. (D.2) are those appearing in the Lagrangian. Light front quantization requires that the plus component of all vector potential fields vanishes, and this is obtained by using the Soper-Yan transformation [101, 111]

$$\Psi'(x) \equiv e^{-ig_v\Lambda(x)}\Psi(x), \quad \partial^+\Lambda(x) = V^+(x). \quad (\text{D.3})$$

to define the nucleon field operator  $\Psi$  for various models [79]. This transformation allows the use of the eigenmode expansion for the  $\Psi$  fields which have been obtained previously in Ref. [21]

$$\begin{aligned} \Psi(x) &= \sum_{\alpha} \left[ a_{\alpha}\Psi_{\alpha}(x) + b_{\alpha}^\dagger\varphi_{\alpha}(x) \right] \\ &= \sum_{\alpha} \left[ a_{\alpha}\Psi_{\alpha}(\mathbf{x})e^{-ip_{\alpha}^-x^+/2} + b_{\alpha}^\dagger\varphi_{\alpha}(\mathbf{x})e^{ip_{\alpha}^-x^+/2} \right], \end{aligned} \quad (\text{D.4})$$

where  $a_{\alpha}$  and  $b_{\alpha}^\dagger$  are (anti-)nucleon annihilation operators and we define  $z \equiv -x^-/2$  with  $\partial^+ = 2\partial_- = -\partial_z$  and  $(\mathbf{x}_\perp, z) \equiv \mathbf{x}$  which allows us to treat the minus and perpendicular coördinates on equal footing. The  $\Psi_{\alpha}$  and  $\varphi_{\alpha}$  are coördinate space 4-component spinor solutions to the light front Dirac equation with eigenvalues  $p_{\alpha}^-/2 = M_N - \varepsilon_{\alpha}$ . To simplify the analysis we will temporarily ignore electromagnetic effects, but we will include them in the final numerical results. The light front mode equations in QHD-I are obtained by minimizing the  $P^-$  operator (light front Hamiltonian) with the constraint [21] that

$P^+ = P^-$ . The result is

$$-i\partial_z\Psi_\alpha^-(\mathbf{x}) = [\boldsymbol{\alpha}_\perp \cdot (\mathbf{p}_\perp - g_v \bar{\mathbf{V}}_\perp) + \beta(M_N + g_s \phi)] \Psi_\alpha^+(\mathbf{x}) \quad (\text{D.5})$$

$$\begin{aligned} p_\alpha^-\Psi_\alpha^+(\mathbf{x}) &= [-i\partial_z + 2g_v \bar{V}^-] \Psi_\alpha^+(\mathbf{x}) \\ &\quad + [\boldsymbol{\alpha}_\perp \cdot (\mathbf{p}_\perp - g_v \bar{\mathbf{V}}_\perp) + \beta(M_N + g_s \phi)] \Psi_\alpha^-(\mathbf{x}), \end{aligned} \quad (\text{D.6})$$

with

$$\Lambda_\pm\Psi_\alpha = \frac{1}{2}\gamma^0\gamma^\pm\Psi_\alpha = \Psi_\alpha^\pm \quad (\text{D.7})$$

$$\partial^+\bar{V}^\mu = \partial^+V^\mu - \partial^\mu V^+. \quad (\text{D.8})$$

Using standard manipulations [95] and defining  $\varepsilon_F$  as the energy of the highest occupied state, we find the Green's function to be

$$\begin{aligned} G(x, y) &= \sum_\alpha \Psi_\alpha(\mathbf{x}) \bar{\Psi}_\alpha(\mathbf{y}) e^{-ig_v[\Lambda(\mathbf{x})-\Lambda(\mathbf{y})]} \int \frac{dk^-}{2\pi} e^{-ik^-(x^+-y^+)/2} \left[ \frac{1}{k^- - p_\alpha^- + i\varepsilon} \right. \\ &\quad \left. + 2\pi i\delta(k^- - p_\alpha^-)\theta(\varepsilon_F - \varepsilon_\alpha) \right] \\ &\equiv G^D(x, y) + G^C(x, y), \end{aligned} \quad (\text{D.9})$$

where the superscripts  $D$  and  $C$  represent the disconnected and connected parts of the nucleon Green's function, respectively. The connected part is relevant to deep inelastic scattering and is given by

$$G^C(x, y) = i \sum_{\alpha \in F} \Psi_\alpha(\mathbf{x}) \bar{\Psi}_\alpha(\mathbf{y}) e^{-ig_v[\Lambda(\mathbf{x})-\Lambda(\mathbf{y})]} e^{-ip_\alpha^-(x^+-y^+)/2}, \quad (\text{D.10})$$

where the sum is over occupied levels  $\alpha$  in the Fermi sea  $F$ . We now substitute Eq. (D.10) into Eq. (D.1), first defining  $(\mathbf{k}_\perp, k^+) \equiv \mathbf{k}$  where  $\mathbf{k} \cdot \mathbf{x} = \mathbf{k}_\perp \cdot \mathbf{x}_\perp + k^+ z = \mathbf{k}_\perp \cdot \mathbf{x}_\perp - k^+ x^- / 2$ ,  $d\mathbf{x} = d^2\mathbf{x}_\perp dz$ ,  $d\mathbf{k} = d^2\mathbf{k}_\perp dk^+$  and

$$\Psi''_\alpha(\mathbf{k}) \equiv \int d\mathbf{x} e^{-i\mathbf{k} \cdot \mathbf{x}} e^{-ig_v \Lambda(\mathbf{x})} \Psi_\alpha(\mathbf{x}). \quad (\text{D.11})$$

We find

$$\chi^A(k, P) = (2\pi)^2 \sum_{\alpha \in F} \Psi''_\alpha(\mathbf{k}) \bar{\Psi}''_\alpha(\mathbf{k}) \delta(k^- - p_\alpha^-). \quad (\text{D.12})$$

The motivation for the ‘double-prime’ notation is the subject of the next section.

## D.2 Wave function Subtleties

It would be useful to express  $\chi^A(k, P)$  in terms of solutions of the ordinary Dirac equation, because one may use a standard computer program [60]. If we use Eq. (D.11) we find that these ‘double-primed’ fields satisfy another version of the mode equations Eq. (D.5) and Eq. (D.6) following from an application of the Soper-Yan transformation Eq. (D.3), and are given by

$$[-i\partial_z - g_v V^+] \Psi''_\alpha^- = [\boldsymbol{\alpha}_\perp \cdot (\mathbf{p}_\perp - g_v \mathbf{V}_\perp) + \beta(M_N + g_s \phi)] \Psi''_\alpha^+ \quad (\text{D.13})$$

$$[i\partial_z + g_v V^+ - 2g_v \bar{V}^- + p_\alpha^-] \Psi''_\alpha^+ = [\boldsymbol{\alpha}_\perp \cdot (\mathbf{p}_\perp - g_v \mathbf{V}_\perp) + \beta(M_N + g_s \phi)] \Psi''_\alpha^- \quad (\text{D.14})$$

If one multiplies Eq. (D.13) by  $\gamma^+$  and Eq. (D.14) by  $\gamma^-$  and adds the two equations, using  $V^+ = V^- = \bar{V}^- = V^0$ , one obtains

$$[-\gamma^3(i\partial_z + p_\alpha^-/2) + \gamma^0(p_\alpha^-/2 - g_v V^0)] \Psi''_\alpha(\mathbf{x}) = [\boldsymbol{\gamma}_\perp \cdot \mathbf{p}_\perp + M_N + g_s \phi] \Psi''_\alpha(\mathbf{x}) \quad (\text{D.15})$$

Which looks nearly like the ordinary Dirac equation which the exception of the  $\gamma^3 p_\alpha^-/2$  term. To remove this term, set

$$\tilde{\Psi}_\alpha(\mathbf{x}) \equiv e^{-ip_\alpha^- z/2} \Psi''_\alpha(\mathbf{x}) \quad (\text{D.16})$$

and substitute into Eq. (D.15), so that

$$\gamma^0(p_\alpha^-/2 - g_v V^0) \tilde{\Psi}_\alpha(\mathbf{x}) = [\boldsymbol{\gamma} \cdot \mathbf{p} + M_N + g_s \phi] \tilde{\Psi}_\alpha(\mathbf{x}) \quad (\text{D.17})$$

which looks superficially like the ordinary Dirac equation for the  $\Psi'$  fields which appear in the Lagrangian. There is a subtle difference; since the light front energy is given by  $k^2 = (\mathbf{k}_\perp^2 + M_N^2)/k^+$ , Eq. (D.15) has support for  $k^+ > 0$ . This means Eq. (D.17) has support for  $k^3 > -p_\alpha^-/2$  which in turn implies that it can only be considered the ordinary Dirac equation with a momentum cutoff at  $p_\alpha^-/2 \simeq M_N$ . This restriction is nearly superfluous since the probability that a nucleon is carrying  $|k^3| > M_N$  is suppressed by a factor of order  $e^{-M_N^2 R^2}$  with  $R$  being the nuclear radius. This allows us to effectively identify  $\tilde{\Psi}_\alpha \simeq \Psi'$  which gives the approximate relationships between the (equal time) Lagrangian fields  $\Psi'$ ,

the Soper-Yan transformed light front fields  $\Psi$  and the untransformed light front fields  $\Psi''$  that appear in Eq. (D.12). We have

$$\Psi'_\alpha(\mathbf{x}) \simeq e^{-ip_\alpha^- z/2} \Psi''_\alpha(\mathbf{x}) \quad (\text{D.18})$$

$$= e^{-ip_\alpha^- z/2} e^{-ig_v \Lambda(\mathbf{x})} \Psi_\alpha(\mathbf{x}) \quad (\text{D.19})$$

Eq. (D.19) is the approximate relationship between the  $\Psi$  and  $\Psi'$  fields in Ref. [21]. We now are ready to derive a representation of Eq. (1.12) in terms of these nucleon wave functions.

### D.3 Derivation of the Plus Momentum Distribution

#### D.3.1 General Case

In Ref. [21], it was determined that a plus momentum distribution in QHD-I is given by

$$f(k^+) = 2 \sum_{\alpha \in F} \int d^2 \mathbf{x}_\perp |\Psi_\alpha^+(\mathbf{x}_\perp, k^+)|^2. \quad (\text{D.20})$$

This distribution peaks at  $k^+/\bar{M}_N \equiv y \simeq 0.8$  for  $^{16}\text{O}$ , (with smaller values for heavier nuclei) but is not the distribution obtained from the covariant formalism of Section D.1. The connection between this  $f(y)$  and the covariant  $f(y)$  was made in Ref. [79]; it was determined that, in the limit of infinite nuclear matter, the relationship between  $f(y)$  and  $f(y)$  is simply a shift in the argument by the vector meson potential:

$$f(y) = f(y + g_v V^+ / \bar{M}_N). \quad (\text{D.21})$$

This shift arises from the use of the Soper-Yan transformation Eq. (D.3) where the  $\Psi'$  fields are those appearing in the Lagrangian and are used to determine  $f(y)$ , whereas the  $\Psi$  fields are used to determine  $f(y)$ . In finite nuclei, this relationship is somewhat more complicated since the vector meson potential is no longer a constant over all space. We start with Eq. (D.12), and see that

$$\begin{aligned} \text{Tr} \gamma^+ \chi^A(k, P) &= (2\pi)^2 \sum_{\alpha \in F} \text{Tr} \left[ \gamma^+ \Psi''_\alpha(\mathbf{k}) \overline{\Psi}'_\alpha(\mathbf{k}) \right] \delta(k^- - p_\alpha^-) \\ &= 8\pi^2 \sum_{\alpha \in F} |\Psi''_\alpha^+(\mathbf{k})|^2 \delta(k^- - p_\alpha^-). \end{aligned}$$

Substituting into Eq. (1.12) we obtain

$$f(y) = \frac{2}{(2\pi)^2} \sum_{\alpha \in F} \int d\mathbf{k} \delta(y - k^+/\bar{M}_N) |\Psi''_\alpha(\mathbf{k})|^2. \quad (\text{D.22})$$

Use of Parseval's identity and integrating over  $k^+$  gives us our main result:

$$f(y) = 2\bar{M}_N \sum_{\alpha \in F} \int d^2\mathbf{x}_\perp |\Psi''_\alpha(\mathbf{x}_\perp, \bar{M}_N y)|^2, \quad (\text{D.23})$$

so the plus momentum distribution is related to Fourier transform of the  $\Psi''$  wave functions. One can see the similarity to Eq. (D.20); the difference lies entirely in Eq. (D.11). It should be emphasized that this result does not depend on the approximation in Section D.2.

We shall use  $f(y)$  to compute the nuclear structure function  $F_2^{(A)}(x)$  in Section D.4, but first we derive a version of the Hugenholtz-van Hove theorem valid for finite nuclei. To do that, multiply Eq. (D.22) by  $y$  and integrate

$$\begin{aligned} \langle y \rangle &\equiv \int dy y f(y) \\ &= \frac{2}{(2\pi)^2} \sum_{\alpha \in F} \int d\mathbf{k} \frac{k^+}{\bar{M}_N} |\Psi''_\alpha(\mathbf{k})|^2, \end{aligned} \quad (\text{D.24})$$

Now remove the plus projections and re-express  $\Psi''$  and its complex conjugate in coördinate spaces  $\mathbf{x}$  and  $\mathbf{x}'$ . One can then integrate over  $\mathbf{k}$  yielding a delta function  $\delta(\mathbf{x} - \mathbf{x}')$  which allows integration over  $\mathbf{x}'$  yielding

$$\langle y \rangle = \frac{1}{\bar{M}_N} \sum_{\alpha \in F} \int d\mathbf{x} \Psi''_\alpha^\dagger(\mathbf{x}) \gamma^0 \gamma^+ i\partial^+ \Psi''_\alpha(\mathbf{x})$$

We wish to look at the  $\Psi$  fields in order to understand our result in the context of Ref. [21], so we need to perform the Soper-Yan transformation Eq. (D.3) and use  $X^\dagger \gamma^0 \equiv \bar{X}$

$$\langle y \rangle = \frac{1}{\bar{M}_N} \sum_{\alpha \in F} \int d\mathbf{x} \bar{\Psi}_\alpha(\mathbf{x}) \gamma^+ [i\partial^+ + g_v V^+(\mathbf{x})] \Psi_\alpha(\mathbf{x})$$

If we explicitly put in the the nuclear state vectors, we can perform the sum on  $\alpha$  by inserting creation and annihilation operators; we can add the time dependence for free since it is unaffected by  $\partial^+$  and cancels with both fermion fields, and the vector potential is static. We have effectively undone the substitution Eq. (D.4) and now have an expectation value of an operator

$$\langle y \rangle = \frac{1}{M_A} \int d\mathbf{x} \langle P | \bar{\Psi} \gamma^+ [i\partial^+ + g_v V^+] \Psi | P \rangle \quad (\text{D.25})$$

The second term of Eq. (D.25) was essentially included by Birse [15] via a kinematic argument; here it follows from a fully covariant light front treatment. Using the vector meson field equation in QHD-I

$$\partial_\mu V^{\mu+} + m_v^2 V^+ = g_v \bar{\Psi} \gamma^+ \Psi,$$

integrating by parts, and anti-symmetrizing one can re-express the second term of Eq. (D.25)

$$\begin{aligned} \langle y \rangle &= \frac{1}{M_A} \int d\mathbf{x} \langle P | \bar{\Psi} \gamma^+ i \partial^+ \Psi + m_v^2 V^+ V^+ + V^{+\mu} V_\mu^+ | P \rangle \\ &= \frac{1}{M_A} \int d\mathbf{x} \langle P | T^{++} - \partial^+ \phi \partial^+ \phi | P \rangle \\ &= \frac{1}{M_A} (P^+ - P_s^+) \\ &= 1 - \frac{P_s^+}{M_A} \simeq 1 \end{aligned} \quad (\text{D.26})$$

where  $T^{++}$  is one component of the canonical energy momentum tensor,  $P_s^+$  is the plus momentum of the scalar meson fields, and  $P^+$  is the total nuclear plus momentum. The result Eq. (D.26) constitutes an analog of the Hugenholtz-van Hove theorem [62] for finite relativistic systems; the equality becomes exact in the nuclear matter limit, where the scalar meson contribution vanishes, as shown in our previous work [79]. This means that we may anticipate that the binding effect will again be small. The vector operator ‘mixing’ and the scalar meson contribution will be elaborated on in a more general context in Section D.5.

It is also worthwhile to explicitly evaluate the expression Eq. (D.23) for  $f(y)$  in the limit of infinite nuclear matter. In this case,  $V^0 = V^+ = V^-$  are constant and  $\mathbf{V}_\perp = 0$ , so we find

$$\begin{aligned} \Lambda(z, \mathbf{x}_\perp) &= \int_z^\infty dz' V^0(z', \mathbf{x}_\perp) \\ &= -V^0 z \\ &= -V^+ z, \end{aligned} \quad (\text{D.27})$$

so that Eq. (D.11) becomes

$$\begin{aligned} \Psi_\alpha''^+(\mathbf{k}) &= \int d\mathbf{x} e^{-i\mathbf{k}_\perp \cdot \mathbf{x}_\perp} e^{-i(k^+ - g_v V^+) z} \Psi_\alpha^+(\mathbf{x}) \\ &= \Psi_\alpha^+(\mathbf{k}_\perp, k^+ - g_v V^+). \end{aligned} \quad (\text{D.28})$$

Therefore Eq. (D.23) becomes

$$f(y) = 2\bar{M}_N \sum_{\alpha \in F} \int d^2 \mathbf{x}_\perp |\Psi_\alpha^+(\mathbf{x}_\perp, \bar{M}_N y - g_v V^+)|^2, \quad (\text{D.29})$$

which is simply the expression (D.20) modified by a shift in the argument of  $g_v V^+ / \bar{M}_N$ . Thus we find Eq. (D.21) is satisfied in the nuclear matter limit. It is important to stress that all that is recovered here is the shift in the argument and not any particular form of the plus momentum distribution which arises from the specific model used for the wavefunctions.

### D.3.2 Nuclear Matter

In nuclear matter, we can derive an explicit form of  $f(y)$  valid for all mean field theories with  $k_F$  and  $M_N$  as the only input parameters. The manifestly covariant form of the single nucleon Green's function has been known for a long time [95], and its use (in the nucleus rest frame) leads to the result

$$\begin{aligned} \chi(k, P) &= -i(\gamma \cdot (k - g_v V) + M_N^*) \\ &\times \left[ \frac{1}{(k - V)^2 - M_N^{*2} + i\epsilon} + \frac{i\pi}{E^*(k)} \delta(k^0 - E^*(k) - g_v V^0) \right] \theta(k_F - |\mathbf{k}|) \end{aligned} \quad (\text{D.30})$$

where

$$E^*(k) \equiv \sqrt{M_N^{*2} + \mathbf{k}^2}. \quad (\text{D.31})$$

The general form of the Green's function depends on a vector potential  $V = (V^0, \mathbf{0})$  for a nucleus at rest, and the effective mass  $M_N^*$  which includes the effects of interactions on the nucleon mass. The values of  $V$  and  $M_N^*$  depend on the specific Lagrangian employed, but the form of the Green's function is general. Recall also that  $V^- = V^+ = V^0$  for the expectation values of vector meson fields in the nucleus rest frame.

The result Eq. (D.30) was first obtained using the conventional equal time approach, but the very same can also be obtained from the light front formalism. In that case it is necessary to include the effects of the instantaneous part of the nucleon Green's function and those of the instantaneous meson exchange.

The next step is to insert the connected part (second term) of Eq. (D.30) into Eq. (1.12) for  $f(y)$ . This gives, after taking the trace and using the delta function to integrate over  $k^0$ , the result

$$f(y) = \frac{4}{(2\pi)^3 \rho_B} \int d^2 k_\perp dk^3 \frac{E^*(k) + k^3}{E^*(k)} \delta(y - \frac{E^*(k) + g_v V^+ + k^3}{\bar{M}_N}) \theta(k_F - |\mathbf{k}|). \quad (\text{D.32})$$

The integration is simplified by using the transformation

$$k^+ \equiv E^*(k) + k^3, \quad (\text{D.33})$$

which makes a connection with light front variables. It is an exercise in geometry to show that the Fermi volume can be re-expressed in terms of  $k^+$  using

$$k_\perp^2 + (k^+ - E^*(\mathbf{k}_\perp, k^+))^2 \leq k_F^2, \quad E_F^* \equiv \sqrt{k_F^2 + M_N^{*2}}, \quad (\text{D.34})$$

$$E^*(\mathbf{k}_\perp, k^+) = \frac{1}{2} \left( k^+ + \frac{k_\perp^2 + M_N^{*2}}{k^+} \right) \quad (\text{D.35})$$

so that Eq. (D.32) becomes

$$f(y) = \frac{4}{(2\pi)^3 \rho_B} \int d^2 k_\perp \int dk^+ \theta(k_F^2 - k_\perp^2 - (k^+ - E^*(k))^2) \delta(y - \frac{k^+ + g_v V^+}{\bar{M}_N}). \quad (\text{D.36})$$

The use of the definition of the energy of a nucleon at the Fermi surface,

$$E_F = E_F^* + g_v V^+ = E_F^* + g_v V^0, \quad (\text{D.37})$$

allows one to achieve a simple expression for  $f(y)$ :

$$f(y) = \frac{3}{4} \frac{\bar{M}_N^3}{k_F^3} \theta((E_F + k_F)/\bar{M}_N - y) \theta(y - (E_F - k_F)/\bar{M}_N) \left[ \frac{k_F^2}{\bar{M}_N^2} - \left( \frac{E_F}{\bar{M}_N} - y \right)^2 \right]. \quad (\text{D.38})$$

The essence of the relativistic version of the Hugenholtz-van Hove theorem [62] follows simply from the statement that the pressure of a stable nucleus vanishes, and hence  $P^+ = P^-$ . Therefore, in the nuclear rest frame

$$\begin{aligned} E_A(k_F) &= \frac{1}{2} (P^+ + P^-) = P^+ = P^- = M_A \\ \frac{E_A(k_F)}{A} &= \frac{M_A}{A} \\ E(k_F) \equiv E_F &= \bar{M}_N \end{aligned} \quad (\text{D.39})$$

The result Eq. (D.38) can be further simplified to

$$f(y) = \frac{3}{4 \Delta_F^3} \theta(1 + \Delta_F - y) \theta(y - 1 + \Delta_F) [\Delta_F^2 - (1 - y)^2], \quad (\text{D.40})$$

where  $\Delta_F = k_F/\bar{M}_N$ , correct for any relativistic mean field theory of infinite nuclear matter. Different theories with the same binding energy and Fermi momentum may have very different scalar and vector potentials, but must have the same  $f(y)$ .

A result very similar to Eq. (D.40) was previously obtained by Birse [13]. The difference between his formula and ours is the appearance of  $\bar{M}_N$  in the function  $f(y)$ , whereas he uses  $M_N$ . This difference is a small effect numerically, and therefore our conclusions will be the same as his.

The baryon sum rule and momentum sum rules are derived by taking the first two moments of  $f(y)$ . This gives:

$$\int dy f(y) = 1 \quad (\text{D.41})$$

$$\int dy y f(y) = 1. \quad (\text{D.42})$$

The latter equation is remarkable; it states that in deep inelastic scattering the nucleons act as if they carry all of the  $P^+$  of the nucleus even though the mesonic fields may be very prominent.

This is clearer if we re-interpret these sum rules in terms of a probability  $f(k^+)$  that a nucleon has a plus momentum  $k^+ \equiv y\bar{M}_N$ , with  $f(k^+) \equiv Af(y\bar{M}_N)/\bar{M}_N$ , so that

$$\int dk^+ f(k^+) = A, \quad (\text{D.43})$$

$$\int dk^+ k^+ f(k^+) = A\bar{M}_N = M_A \quad (\text{D.44})$$

The momentum sum rule Eq. (D.44) shows the total plus momentum carried by the nucleons (as seen in deep inelastic scattering) is also the total momentum carried by the nucleus.

The main result of this is that the nuclear structure function is given by 1.12) with the function  $f(y)$  obtained in D.40). This tells us that, despite the fact that there is considerable binding energy, there is no EMC binding effect. Indeed,  $F_2^{(A)}$  depends on the Fermi momentum but does not depend on the effective mass  $M_N^*$ .

#### D.4 Nuclear Structure Functions

We determine the wave functions appearing in Eq. (D.23) numerically from a relativistic self-consistent treatment following Horowitz and Serot [61] using the same program [60] which includes electromagnetic effects. The plus momentum distribution follows and is given in Fig. D.3 for  $^{16}\text{O}$ ,  $^{40}\text{Ca}$ ,  $^{208}\text{Pb}$  and in the nuclear matter limit. One can see that the peaks appear near  $y = 1$  as required by the Hugenholtz-van Hove theorem Eq. (D.26).

It is worth noting that application of the Soper-Yan transformation Eq. (D.3) to the  $\Psi''$  wavefunctions obtained from the equal time wavefunctions reproduces the plus momentum distributions, including the correct asymmetry, of the light front calculations in Ref. [21], which did not use the approximation Eq. (D.18). We show the comparison of our Oxygen calculation to that of Ref. [21] in Fig. D.4; the agreement of these two curves demonstrates the excellence of the approximation relating light front and equal time wavefunctions. One can see that the effect in finite nuclei of the Soper-Yan transformation is to shift and broaden the plus momentum distribution, while in nuclear matter (also shown in Fig. D.4) it is just a shift. If these distributions were to be used in the nuclear structure function Eq. (4.9) though, since  $\langle y \rangle \simeq 0.8$  for Oxygen, the ratio function (Eq. (4.8) discussed later) would fall precipitously to nearly zero at  $x \simeq 0.6$  in stark contradiction with experiment.

The structure function is given by the convolution Eq. (4.9) with the generic function  $q = F_2^{(N)}$ . The assumption that nuclear effects do not modify the structure of the nucleon is embodied in Eq. (4.9) by the use of the structure function of a free nucleon; we use the parameterization [33]

$$F_2^{(N)}(x) = 0.58\sqrt{x}(1-x)^{2.8} + 0.33\sqrt{x}(1-x)^{3.8} + 0.49(1-x)^8. \quad (\text{D.45})$$

The experiments measure the ratio function Eq. 4.8. The results of our calculations are plotted for  $^{16}\text{O}$ ,  $^{40}\text{Ca}$ ,  $^{208}\text{Pb}$  and in the nuclear matter limit in Fig. D.5 showing data for Carbon, Calcium and Gold from SLAC-E139 [52] and an extrapolation [97] for the nuclear matter calculation. The most striking result is that these calculations fail to reproduce the EMC effect; the curves consistently miss the minima in the data, and the agreement gets worse with increasing  $A$ . Another important result is that the ratio function does not fall

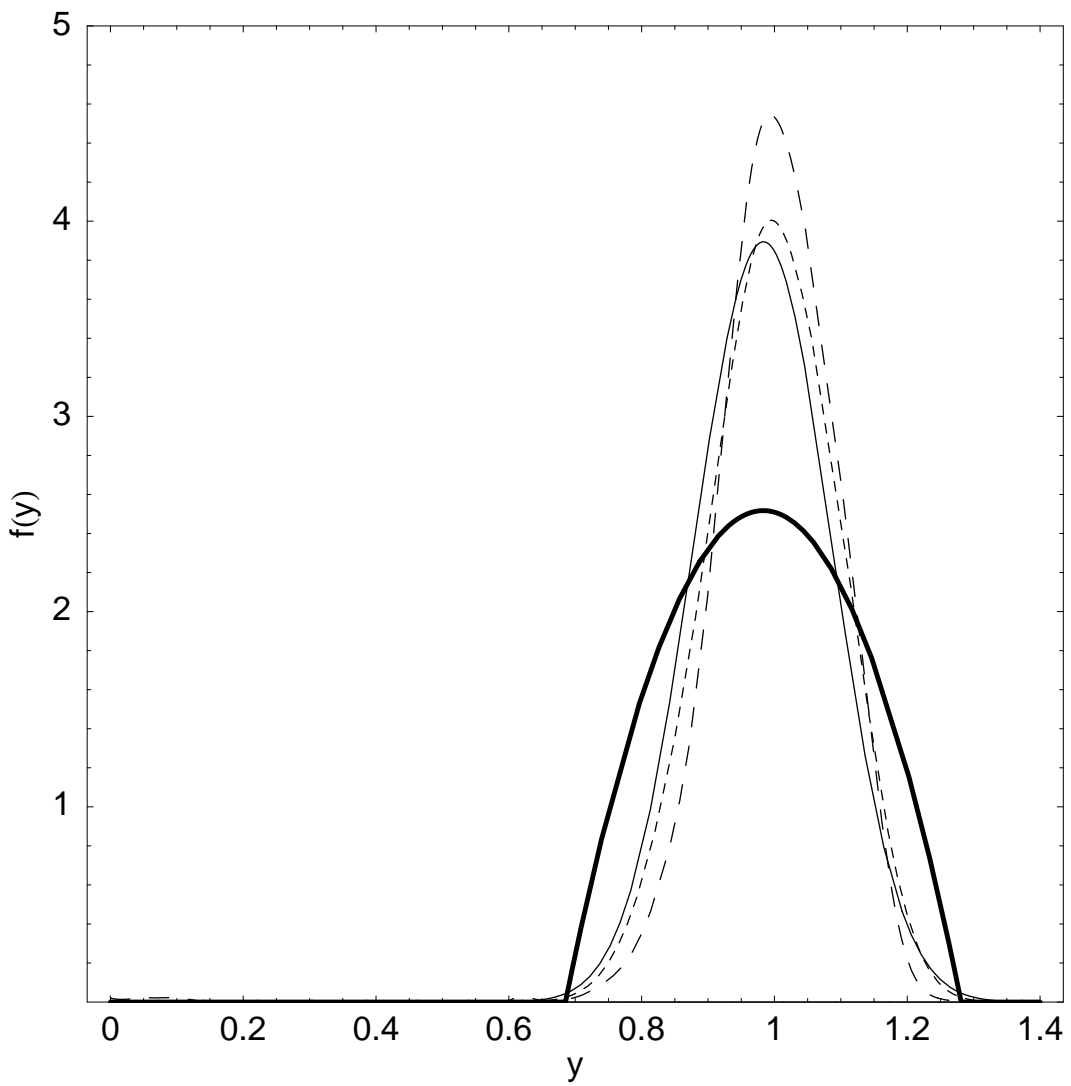


Figure D.3: Plus momentum distributions,  $f(y)$ , for  ${}^{40}\text{Ca}$  (solid),  ${}^{16}\text{O}$  (short dashes),  ${}^{208}\text{Pb}$  (dot-dashes) and nuclear matter (long dashes).

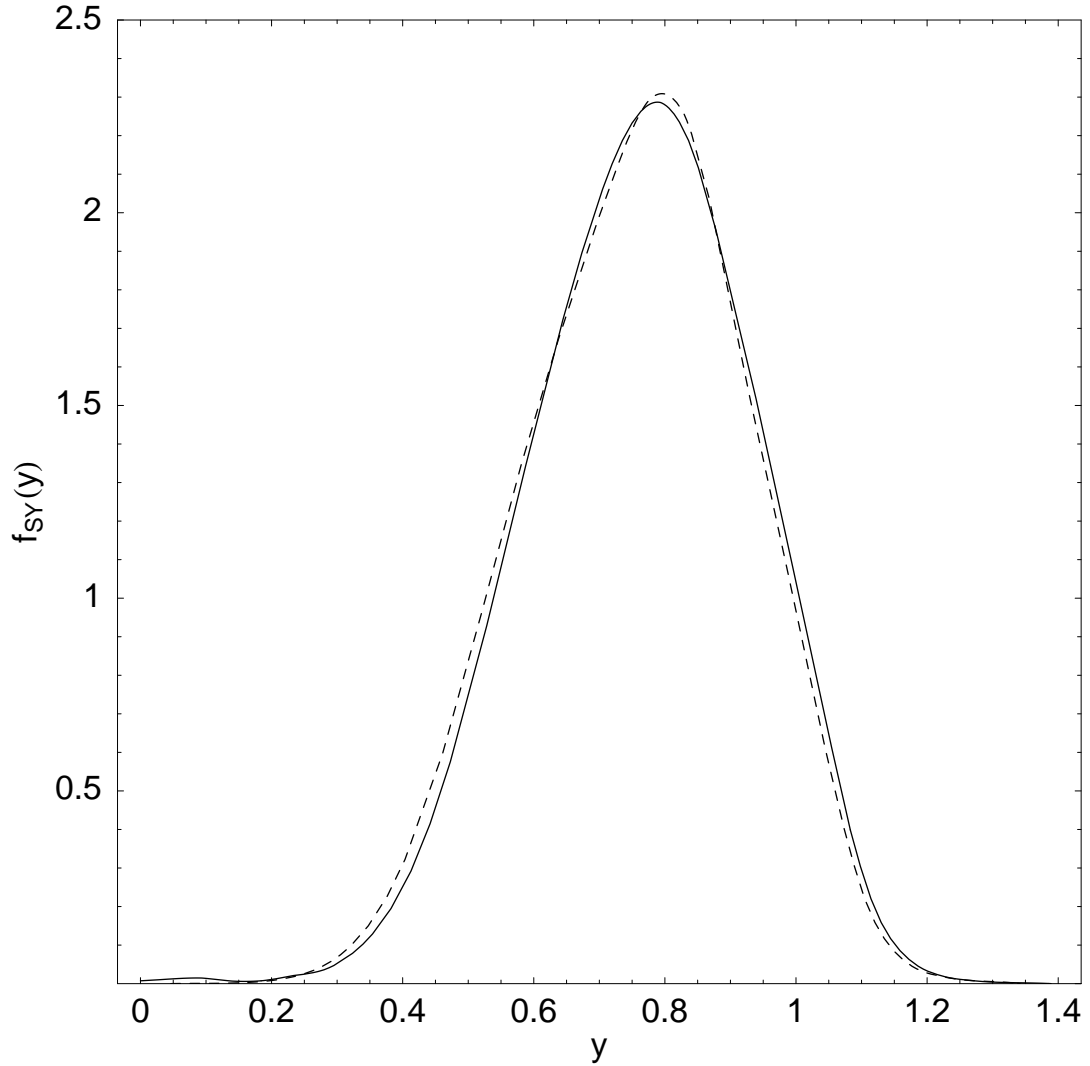


Figure D.4:  $f(y)$  distribution for  $^{16}\text{O}$  (solid) after application of the Soper-Yan transformation along with the  $^{16}\text{O}$  distribution from Ref. [21] (short dashes). Note that the peaks occur at  $y < 1$ .

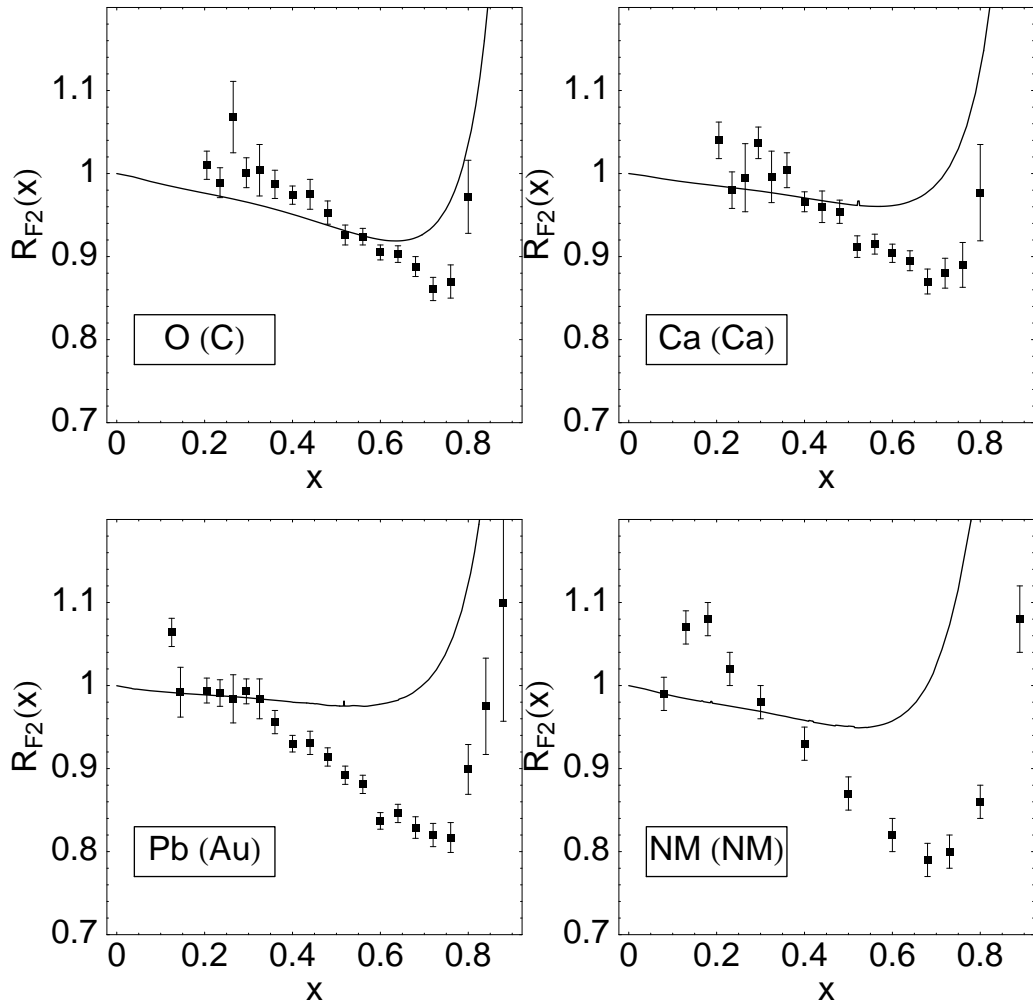


Figure D.5: Ratio functions for  $^{16}\text{O}$ ,  $^{40}\text{Ca}$  and  $^{208}\text{Pb}$  showing data for Carbon, Calcium and Gold, respectively, from SLAC-E139 [52]. The nuclear matter calculation shows extrapolated data [97].

to zero as would be the case if the small effective mass ( $\sim 0.56M_N$  for nuclear matter in QHD-I) were the relevant parameter describing the binding effect which would follow from using Eq. (D.20) instead of Eq. (D.23). The results also show a minimum near  $x \simeq 0.6$  for Oxygen and nuclear matter that is deeper than the Calcium and Lead calculations. This is a curious feature that contradicts the trend in experimental data, and is due to the effects of two parameters.

The first, and most important, is that of the location of the peak of the plus momentum distribution given by Eq. (D.26), which gradually approaches  $y = 1$  as the nuclear matter limit is reached. This is due to the fact that scalar mesons carry a small amount of plus momentum [21] that vanishes as  $A \rightarrow \infty$ . The closer to  $y = 1$  the peak is in Fig. D.3, the less pronounced the minimum in Fig. D.5, all else remaining constant. The second effect is due to  $\bar{M}_N$ , which reaches a minimum at  $^{56}\text{Fe}$  corresponding to a more pronounced minimum of the ratio function than for  $A < 56$  or  $A > 56$ , keeping the scalar meson contribution constant.

Using a Gaussian parameterization of the plus momentum distribution and the experimental binding energy per nucleon via the semi-empirical mass formula, we have modeled the dependence of the minimum of the ratio function,  $R(x \simeq 0.72)$ , on the number of nucleons in the nucleus in Fig. D.6. The motivation for the use of Gaussian plus momentum distributions is based on the expansion [48]

$$\begin{aligned} F_2^{(A)}(x_A) &= F_2^{(N)}(x_A) + \epsilon x_A \frac{\partial F_2^{(N)}}{\partial x} \Big|_{x=x_A} \\ &\quad + \gamma \left[ 2x_A \frac{\partial F_2^{(N)}}{\partial x} \Big|_{x=x_A} + x_A^2 \frac{\partial^2 F_2^{(N)}}{\partial x^2} \Big|_{x=x_A} \right] \end{aligned} \quad (\text{D.46})$$

$$\text{where } \epsilon \equiv 1 - \int dy y f(y) \quad (\text{D.47})$$

$$\gamma \equiv \int dy (y - 1)^2 f(y) \quad (\text{D.48})$$

The Gaussian parameterization uses the peak location and width,  $\langle y \rangle$  and  $(\langle y^2 \rangle - \langle y \rangle^2)^{1/2}$  respectively, from the relativistic Hartree calculations in Fig. D.3, and is normalized to unity. This allows us to obtain a plus momentum distribution for any  $A$  with minimal effort. We show the combined effect of scalar mesons and binding energy per nucleon on the ratio

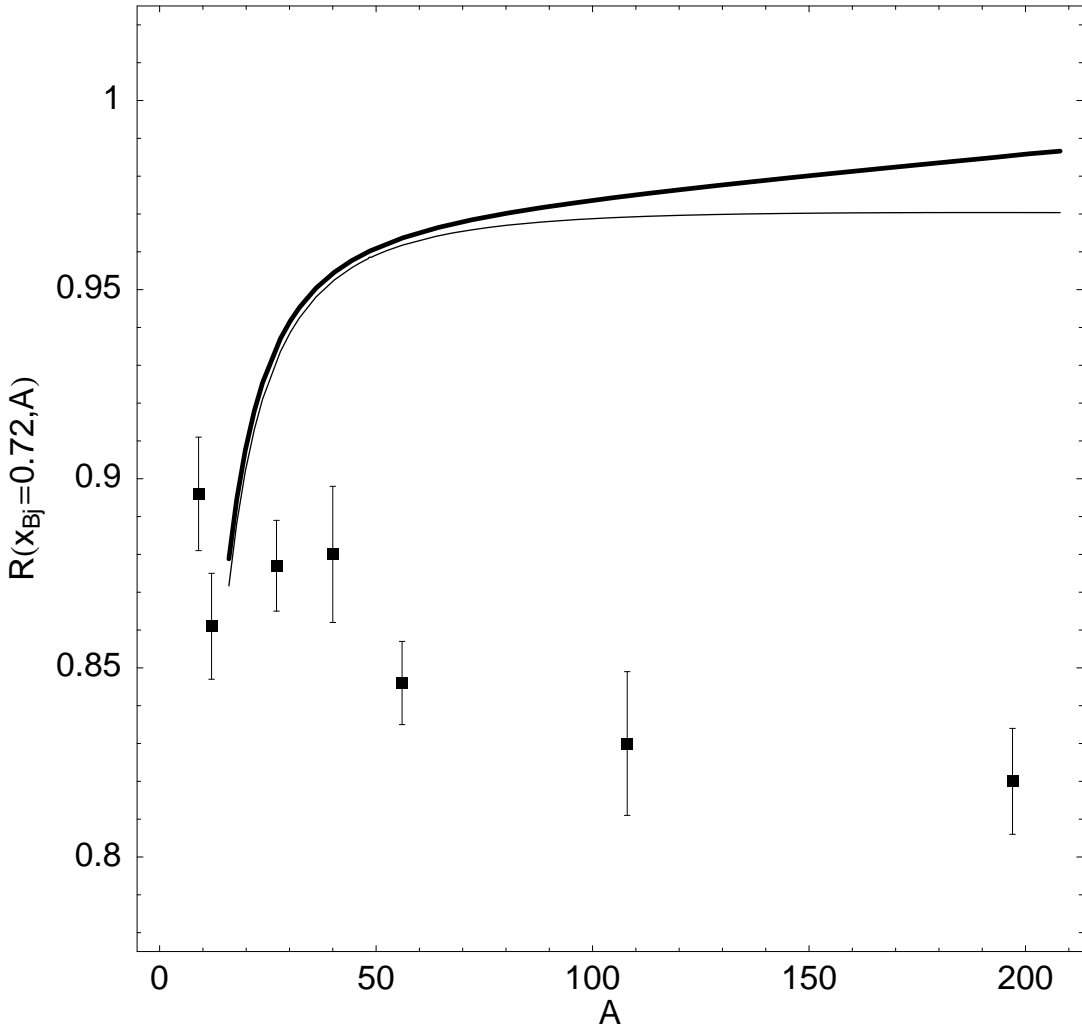


Figure D.6:  $R(x = 0.72)$  as a function of  $A$  including scalar meson and binding effects (solid line), and leaving binding energy per nucleon constant at  $-8.5$  MeV (dashed line). The data are from SLAC-E139 [52].

function along with the effect of scalar mesons alone using a constant binding energy per nucleon of  $-8.5$  MeV independent of  $A$ . It can be seen that a changing  $\bar{M}_N$  with  $A$  has the most effect for nuclei much larger than Iron, but does not change the general trend that the minimum of the ratio function becomes less pronounced as  $A$  increases due to the vanishing scalar meson contribution and the peak of the plus momentum distribution approaching unity. This dependence of the binding effect on  $A$  is quite different, both in magnitude and shape, than the trend in experimental data summarized in Ref. [97] which satisfies  $R(x \simeq 0.72) \sim A^{-1/3}$ , so that the minimum becomes more pronounced as  $A$  increases. This fully demonstrates the inadequacy of conventional nucleon-meson dynamics to explain the EMC effect.

### **D.5 Scalar Mesons and More General Considerations**

The average value of  $y$ , given by Eq. (D.26), yields the nucleon contribution to the plus momentum, and is less than one which can be seen in Fig. D.3. We now address the remaining plus momentum in finite nuclei. Previous results [21] show that a small fraction ( $\delta y \sim 0.005$ ) of the plus momentum is carried by the scalar mesons which vanishes as the nuclear matter limit is approached. This is due to the fact that scalar mesons couple to gradients in the scalar density (arising mainly from the surface of finite nuclei) which vanish as  $A \rightarrow \infty$ . The question is: why are scalar mesons allowed to carry plus momentum and not vector mesons?

The simplest answer lies in the Dirac structure of Eq. (1.12); the  $\gamma^+$  in the trace picks out terms in the full interacting Green's function with an odd number of gamma matrices which includes all Lorentz vector interactions and excludes Lorentz scalar interactions. The Dirac structure of  $f(y)$  is directly related to the Dirac structure of the energy momentum tensor, so the answer also lies there and illuminates a problem with conventional nucleon-meson dynamics. The component of the energy momentum tensor relevant to the plus momentum, from a chiral Lagrangian containing isoscalar vector mesons, scalar mesons and

pions, is given by [76, 78]

$$\begin{aligned} T^{++} = & V^{+\mu}V_\mu^+ + m_v^2 V^+V^+ + \bar{\Psi}\gamma^+i\partial^+\Psi + \partial^+\phi\partial^+\phi \\ & + \partial^+\pi\cdot\partial^+\pi + \pi\cdot\partial^+\pi \frac{\pi\cdot\partial^+\pi}{\pi^2} \left(1 - \frac{f^2}{\pi^2} \sin^2 \frac{\pi}{f}\right). \end{aligned} \quad (\text{D.49})$$

Since each of the terms in Eq. (D.49) involves one of the fields, it is natural to associate each term with a particular contribution to the plus momentum. This decomposition, though, is not well defined; field equations relate various components. We see the first three terms of Eq. (D.49) appear in  $\langle y \rangle$ , which defines the nucleon contribution to the total nuclear plus momentum, in the derivation of the Hugenholtz-van Hove theorem Eq. (D.26); we are not allowed to have the vector mesons contribute a well defined fraction of plus momentum. This means that one could trade certain mesonic degrees of freedom for nucleons by replacing mesonic vertices with nucleon point couplings, for example, in line with the general concept of effective field theory. In our case the first three terms are related by the vector meson field equation, but the fourth is left out since the scalar mesons couple to the scalar density  $\bar{\Psi}\Psi$  which is not present in Eq. (D.49). Therefore the scalar mesons (and pions) contribute a well defined fraction of plus momentum. These explicit meson contributions create an EMC binding effect, but the pionic contributions are also limited by nuclear Drell-Yan experiments [2] to carrying about 2% of the plus momentum which is insufficient to account for the entire EMC effect which corresponds to about 5% of the plus momentum for Iron.

## VITA

Jason Smith was born in Mattoon, Illinois on December 20, 1976, although he spent the vast majority of his childhood in The Woodlands, Texas, a suburb of Houston. He has been slowly educated since 1982, earning along the way a Bachelor of Science in Physics and a Bachelor of Science in Mathematics from the University of Texas at Austin in May of 1999, and a Doctor of Philosophy in physics from the University of Washington, Seattle in August of 2005.